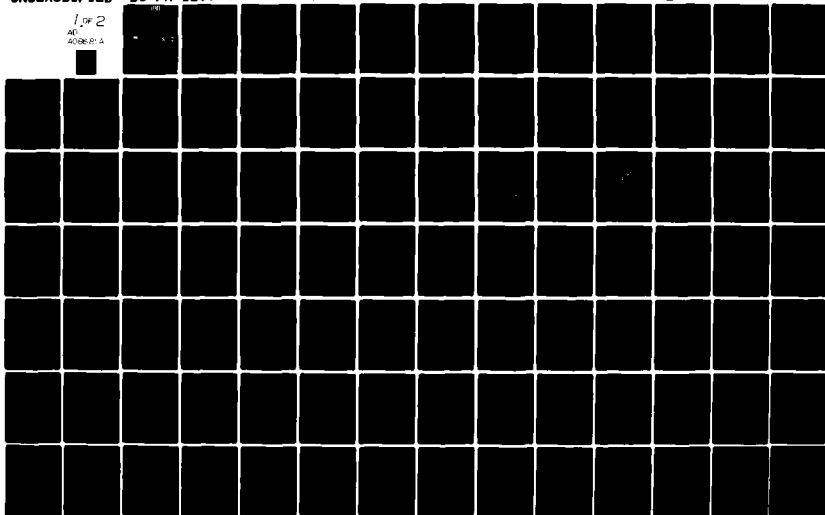


AD-A086 814

DIKEWOOD INDUSTRIES INC ALBUQUERQUE NM F/G 20/14
PARALLEL-PLATE TRANSMISSION LINE TYPE OF EMP SIMULATORS: SYSTEM--ETC(U)
MAY 80 D V GIRI, T K LIU, F M TESCHE F29601-78-C-0045
DC-FR-1299-4 AFWL-TR-79-139 NL

UNCLASSIFIED

1 OF 2
AD
AD-86-814



AFWL-TR-79-139

(2)

LEVEL III

AD-E200320

AFWL-TR-
79-139

ADA086814



PARALLEL-PLATE TRANSMISSION LINE TYPE OF EMP SIMULATORS: SYSTEMATIC REVIEW AND RECOMMENDATIONS

D. V. Giri, et al.

Dikewood Industries, Inc
1009 Bradbury Dr., SE
Albuquerque, NM 87106

May 1980

Final Report

DTIC
ELECTE
S JUL 17 1980 D
B

Approved for public release; distribution unlimited.

DDC FILE COPY

AIR FORCE WEAPONS LABORATORY
Air Force Systems Command
Kirtland Air Force Base, NM 87117

80 6

10 008

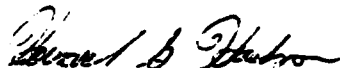
This final report was prepared by Dikewood Industries, Inc., Albuquerque, New Mexico, under Contract F29601-78-C-0045, Job Order 37630274 with the Air Force Weapons Laboratory, Kirtland Air Force Base, New Mexico. Captain Howard G. Hudson (NTYE) was the Laboratory Project Officer-in-Charge.

When US Government drawings, specifications, or other data are used for any purpose other than a definitely related Government procurement operation, the Government thereby incurs no responsibility nor any obligation whatsoever, and the fact that the Government may have formulated, furnished, or in any way supplied the said drawings, specifications, or other data, is not to be regarded by implication or otherwise, as in any manner licensing the holder or any other person or corporation, or conveying any rights or permission to manufacture, use, or sell any patented invention that may in any way be related thereto.

This report has been authored by a contractor of the United States Government. The United States Government retains a nonexclusive, royalty-free license to publish or reproduce the material contained herein, or allow others to do so, for the United States Government purposes.

This report has been reviewed by the Public Affairs Office and is releasable to the National Technical Information Service (NTIS). At NTIS, it will be available to the general public, including foreign nations.


This technical report has been reviewed and is approved for publication.



HOWARD G. HUDSON
Captain, USAF
Project Officer


PHILIP CASTILLO, PhD
Chief, Electromagnetics Branch

FOR THE DIRECTOR



THOMAS W. CIAMBRONE
Colonel, USAF
Chief, Applied Physics Division

DO NOT RETURN THIS COPY. RETAIN OR DESTROY.

UNCLASSIFIED

SECURITY CLASSIFICATION OF THIS PAGE (When Data Entered)

REPORT DOCUMENTATION PAGE		READ INSTRUCTIONS BEFORE COMPLETING FORM
1. REPORT NUMBER AFWL-TR-79-139	2. GOVT ACCESSION NO. AD-A086 844	3. RECIPIENT'S CATALOG NUMBER
4. TITLE (and Subtitle) PARALLEL-PLATE TRANSMISSION LINE TYPE OF EMP SIMULATORS: SYSTEMATIC REVIEW AND RECOMMENDATIONS		5. TYPE OF REPORT & PERIOD COVERED Final Report
7. AUTHOR(s) D. V. Giri R. W. P. King** T. K. Liu F. M. Tesche*		6. PERFORMING ORG. REPORT NUMBER DC-FR-1299-4
9. PERFORMING ORGANIZATION NAME AND ADDRESS Dikewood Industries, Inc. 1009 Bradbury Drive, S.E. Albuquerque, NM 87106		8. CONTRACT OR GRANT NUMBER(s) F29601-78-C-0045
11. CONTROLLING OFFICE NAME AND ADDRESS Air Force Weapons Laboratory (NTYE) Kirtland Air Force Base, NM 87117		10. PROGRAM ELEMENT, PROJECT, TASK AREA & WORK UNIT NUMBERS 64711F/37630274
14. MONITORING AGENCY NAME & ADDRESS (if different from Controlling Office)		12. REPORT DATE May 1980
		13. NUMBER OF PAGES 166
		15. SECURITY CLASS. (of this report) Unclassified
		15a. DECLASSIFICATION/DOWNGRADING SCHEDULE
16. DISTRIBUTION STATEMENT (of this Report) Approved for public release; distribution unlimited.		
17. DISTRIBUTION STATEMENT (of the abstract entered in Block 20, if different from Report)		
18. SUPPLEMENTARY NOTES Subcontractor: *LuTech, Inc., 5301 Central Ave., N.E., Albuquerque, NM 87108. **Harvard University		
19. KEY WORDS (Continue on reverse side if necessary and identify by block number) Conical Transmission Lines EMP Pulse Generators EMP Simulators Parallel-Plate Transmission Lines		
20. ABSTRACT (Continue on reverse side if necessary and identify by block number) This report presents various aspects of the two-parallel-plate transmission line type of EMP simulator. Much of the work is the result of research efforts conducted during the last two decades at the Air Force Weapons Laboratory, and in industries/universities as well. The principal features of individual simulator components are discussed. The report also emphasizes that it is imperative to hybridize our understanding of individual components		

DD FORM 1473
1 JAN 73

UNCLASSIFIED

SECURITY CLASSIFICATION OF THIS PAGE (When Data Entered)

UNCLASSIFIED

SECURITY CLASSIFICATION OF THIS PAGE(When Data Entered)

20. ABSTRACT

so that we can draw meaningful conclusions of simulator performance as a whole.

UNCLASSIFIED

SECURITY CLASSIFICATION OF THIS PAGE(When Data Entered)

SUMMARY

In this report, we have attempted to summarize the various aspects of the two-parallel-plate transmission line type of EMP simulator. Much of the work, briefly reported here, is the result of research efforts during the last two decades at the Air Force Weapons Laboratory, and in industry/universities as well. It was considered useful to bring under one cover, the principal features of individual simulator components. In addition, our understanding of the performance and problems associated with the individual simulator components needs to be combined in such a manner that one can draw conclusions about the simulator performance as a whole.

To appreciate the magnitude of work that has been accomplished, the reader is encouraged to consult reference [S.1], which lists about 50 references from the EMP Notes and Memo series. However, one rapidly recognizes that the analytical/numerical efforts address relatively simpler design aspects. But in reality, practical considerations resulting in engineering compromises make the problem much harder. With these considerations in mind, we have included a section on the simulator as a whole which lists some of the problem areas while pointing out their principal features.

The approach taken in this report is to briefly summarize in various sections, the available data/results with regard to the constitutive elements of the simulator (e.g., pulser, conical and cylindrical transmission line, etc.). However, in interpreting these results in the context of the simulator proper, one has to keep in mind the implications of the approximations made in the analysis procedures. An example of these is the available results

on the propagating modes (TE, TM and TEM) in two-parallel-plate transmission lines. Being an open-structure, such modal representations are valid only in and very near the parallel plate region, while they grow unbounded as one moves away in the transverse plane. In addition, for transmission line treatment, the length of the line should at least be several times larger than separation, a condition which is not satisfied in the simulator facilities. In spite of such approximations, the modal representation of the working volume fields appears to be the best available framework for interpreting and comparing the measured fields with calculations.

We have condensed the available information on two types of pulsers (Van de Graaff and Marx) with the view of providing a working knowledge of these EMP pulsers especially to the readers concerned with electromagnetic aspects. This is followed by discussions which deal respectively with the conical and parallel-plate transmission lines. The TEM quantities (characteristic impedance and field distribution) in two-conical-plate transmission lines are well known [3.2 and 3.3], while no work has been attempted on the evaluation of non-TEM modes in the conical transmission lines. However, in the central parallel-plate region, detailed information is available on the TEM, $TE_{0\ell}$ and TM_{0n} modes. A knowledge of the properties of TEM and non-TEM modes in parallel plate transmission lines is extremely useful in understanding and interpreting the measured working volume fields.

It is impractical and prohibitively expensive to build bounded wave simulators long enough so that the reflections from unterminated line will not arrive back in

the working volume to contaminate the object response. This creates the need for a "proper" termination at the far end of the simulator. These issues are then addressed while summarizing the available theoretical and experimental studies. Furthermore, a laboratory model bounded wave simulator has been in existence since 1976 at Harvard University for controlled experimental studies, e.g., detailed field maps at specific frequencies, terminator development, simulator/object interaction, etc. Professor R.W.P. King of Harvard University (one of the authors of this report) has included a review of the experimental work.

The topic of simulator/object interaction has received some attention in the past and is reviewed. Careful experimental studies in this area are considered highly desirable.

As was pointed out repeatedly in this report, in the final analysis, we need to draw meaningful conclusions about the properties and performance of the simulator as a single electromagnetic structure. With such considerations in mind, we have listed several problem areas that merit attention in the future. Needless to say, based on value judgments, there are avenues open for cost effectively advancing this technology. The report is concluded with a list of references.

ACCESSION for		
NTIS	White Section	<input checked="" type="checkbox"/>
DDC	Buff Section	<input type="checkbox"/>
UNANNOUNCED		<input type="checkbox"/>
JUSTIFICATION _____		
BY _____		
DISTRIBUTION/AVAILABILITY CODES		
Dist.	AVAIL.	and/or SPECIAL
A		

PREFACE

In compiling a document of this nature, we are deeply indebted to many individuals whose published work has been freely used. Drs. K.S.H. Lee and C.E. Baum have provided constant support. Special thanks are also due to Ms. Kathy Magann for her painstaking assistance during the preparation of this report.

CONTENTS

<u>Section</u>		<u>Page</u>
I	INTRODUCTION	9
II	PULSE GENERATORS	13
	II.1 Introduction	13
	II.2 Van de Graaf Pulse Generator	15
	a) Energy storage	16
	b) Voltage generator	19
	c) Output switch	20
	d) Output section	20
	e) Pulser equivalent circuit	20
	II.3 Marx Generator	22
	a) Equivalent circuit	25
III	CONICAL-PLATE TRANSMISSION LINES	31
	III.1 Impedance	33
	III.2 Fields	39
IV	PARALLEL-PLATE TRANSMISSION LINES	45
	IV.1 Introduction	45
	IV.2 Infinitely Wide and Infinitely Long Parallel Plates	47
	IV.3 Finitely Wide and Infinitely Long Parallel Plates	50
	a) TEM Mode	52
	b) Non-TEM Modes	56
	IV.4 Source Excitation	67
	IV.5 Experimental Results	70
	IV.6 Modal Representation of Measured Fields	72

V	TERMINATIONS FOR THE SIMULATORS	80
	V.1 Introduction	80
	V.2 Values of the Terminating Elements	81
	V.3 Idealized Analyses	83
	V.4 Practical Considerations	87
	V.5 Experimental Evaluation and Optimization	92
	V.6 Example	93
	V.7 Recommendations	96
VI	A REVIEW OF AVAILABLE EXPERIMENTAL WORK	98
	VI.1 Introduction	98
	VI.2 The Harvard EMP Simulator	99
	VI.3 Preliminary Measurements	103
	VI.4 Introductory Description of the Field in the Parallel-Plate Region	108
	VI.5 The Field in the Parallel-Plate Section; TEM and TM Modes	112
	VI.6 The Measured Field in the Working Volume; $b = 2.25\lambda = 108 \text{ cm}$, $f = 626.5 \text{ MHz}$	118
	VI.7 The Measured Field in the Working Volume; $b = 0.66\lambda = 75 \text{ cm}$, $f = 264 \text{ MHz}$	127
	VI.8 The Transverse Variation of the Electric Field; TE Modes	127
	VI.9 The Actual Electromagnetic Field in the Simulator as an Approximation of a Plane Wave	129
	VI.10 Possible Methods to Improve the Field in the Simulator as an Approximation of a Traveling Plane Wave	133
VII	SIMULATOR/OBJECT INTERACTION	137
	VII.1 Introduction	137
	VII.2 SEM Representation	139
	VII.3 Fields near the Test Object	148

VIII	SIMULATOR AS A WHOLE	154
	VIII.1 Problems List	155
	VIII.2 Brief Discussion of Salient Features of Listed Problems	156
	REFERENCES	160

I INTRODUCTION

Bounded wave EMP simulators, of the two-parallel-plate transmission line type, are complex electromagnetic structures that should be analyzed in their entirety. In view of the difficulties in analyzing a structure like ALECS (one plate above a ground plane; vertically polarized electric field) or ATLAS I (also called TRESTLE with two parallel plates; horizontally polarized electric field), various analytical/numerical efforts in the past have addressed relatively simpler structures which are idealized versions of individual simulator components. An example of this is the short (length not too large compared to separation), central parallel plate region which is treated as a finitely wide, two-parallel-plate transmission line. It is essential, however, to put together our understanding of individual components in a manner that helps us in evaluating the overall performance of the simulator.

We have attempted in the initial sections (II thru V) of this report, to briefly summarize the principal results of the treatments of individual simulator components. Figure 1.1 shows a schematic of a parallel plate transmission line type of EMP simulator comprised (from right to left) of a pulser, wave launcher, central parallel plate region, wave receptor and a terminator. The planning and design of the facility would naturally have started from the central parallel plate region and evolved toward the pulser on the input side, and the terminator on the output side. However, this report is organized in a different manner from the way the simulator thinking has evolved. After this introductory section, we have essentially followed the simulator components starting from the pulser in Section II and following the direction of propagation of the wave, i.e.,

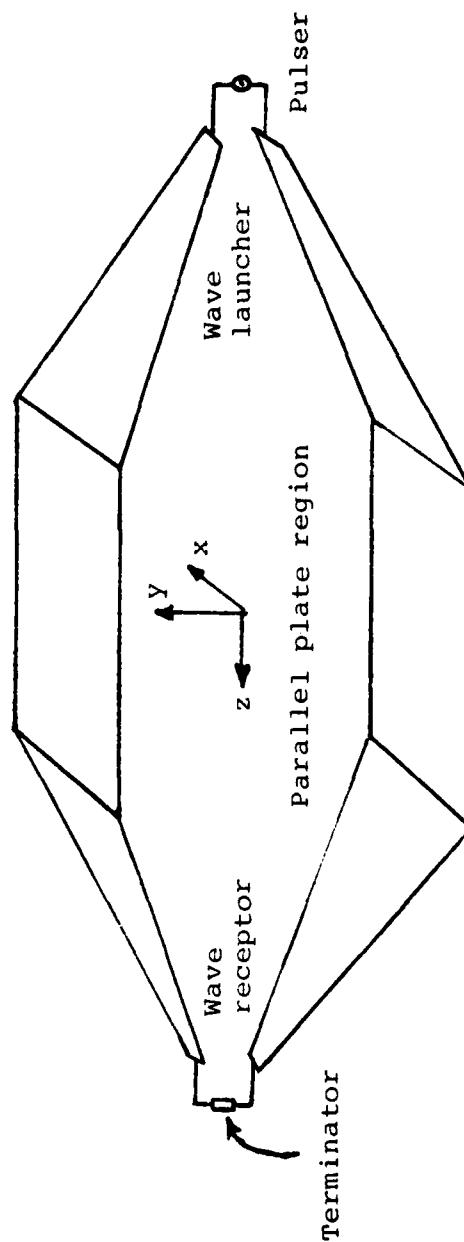


Figure 1.1 Schematic of a parallel plate transmission line type of EMP simulator

conical transmission line (wave launcher and receptor sections), parallel plate transmission line and the terminator.

Specifically, in Section II, we have condensed the available data on the Van de Graaff pulse generator (used, for instance, in the ARES facility) and the Marx pulse generator employed in the ATLAS I facility. This section furnishes a working knowledge of these two types of pulse generators for readers interested in electromagnetic aspects of the facilities (ALECS, ARES, ATLAS I and II). Section III discusses the TEM characteristics of the conical transmission line. In this regard, one may note that no calculations are available on the properties of non-TEM modes in conical lines. On the other hand, detailed calculations of the TEM and non-TEM (TE and TM) modes in parallel plate transmission lines are available in the literature and summarized in Section IV. In Section V, we have reviewed the subject of terminators for this class of EMP simulators. Several theoretical treatments of perpendicular and sloped terminating sections are available for the case of infinitely wide plates. More importantly, an extensive experimental evaluation of the terminator was conducted (circa 1974) in the ALECS facility, and the results of this study are summarized here along with recommendations for future designs.

With the view of being able to perform controlled experiments, a laboratory model parallel plate EMP simulator has been in existence since 1976 at Harvard University. Some of the experiments that have been, and are being performed with this laboratory model simulator are:

- a) careful and complete field mapping in the parallel plate region,
- b) terminator development,

- c) suppression of non-TEM modes by taking advantage of the known TEM and non-TEM field distributions,
 - d) measurement of representative object responses,
 - e) simulator/object interaction studies,
 - f) evaluation of some of the trestle effects, e.g., the platform,
- etc.

In Section VI, Professor R.W.P. King (one of the authors of this report) has included a review of the presently available experimental results.

With regard to the subject of simulator/object interaction, the available theoretical work is reviewed in Section VII. One of the approaches in the past has been to use SEM representation, i.e., to trace or follow the changes in SEM parameters as one varies the relative simulator/object geometry. There appears to be no single physical parameter which can effectively quantify all of the simulator/object interaction effects. Careful and extensive experimental investigation of these effects on the laboratory model simulator is highly recommended as a future effort.

In Section VIII entitled "Simulator as a Whole" we have addressed some of the questions deserving further study to help analysts in evaluating the overall characteristics of this class of bounded wave simulators. The report is concluded with a list of references.

II PULSE GENERATORS

II.1 Introduction

From an electromagnetic point of view, considerably more is known about the simulation proper than the associated pulse power [2.1]. Generally speaking, the pulser for EMP simulators depend on the basic properties of the electrical discharge process for the design and fabrication of fast switches and other pulser components. This indicates a need for seeking answers to basic questions concerning the properties of materials used in various pulser components. In addition, from a macroscopic viewpoint, one might think of the pulser in its entirety as a wave generator responsible for producing, transporting across its own various stages, and launching on to the simulator, a travelling wave with a reasonably planar wavefront, by the time it reaches the working volume. Put differently, it is not adequate to think of the pulser as a high voltage (typically up to 5 MV), fast rising (t_{10-90} of < 20 ns) pulse generator. It is imperative to consider and, in some sense, optimize the properties of wave transport across various stages/interfaces within the pulser via the considerations of spatial, temporal and spectral content of the waveform. An example of such considerations lies in assuring proper wave matching (both in impedance and field) in and between various Marx pulser elements, namely the output switch and its interface with the central Marx column and peaker assembly. In the present configuration, shown in Figure 2.1 the monocone output switch has an impedance of 88Ω , as opposed to simulator or load impedance of $\sim 150\Omega$. The input impedance of the simulator, which acts as a load to the pulse generator, is largely dominated by the characteristic impedance of the principal TEM mode owing to the fact

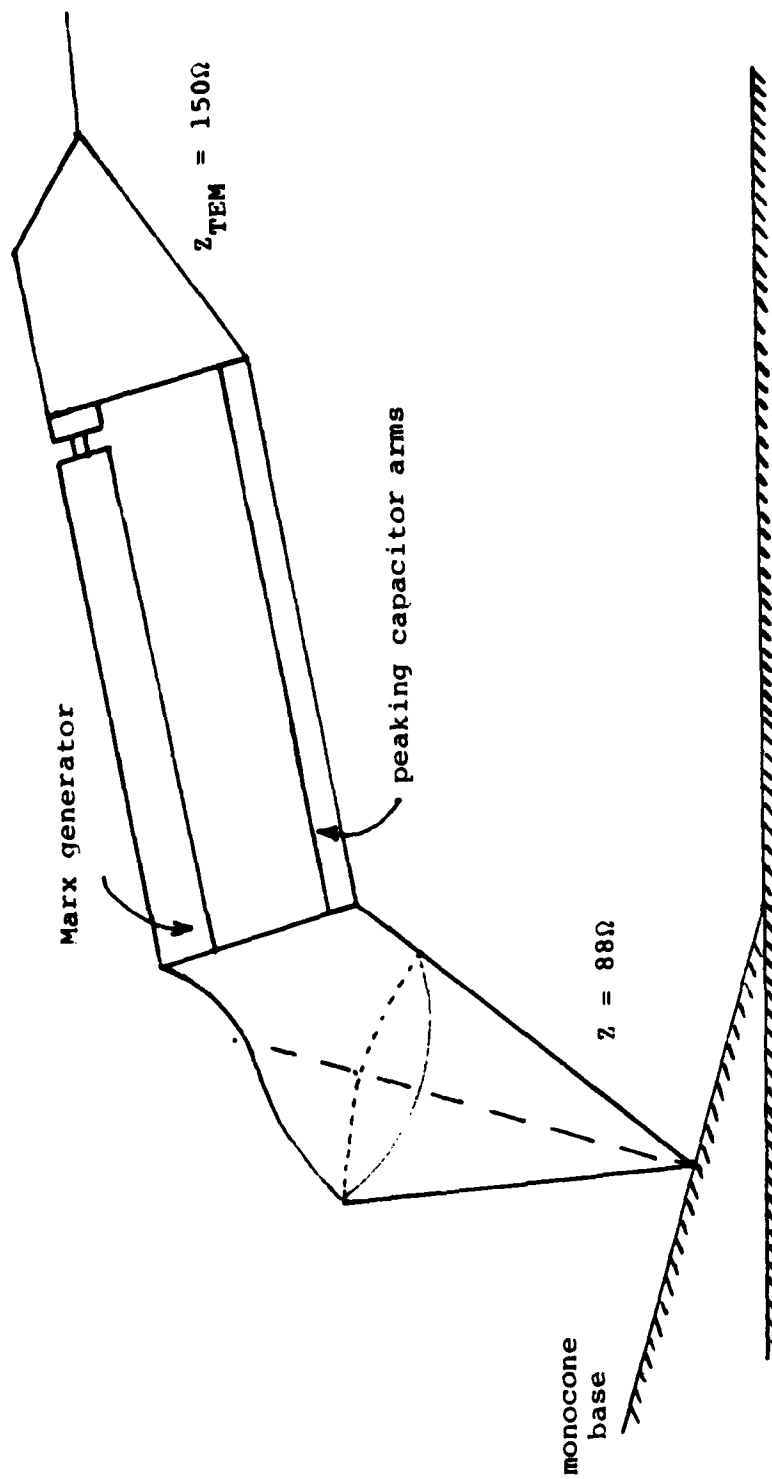


Figure 2.1. The pulse generator (present configuration)

that the non-TEM modes do not propagate near both ends of the simulator. Hence, it is desirable to maintain a constant impedance $\approx Z_c^{TEM}$ of the simulator across the various pulser elements, in addition to minimizing field discontinuities across junctions and interfaces. Presently, work is just being commenced by LuTech personnel under a separate effort, that specifically addresses such wave matching questions. The approach being followed is:

- (1) to investigate ways of increasing the impedance of the output monocone switch from its present value of 88Ω ,
- (2) to optimize the number and location of peaker arms and
- (3) to understand the properties of wave transport on the Marx column by modeling the Marx-peaker assembly by coupled transmission lines. The results of this study are expected to yield design curves and tables useful in future pulser design and possibly in suggesting modification to existing pulser designs.

The two types of pulse generators that have been used for the bounded wave simulators are Van de Graaff (ARES facility) and Marx (ATLAS I facility). In the remainder of this section, we shall briefly summarize the principal features of these two types of pulse generators [2.2, 2.3 and 2.4].

II.2 Van de Graaff Pulse Generator

Basically this ARES pulser is a dc charged system employing a coaxial gas line capacitance, relying on proven Van de Graaff and flash X-ray machine technology [2.2]. The pulse generator is a combination of the individual elements, viz., energy store, voltage generator, output switch and the output section. The pulser assembly is

schematically sketched in Figure 2.2, showing the various elements. At the output end, the transition departs from coaxial geometry and fans into a stripline, with an appropriate characteristic impedance controlled by spacing to width ratio. The edges of the stripline are curved to prevent flashover. The insulating medium also transitions from oil \rightarrow SF_6 at 1 atmospheric pressure \rightarrow air. This coaxial gas line design is a low impedance (15 to 20 Ω) source wherein the energy is stored and discharged directly into the ARES input conic section. The idealized staircase waveform, by discharging a 15 Ω source into ARES ($Z_c \approx 125\Omega$), approximates the desired pulse shape as shown in Figure 2.3.

The electrical and mechanical characteristics of the main pulser components are reproduced below from Reference [2.2] compiled by Ion Physics Corporation personnel.

a) Energy storage

This is accomplished in a simple coaxial structure ($\sim 15\Omega$ characteristic Z_{store} impedance) formed by the cylindrical pressure vessel wall and an inner cylindrical assembly supported by and directly coupled to the Van de Graaff voltage generator as illustrated in Figure 2.2. The characteristics of this coaxial line storage are as follows:

Effective Outer Diameter	Nominal 3.35 m
Effective Inner Diameter	Nominal 2.59 m
Characteristic Impedance	Nominal 15.5 Ω
Physical Length	Nominal 8.53 m
Electrical Length (Double Transit)	Nominal 54×10^{-9} s
Total Pressure, Dielectric Gas Mixture	$\dagger 300$ psig

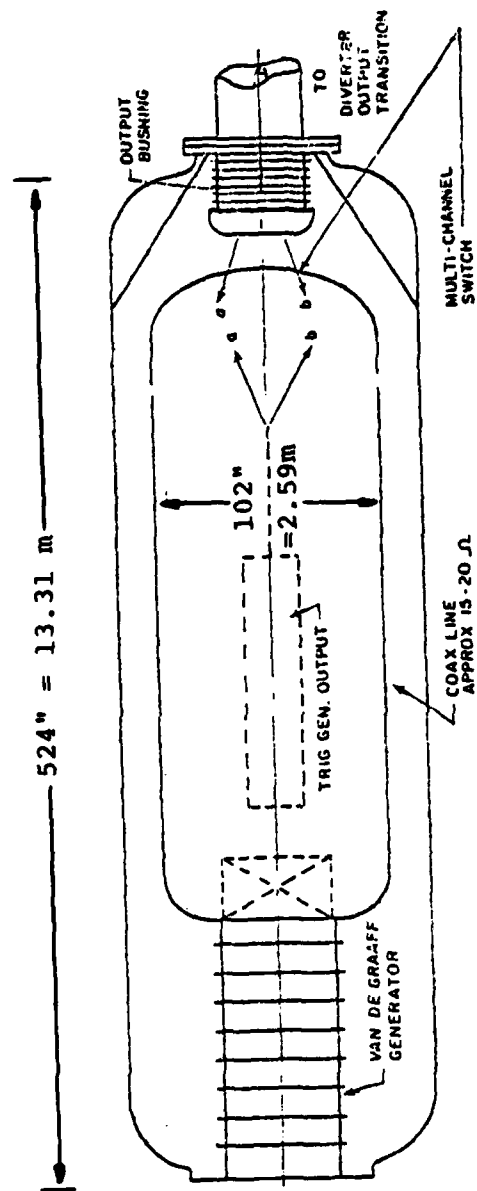


Figure 2.2. Main assembly of ARES pulser

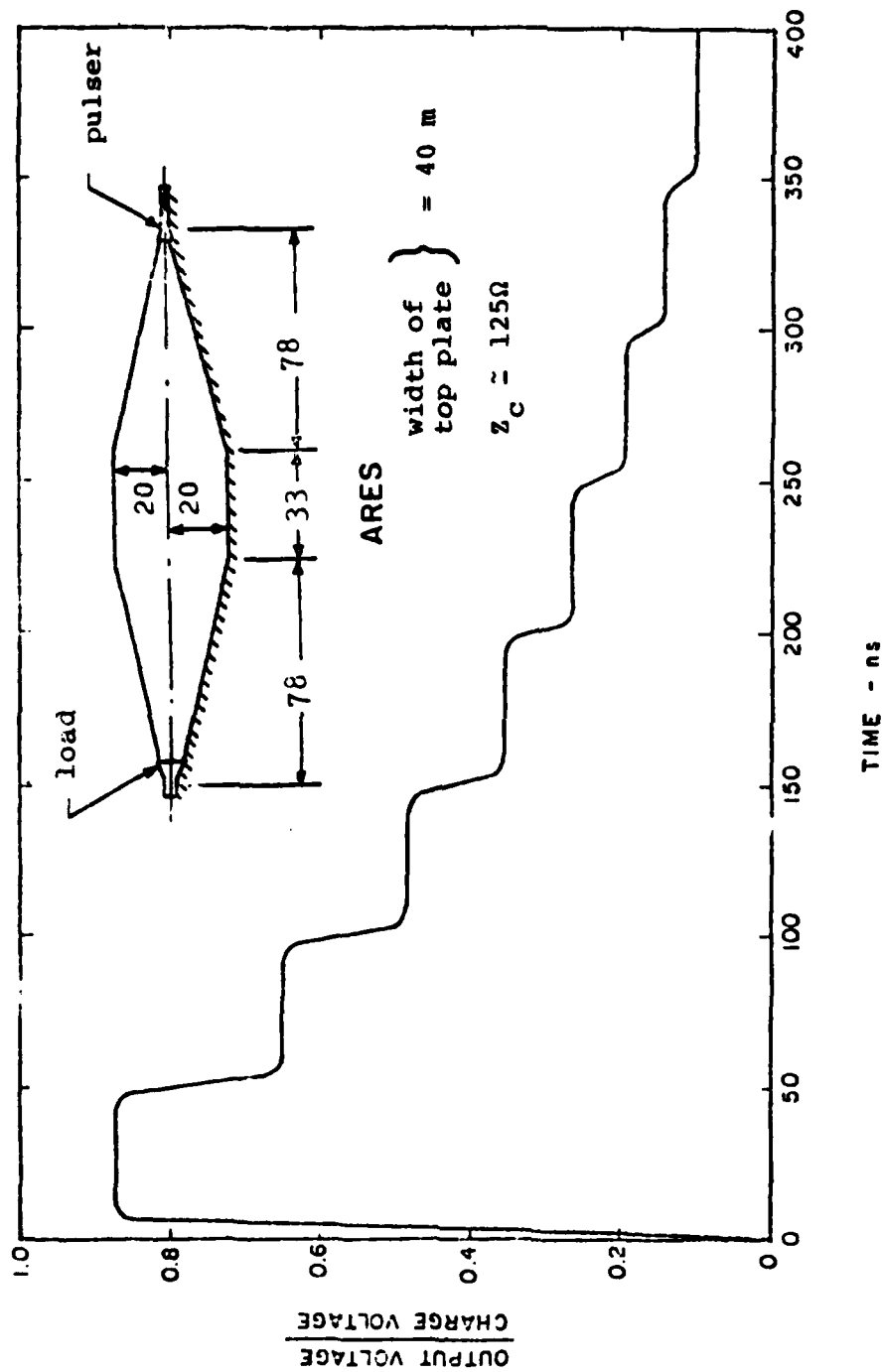


Figure 2.3. Idealized discharge characteristics of a mismatched gas line (15Ω source discharging into 125Ω load) approximates the desired pulse

Partial Pressures -	80% N ₂ : 20% CO ₂
Optional	95% N ₂ : 5% SF ₆
Storage Charge Voltage at 4.5 MV Load	5.06 MV (Nominal)
Electrical, Radial Stress at 5.06 MV Charge	15 MV/m
Predicted Maximum Radial Stress	≈19 MV/m
Total Capacitance of Store	≈2000 pF
Energy Stored at 5 MV Charge	25 kJ

b) Voltage generator

It is evident that the voltage generator must, at a minimum, charge the store capacitance of 2000 pF to a voltage of 5 MV in a satisfactory operational time. The voltage generator has the following characteristics:

Generation Method	Van de Graaff Generator Single Belt (Option for Two)
Polarity	Positive or Negative
Belt Width	21.0 Inches (Effective ≈10 Inches)
Belt Speed	530 in/s
Maximum Belt Charge	≈10 ⁻⁷ C/square inch
Maximum Charge Rate	550 μA
Charge Rate for a 30-s Charge Time	330 μA
Insulating Column Length	7 ft
Maximum Stress per Unit Length	1 MV/ft
Working Stress at 5 MV	0.71 MV/ft

The generator is both capacitively and resistively voltage graded. The resistors which are 1% components are also used to monitor the generator voltage as a check on the generating voltmeter.

c) Output switch

It is an important feature of dc charged generators that only a single switch is needed between the energy store and the operating load. In the present configuration, this switch is formed by the end of the energy storage terminal and the output bushing cap. The switch gap length may be continuously varied from 1.5 to 15 inches. The switching is accomplished by a system of trigger pulse generators and amplifiers on light signal command from a light source operating external to the machine.

d) Output section

This is comprised of the output bushing assembly (capacitively graded structure constructed of annular insulators) and the output 125 Ω transmission line that provides the necessary interface between the pressurized gas medium to oil. Also, to facilitate controlled reduction in fall time to 100 ns, an energy diverter is fitted into the oil line, at the leading edge of the output transition.

e) Pulser equivalent circuit

A simple circuit model for this pulse generator, neglecting stray reactances, is shown in Figure 2.4 where

C_1 \equiv capacitance of Van de Graaff column

Z_0 \equiv coaxial gas line characteristic impedance

τ \equiv one way transit time of the gas line

c \equiv speed of light in the gas line medium

C_0 \equiv output bushing capacitance

L_0 \equiv switch inductance

R_L \equiv characteristic impedance of output strip transmission line.

Circuit analysis leads to the voltage at

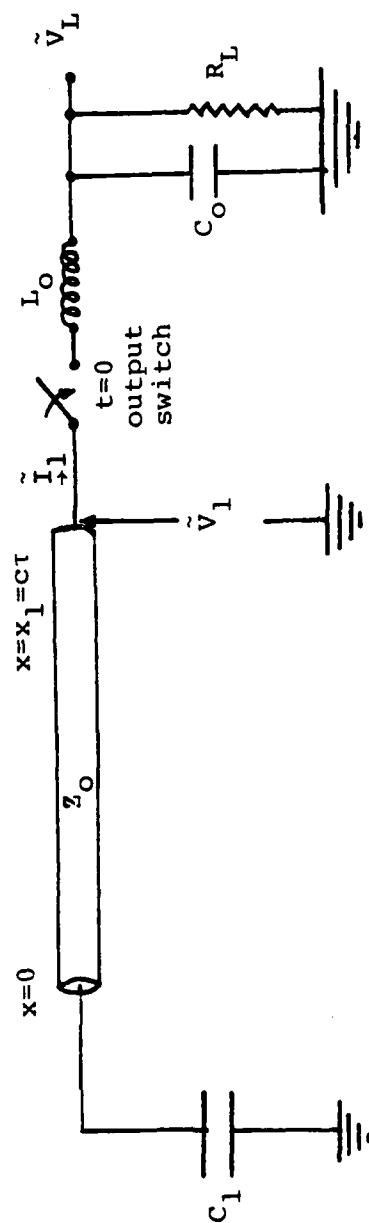


Figure 2.4. Equivalent circuit model for the Van de Graaff pulser

$$\tilde{V}_1(s) = R_L \left[1 + \frac{L_O}{R_L} + L_O C_O s^2 \right] \left(\frac{\tilde{I}_1(s)}{1 + R_L C_O s} \right) \quad (2.1)$$

where $\tilde{V}_1(s)$ and $\tilde{I}_1(s)$ are respectively voltage and current spectrum at the location $x = x_1 = c\tau$, which is the output end of the gas line. From equation (2.1), it is also possible to compute the voltage spectrum at the load $\tilde{V}_L(s)$ and convince oneself that it approximates the desired double exponential pulse. However, there is one limitation, that is, if one computes the power spectrum (proportional of $|\tilde{V}_L(s)|^2$), there are nulls in energy delivered to the simulator at specific frequencies.

II.3 Marx Generator

A schematic of the Marx-type of pulse generator, which was configured into the Pulser Testing Fixture (PTF) for evaluation purposes, is shown in Figure 2.5. It basically is comprised of an output bicone switch (can be replaced by a monocone as in Figure 2.1), the peaking capacitor arms and the Marx column along with the interconnections. The geometrical and mechanical details of all the components along with the electrical characterization of the key elements are available in Reference [2.3], which is a collection of 18 technical memoranda on the subject by Maxwell Laboratories, Inc.

In order to develop an equivalent circuit model for the Marx pulser, it is required to determine the pulser parameters that are geometry dependent as well as internal parameters. The notational details for a typical output waveform are shown in Figure 2.6, where V_c and V_p are respectively the charge and peak voltage amplitudes. The ratio (V_p/V_c) is a measure of pulser efficiency. Some of the typical problems with the pulser output waveforms, e.g.,

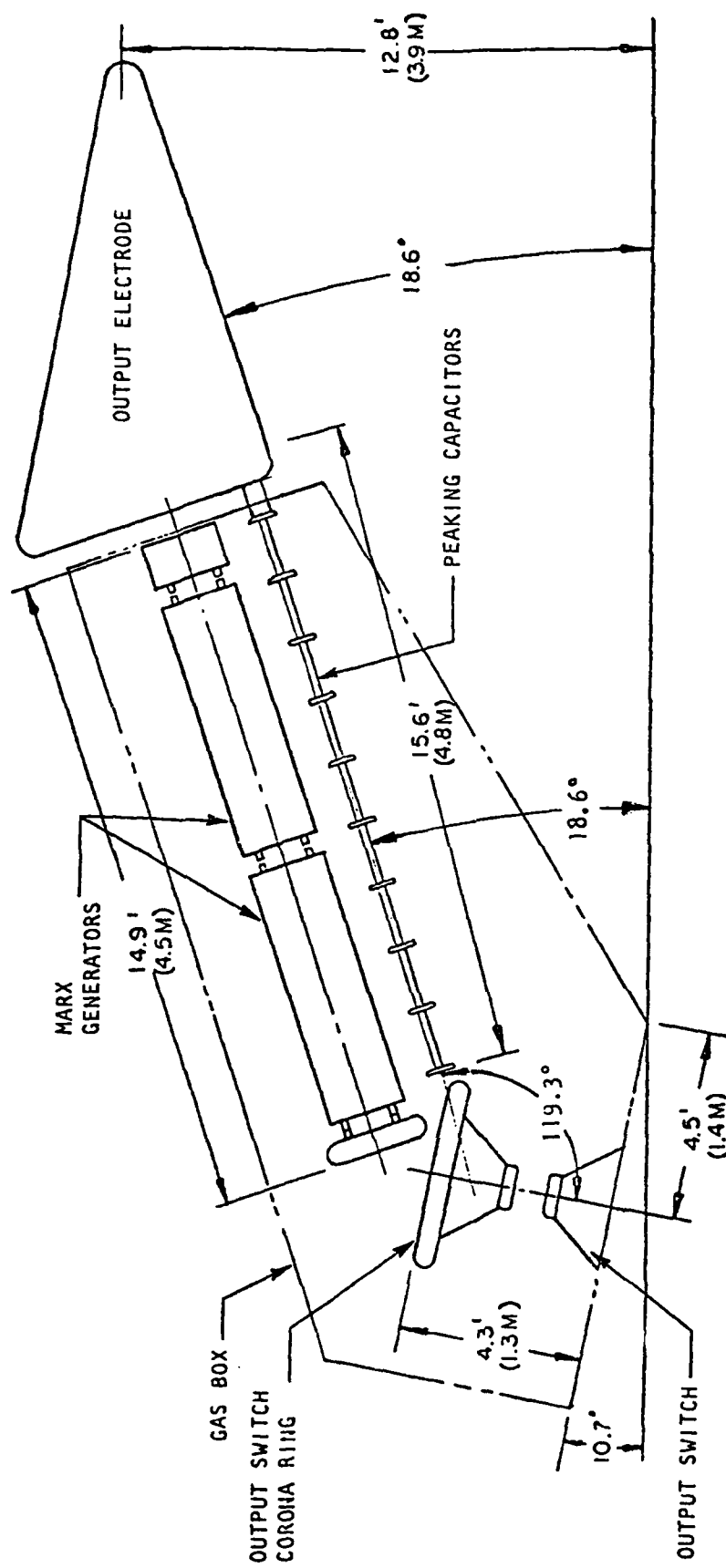


Figure 2.5. Pulser module geometry with a bicone output switch

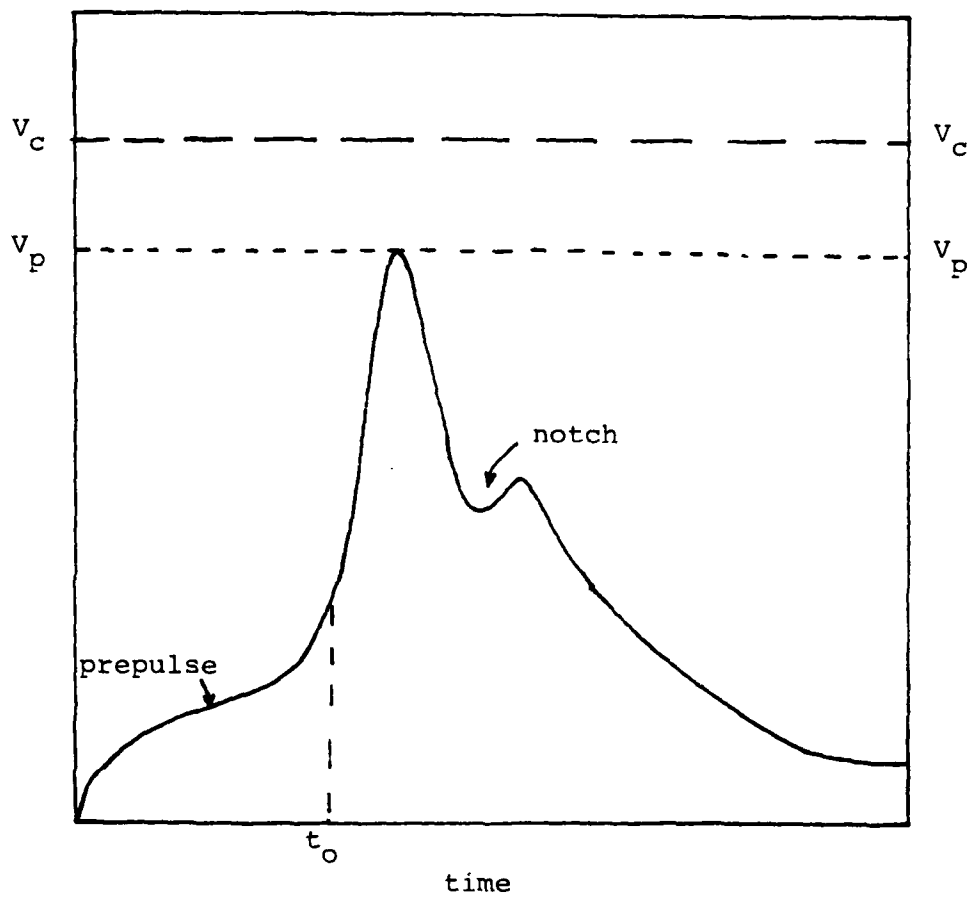


Figure 2.6. Pulser output waveform

prepulse, notch after the peak, are symbolically shown in this figure. The prepulse is the part of the output waveform that occurs prior to closing of the output (bicone or monocone) switch at a time $t = t_0$ (say).

a) Equivalent Circuit:

The equivalent circuit models for a pulser unit cell, i.e., one stage of Marx and a single peaker, are shown in Figures 2.7a and 2.7b, respectively. They comprise internal (L_M^{int} , L_P^{int}) and external (L_M^{ext} , L_P^{ext}) inductances and, likewise, internal (C_M^{int} , C_P^{int}) and external (C_M^{ext} , C_P^{ext}) capacitances. The charging resistor for each Marx stage is denoted by R_{charge} . The Marx stages and peakers also have capacitances to ground (C_{Mg} and C_{pg}) in addition to mutual or coupling capacitances C_{Mp} . All of these are either known or calculable quantities. The overall equivalent circuit consists of several Marx stages combined in series, with peaker circuits in parallel. This Marx-peaker combination, through an output switch, delivers energy to the simulator as schematically shown in Figure 2.8.

With a knowledge of the equivalent circuit elements, one can compute the pulser output waveform via transmission line theory and circuit analysis, for comparison with experimental measurements on such features as prepulse, rise time, peak amplitude, etc. From reviewing the available data, improvements in pulser performance appear possible, by initially analyzing the pulser geometry as a boundary value problem in an attempt to get a clear understanding of the properties of wave transport. Some of the relevant issues here are the optimization of the number and relative orientation of peakers, computation of pulser output waveforms in frequency and time domain, etc.

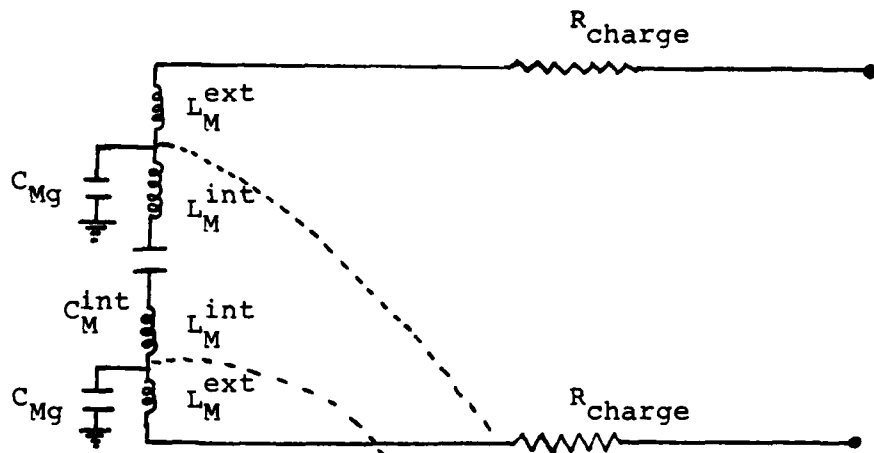


Figure 2.7a. Marx column unit cell

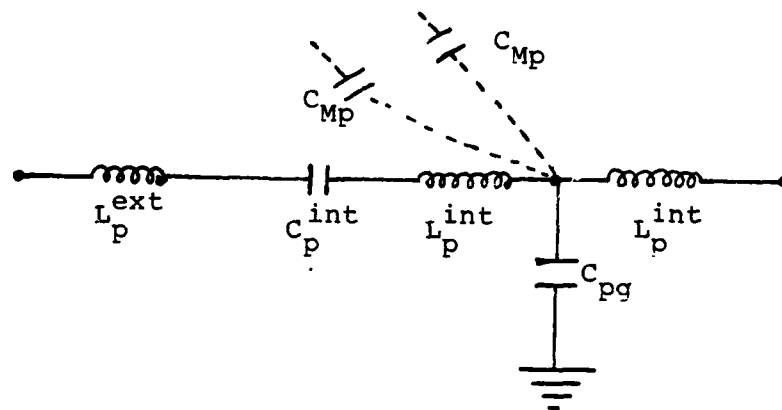


Figure 2.7b. Peaker equivalent model

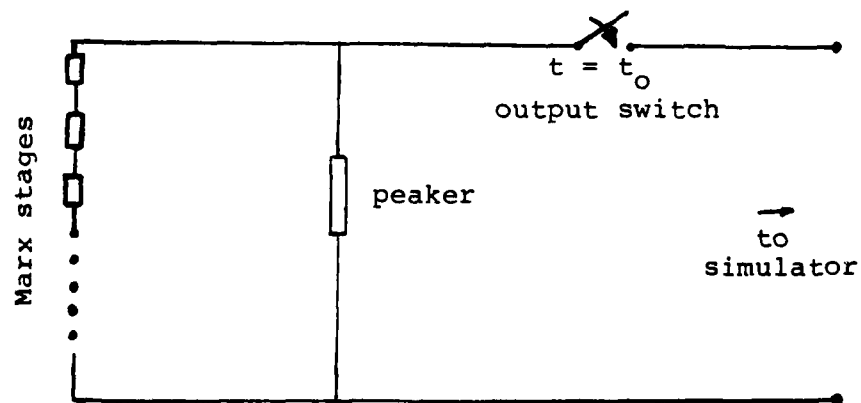


Figure 2.8. Schematic overall equivalent circuit

A similar Marx pulser system, illustrated in Figure 2.9, is being used in the ATHAMAS II or the VPD II facility. In this configuration, the peaking capacitor is physically located in and approximately co-planar with the ground plane. The water dielectric peaking capacitor feeds a uniform 60Ω monocone by way of a self closing, pressurized SF_6 gas output switch. The monocone itself is a continuous structure contained within a dielectric enclosure filled with Freon 12 gas to electrically insulate the conducting surfaces until the electric fields associated with the highest operating voltage have decreased to a low enough value. A summary of the VPD II pulse generator parameters, both physical and electrical, is given below [2.4].

Marx

1.	Erected series capacity	3.50 nF
2.	Number of stages	65
3.	Output voltage (open circuit nV_o)	6.5 MV maximum
4.	Stage capacity	228 nF
5.	dc charge voltage	100 kV maximum
6.	Stray series inductance	$\approx 6.5 \mu\text{H}$
7.	Series resistance (stray $\approx 3.5\Omega$, lumped 2.5Ω)	$\approx 6\Omega$
8.	Insultation	oil
9.	Marx switches	
	• gas type	N_2/SF_6
	• pressure	0 to 30 psig
10.	Marx output voltage range	3:1
11.	Marx erection jitter	$\leq 4 \text{ ns rms}$
12.	Marx shunt resistance	$\geq 2.8 \text{ k}\Omega$

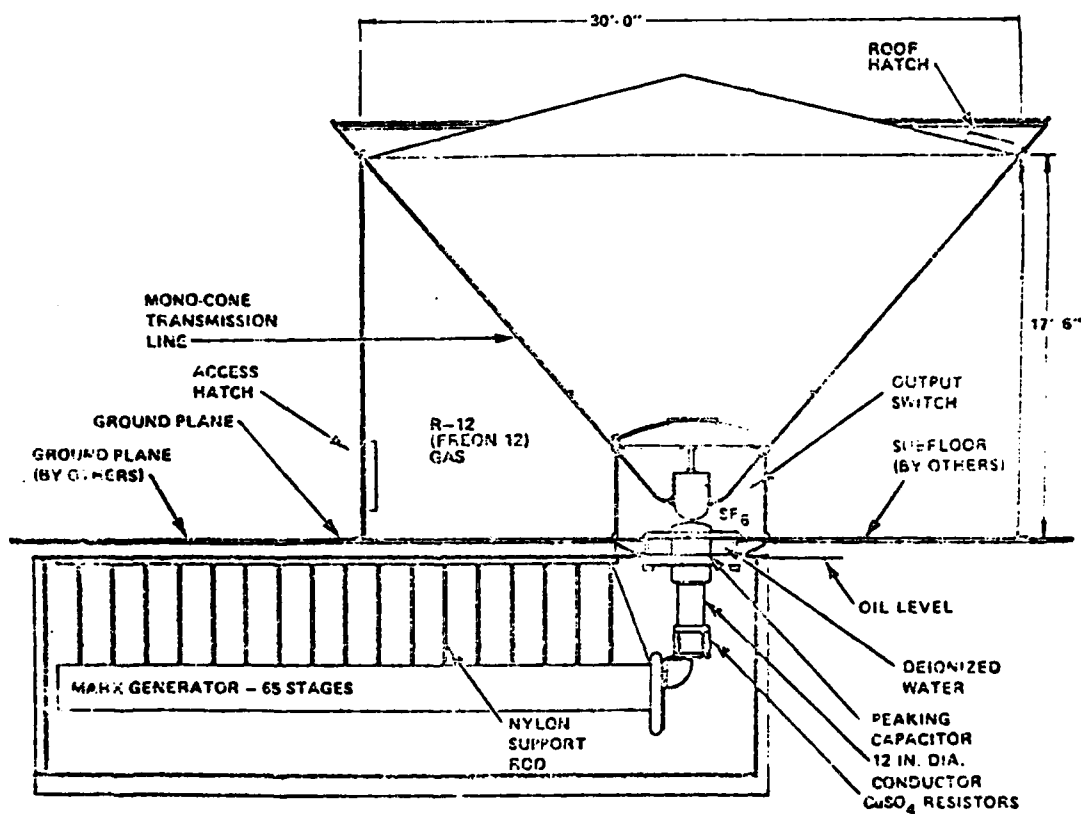


Figure 2.9. Pulser geometry in the VPD II facility

Peaking Capacitor

- | | |
|-------------------|-------------------|
| 1. Capacity | 1.2 nF |
| 2. Dielectric | water |
| 3. Wave impedance | $\cong 6.7\Omega$ |

Output Switch

- | | |
|--------------------------------|-----------------|
| 1. Gas type | SF ₆ |
| 2. Pressure | 50 psig maximum |
| 3. Breakdown voltage variation | $< \pm 5\%$ |
| 4. Breakdown time variation | $< \pm 4$ ns |
| 5. Risetime | < 8 ns |

From some of the test procedures, the following results were obtained.

Total stray series inductance of Marx and connection to peaking capacitor	7.4 μ H
Inductance of connector	0.9 μ H
Inductance of Marx	6.5 μ H
Total series resistance	6 ohms
Average shunt capacitance of Marx stage to ground	9.6 pF
Total effective value to ground	0.21 nF
Transmission time of Marx as a transmission line in oil (excluding connection to peaking cap)	63.7 ns
Impedance of equivalent Marx transmission line	102 ohms
Stray capacitance of connector	0.118 nF
Capacity of peaking cap + connector + output switch stray + Marx stray	1.95 nF
Output switch stray	50 pF
Peaking capacitor value alone	1.55 nF

With regard to the performance, typical 10% to 90% rise times are about: (1) 6 ns at $(1/3) V_{\max}$, (2) 10 ns at $(2/3) V_{\max}$ and (3) 10 ns at full voltage. The peak operational voltage was about 4 MV, although the Marx generator was designed for a maximum operating voltage of 6 MV. The present limitations appear to be confined to the dielectric capabilities of the output switch housing and the upper slab of peaking capacitor.

III CONICAL-PLATE TRANSMISSION LINES

The conical transmission lines on either side of the cylindrical transmission line (parallel plate region) serve as wave launching and receiving structures and consequently are of significant importance in the overall performance of this class of bounded wave simulators. In this section we review the conical transmission line problem in itself and defer the discussion of its compatibility with its neighboring components (viz., parallel plate transmission line, pulser, terminator) to Section VIII entitled "Simulator as a Whole."

In the class of bounded wave simulators under consideration, one has two conic sections which are commonly referred to as the input conic (wave launcher) and the output conic (wave receptor). The input conic serves to transport the electromagnetic wave from the pulser and launches it onto the parallel plate region, whereas the output conic propagates this wave to the terminating section at the far end. In either case, the conic sections are made up of two triangular shaped plates (wire meshes in practice) or, equivalently, a single triangular plate above a ground plane. The two-conical plate transmission line of interest, shown in Figure 3.1 is to be contrasted with the classically [3.1] treated conical waveguide illustrated in Figure 3.2. For lack of better nomenclature, we have referred to the two structures as conical-plate transmission line (Figure 3.1) and conical waveguide (Figure 3.2). In both cases, the natural coordinate system is the spherical coordinate system (r, θ, ϕ) with its origin at the apex. As was mentioned earlier, the treatment of the conical waveguide is available in the literature and reference [3.1] has explicit relations for the impedance and the nonvanishing field quantities (E_θ and H_ϕ). However, the finitely long conical plate

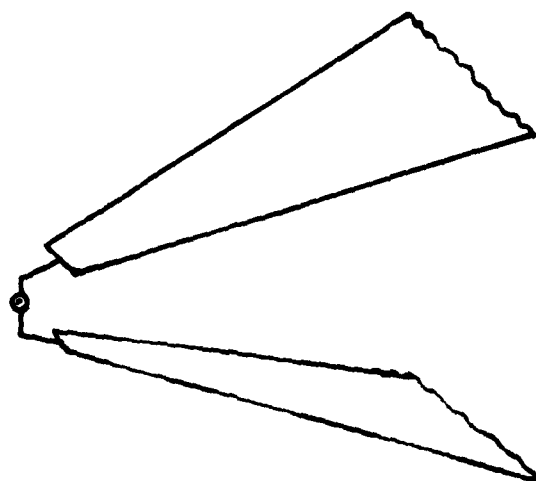


Figure 3.1. Two-conical plate transmission line

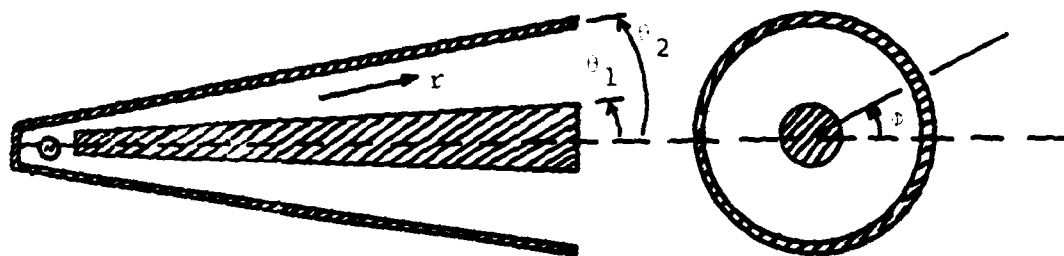


Figure 3.2. Geometry of a conical waveguide

transmission line problem (Figure 3.1) has recently received well deserved attention [3.2, 3.3]. The two references [3.2] and [3.3] respectively deal with the determination of the impedance and the field distribution of the transverse electromagnetic wave. The TEM quantities are derived by a combination of the methods of stereographic projection and conformal mapping. These methods reduce the conical plate region into a much simpler geometry for which the solution is known. We shall briefly review these calculations and follow it up with recommendations for future work.

III.1 Impedance

Impedance of the principal spherical TEM wave propagating in the two-conical-plate transmission line is an important physical parameter because of its impact on ensuring proper wave matching between the adjacent regions of conical plates and the parallel plates. It is essential to minimize the impedance and field discontinuities between all successive sections of the simulator so that undesirable reflections are reduced. However, let us postpone the discussion of this important aspect to Section VIII where we consider the simulator as a whole.

Returning to the subject of the characteristic impedance Z_{CC}^{TEM} of the principal TEM wave in the conical plate region, it is noted that extensive tables and curves are given in reference [3.2] for various cone angles and plate widths. For convenience in relating the physical quantities to those in the parallel plate region, both rectangular and spherical coordinate systems, as illustrated in Figure 3.3, are used. In the two coordinate systems, the top ("+") and bottom ("-") plates are designated by

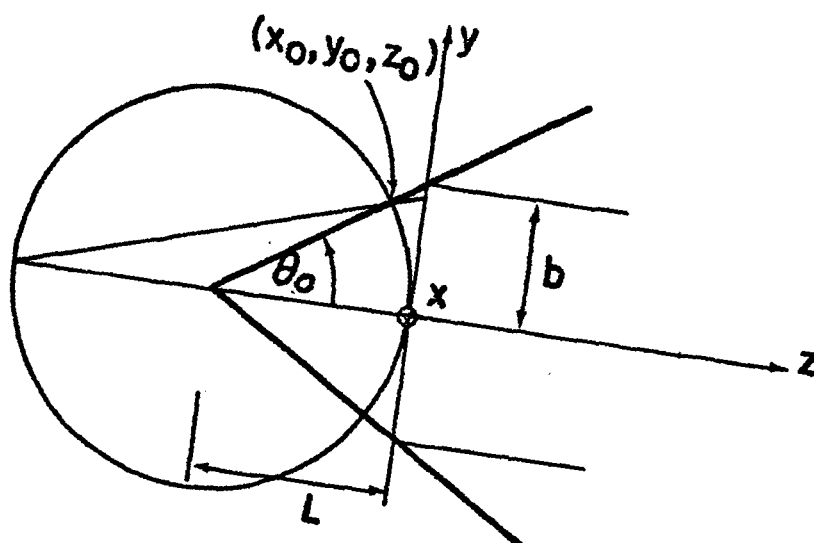
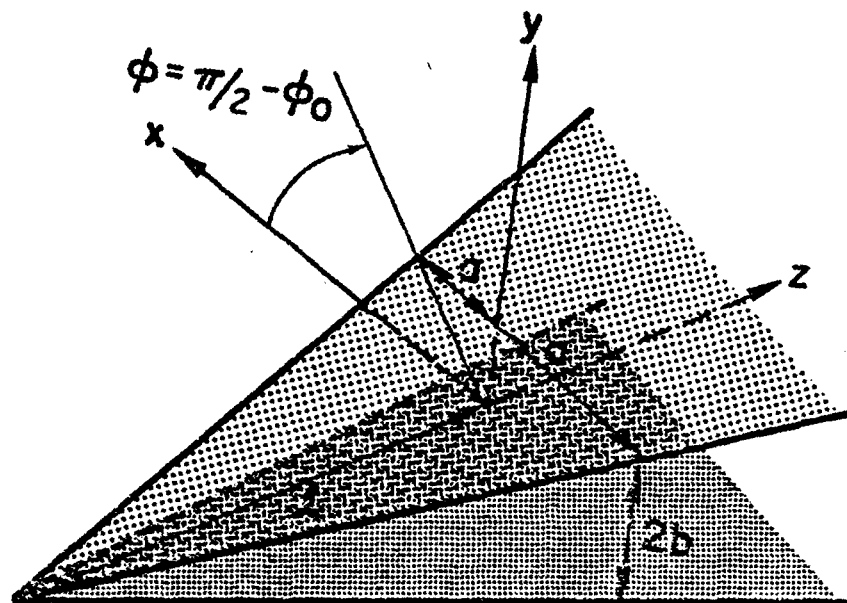


Figure 3.3. Rectangular (x, y, z) and spherical (r, θ, ϕ) coordinate systems of two conical plates

<u>rectangular (x,y,z)</u>	<u>spherical (r,θ,φ)</u>
$y = \pm b(1 + z/L)$	$\theta = \arccos[(1 + \tan^2(\theta_0) \csc^2 \phi)^{-1/2}]$
$ x/y \leq (a/b)$	$(\frac{\pi}{2} - \phi_0) \leq \phi \leq (\frac{\pi}{2} + \phi_0)$
$z + L \geq 0$	
with $\theta_0 = \arctan(b/L)$	(3.1)
$\phi_0 = \arctan(a/b)$	

The spherical TEM wave propagating in the radial (r) direction has non-zero components E_θ , E_ϕ , H_θ , and H_ϕ . The longitudinal fields vanish ($E_r = H_r = 0$) by definition, for the spherical TEM wave. The complex potential (W) of the TEM wave can be written as [3.4],

$$W(r, \theta, \phi) = [U(\theta, \phi) + i V(\theta, \phi)] \frac{e^{\gamma r}}{r} \quad (3.2)$$

with $\gamma = s/c \equiv$ propagation number and U and V satisfy the two-dimensional Laplace equation on a spherical surface

$$\sin(\theta) \frac{\partial}{\partial \theta} \left[\sin(\theta) \frac{\partial}{\partial \theta} \begin{pmatrix} U(\theta, \phi) \\ V(\theta, \phi) \end{pmatrix} \right] + \frac{\partial^2}{\partial \phi^2} \begin{pmatrix} U(\theta, \phi) \\ V(\theta, \phi) \end{pmatrix} = 0 \quad (3.3)$$

Using the following stereographic projection [3.5],

$$\begin{aligned} x &= 2L \tan(\theta/2) \cos(\phi) \\ y &= 2L \tan(\theta/2) \sin(\phi) \end{aligned} \quad (3.4)$$

equation (3.3) becomes

$$\left(\frac{\partial^2}{\partial x^2} + \frac{\partial^2}{\partial y^2} \right) U(x, y) = 0 \quad \text{and} \quad \left(\frac{\partial^2}{\partial x^2} + \frac{\partial^2}{\partial y^2} \right) V(x, y) = 0 \quad (3.5)$$

which is to be solved on the plane $z = 0$.

It can be shown [3.2], that under this stereographic projection, the two conical plates transform into two plates of circular arcs of different circles as shown in Figure 3.4.

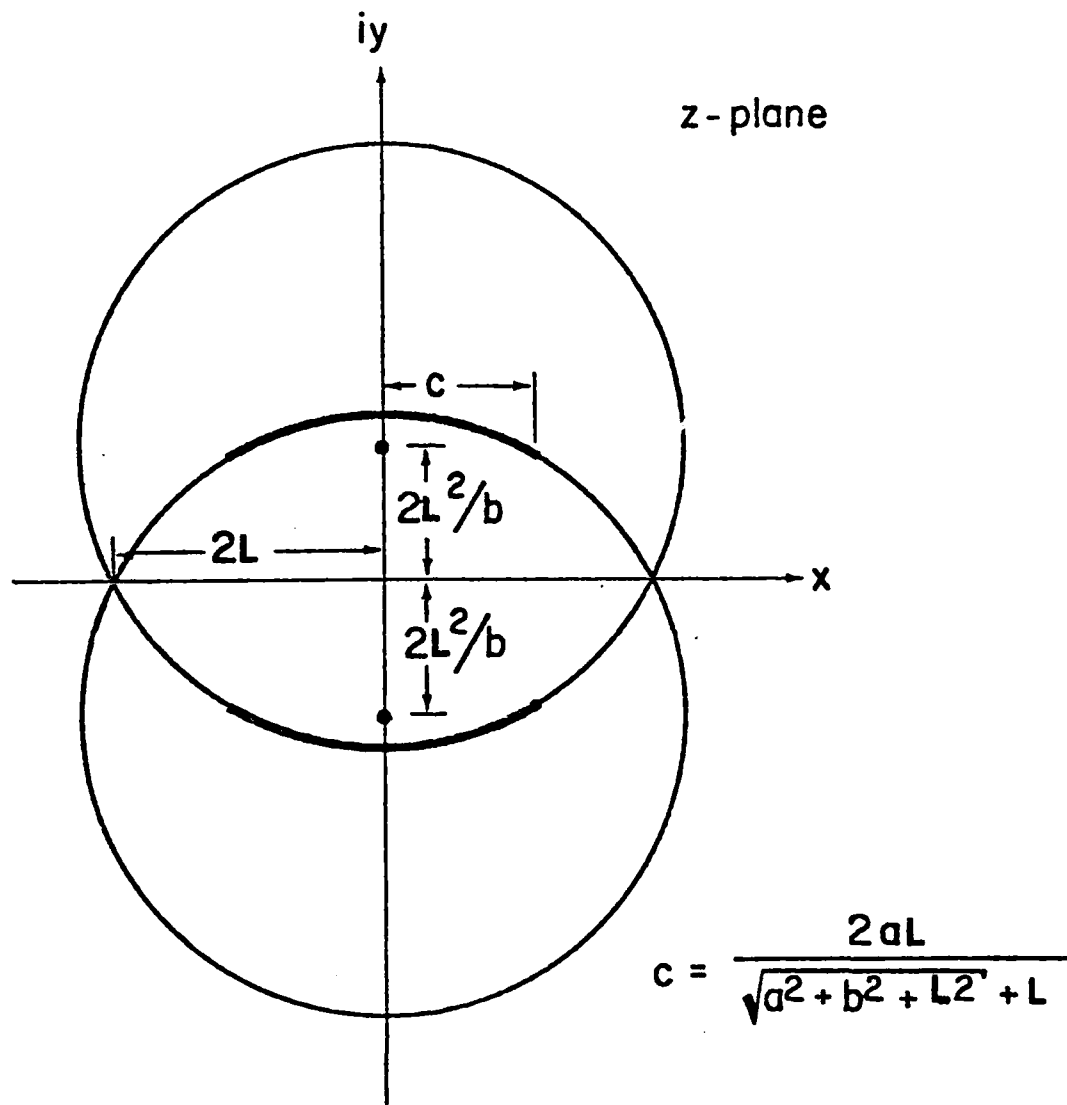


Figure 3.4. Stereographic projection of two conical plates onto two plates of circular arc

It is recognized that the characteristic impedance of the two-circular-arc plates is the same as that of the original problem and that the circular-arc-plate problem can be solved by the standard method of conformal mapping. The two-circular-arcs in the $[(x + iy) = z]$ plane are sequentially mapped into the complex potential $[U + iV = W]$ plane through a series of conformal mappings as illustrated in Figure 3.5. Note that the z -plane (not to be confused with the z -coordinate used earlier) is successively mapped as follows

$$z\text{-plane} \Rightarrow z_1\text{-plane} \Rightarrow t\text{-plane} \Rightarrow W\text{-plane}$$

Following the method developed in reference [3.2], the transformations are summarized below

$$z = 2L \tanh (z_1/2) \quad (3.6)$$

$$z_1 = C_1(u - A_1[\Pi(n;u|m) - \sqrt{n} f(m,n,u)]) + B_1 \quad (3.7)$$

$$W = C_3 u + B_3 \quad (3.8)$$

where

$$C_1 = - \sqrt{(1-n)(m-n)} / (A_1 \sqrt{n}) \quad (3.9)$$

$$B_1 = i\theta_0 \quad (3.10)$$

and m, n, A_1 are obtained by solving a system of three transcendental equations (equation (12) of [3.2]).

Also in equation (3.7), u and Π are the elliptic integrals of the first and third kinds, f is a known function of m, n and u ,

$$f(m,n,u) = \frac{1}{2\sqrt{(1-n)(m-n)}} \ln \left\{ \frac{2(1-n)(m-n) + (1-n) \operatorname{sn}^2(u)(n+nm-2m)}{n(m-1)(1-n \operatorname{sn}^2(u))} + \frac{2n\sqrt{(1-n)(m-n)} \operatorname{cn}(u) \operatorname{dn}(u)}{n(m-1)(1-n \operatorname{sn}^2(u))} \right\} \quad (3.11)$$

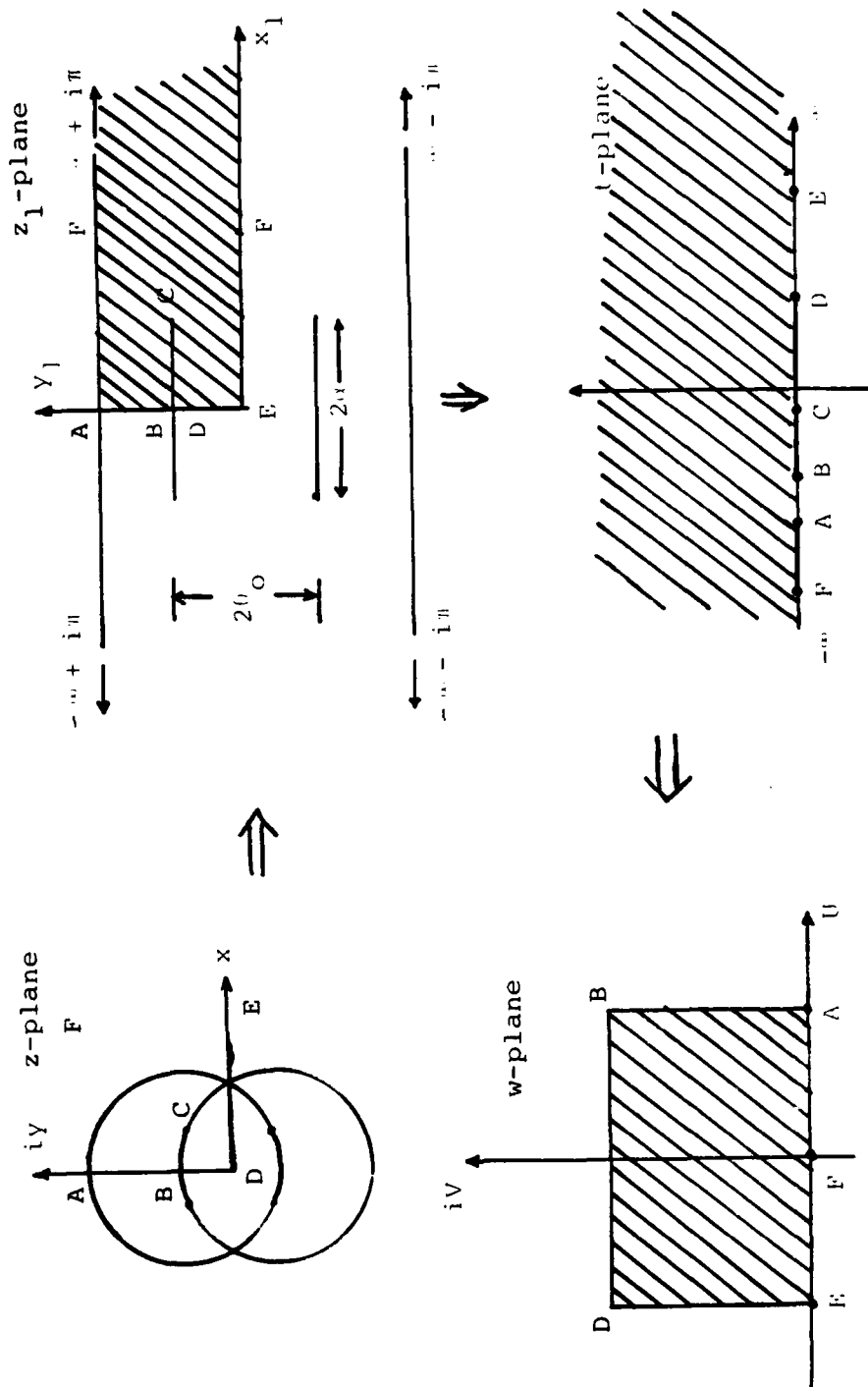


Figure 3.5. Sequential conformal mapping of the two circular-arcs into the complex potential $(U + iV)$ plane

$$t = \text{sn}(u) \quad \text{or} \quad u = \int_0^t \frac{dt'}{\sqrt{(1-t')^2(1-mt'^2)}} \quad (3.12)$$

In equation (3.8),

$$C_3 = 1/K(m) \quad (3.13)$$

$$B_3 = i K'(m)/K(m) - F(\arcsin \sqrt{n/m} | m)/K(m) \quad (3.14)$$

Finally, the geometric impedance factor f_g is given by

$$f_g = \frac{1}{2} \frac{K'(m)}{K(m)} \quad (3.15)$$

leading to the characteristic impedance of the two-conical plate

$$Z_{cc}^{TEM} = \sqrt{\frac{\mu_0}{\epsilon_0}} f_g = Z_0 \frac{1}{2} \frac{K'(m)}{K(m)} \quad (3.16)$$

with Z_0 being the characteristic impedance of free space and $K'(m)$ and $K(m)$ are the usual complete elliptic integrals. The results of the above calculations reported by Yang and Lee [3.2] are shown in Figure 3.6 and in Table 3.1.

It can be seen from Figure 3.6 that when the conical region is about four times or longer than the half separation (i.e., $L \geq 4b$), the impedance is fairly constant with respect to L/b .

III.2 Fields

The mathematical framework outlined in the preceding subsection can be logically extended [3.3] to yield the electric and magnetic field quantities of the TEM wave.

With reference to Figures 3.4 and 3.5, the field quantities are given by the gradient of the complex potential as follows:

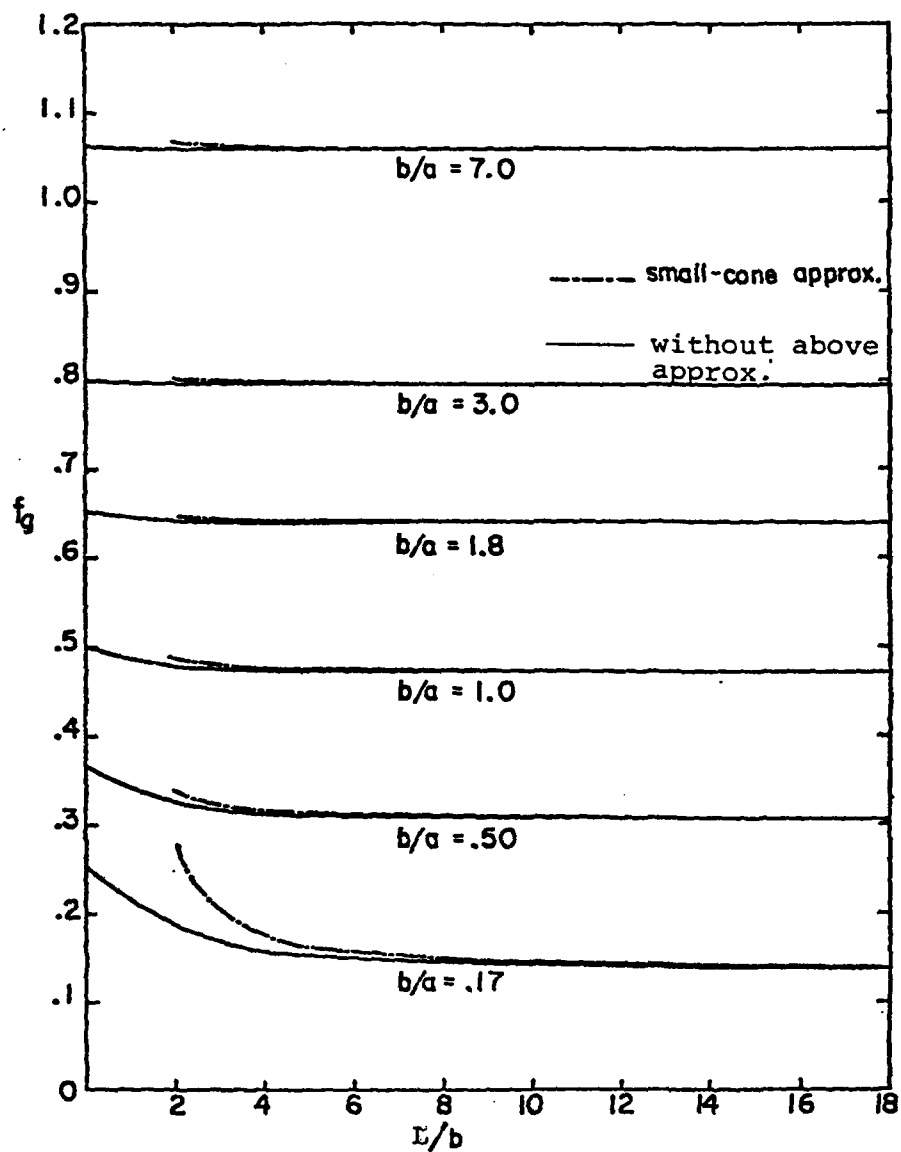


Figure 3.6. Geometric impedance factor f_g of two conical plates as a function of (L/b) with (b/a) as the running parameter

TABLE 3.1. VALUES OF THE CHARACTERISTIC IMPEDANCE Z_{CC}^{TEM} OF TWO CONICAL PLATES

L/b b/a	0.0*	1.00	1.50	2.00	2.50	3.00	3.50	3.90	4.50	5.00	10.0	** ∞
.17	93.47	82.35	75.66	70.50	66.64	63.73	61.51	60.10	58.43	57.34	52.86	50.90
.41	127.7	118.5	113.4	109.9	107.5	105.8	104.7	104.0	103.2	102.8	101.1	100.4
.50	138.5	130.2	125.8	122.8	120.8	119.5	118.6	118.1	117.5	117.1	115.9	115.4
.60	149.7	142.3	138.6	136.1	134.5	133.5	132.8	132.4	131.9	131.7	130.7	130.4
.70	160.3	153.7	150.5	148.5	147.2	146.3	145.8	145.5	145.1	144.9	144.2	143.9
.80	170.2	164.4	161.7	159.9	158.9	158.2	157.7	157.5	157.2	157.0	156.5	156.3
.90	179.5	174.4	172.1	170.6	169.7	169.2	168.8	168.6	168.4	168.2	167.8	167.6
1.00	188.4	183.9	181.8	180.6	179.8	179.4	179.1	178.9	178.7	178.6	178.2	178.0
1.20	204.7	201.1	199.6	198.7	198.1	197.8	197.5	197.4	197.3	197.2	196.9	196.8
1.24	207.8	204.4	202.9	202.0	201.5	201.2	201.0	200.8	200.7	200.6	200.4	200.3
1.40	219.4	216.6	215.4	214.7	214.2	214.0	213.8	213.7	213.6	213.5	213.3	213.3
1.60	232.8	230.5	229.5	229.0	228.6	228.4	228.3	228.2	228.1	228.1	227.9	227.9
1.80	245.0	243.1	242.3	241.8	241.6	241.4	241.3	241.2	241.2	241.1	241.0	241.0
2.00	256.2	254.6	253.9	253.6	253.3	253.2	253.1	253.1	253.0	253.0	252.9	252.9
2.50	280.6	279.6	279.1	278.9	278.7	278.6	278.6	278.6	278.5	278.5	278.4	278.4
3.00	301.2	300.4	300.1	299.9	299.8	299.8	299.7	299.7	299.7	299.7	299.6	299.6
7.00	400.2	400.0	400.0	400.0	399.9	399.9	399.9	399.9	399.9	399.9	399.9	399.9

* Two planar conical plates ** Two parallel plates

$$\begin{aligned}\text{Complex field} &= \frac{dW}{dz} = \frac{\partial U}{\partial x} + i \frac{\partial V}{\partial y} = -(E_y + i E_x) \\ &= Z_0 (H_x - i H_y)\end{aligned}\quad (3.17)$$

Since the complex potential W is known, the field quantities are determined in a straightforward manner although the numerical evaluation is somewhat tedious. One example is shown in Figure 3.7 for the case of $\sim 103\Omega$ characteristic impedance. In this figure, contours of electric and magnetic field lines are shown for the two-circular-arc plates. The discontinuities across the plate in the normal electric field (E_y) and the tangential magnetic field (H_x) account respectively for the TEM charge and current distribution on the top plate. It is important to note that the fields plotted in Figure 3.7 are for the circular arc plates and need to be transformed back to the conical plate region. Using the stereographic projection of equation (3.4), one can write down and compute the field quantities in the spherical (r, θ, ϕ) coordinates, which is a natural coordinate system for the conical plate region. Since the EM fields in the conical plate serve to excite the parallel plate region where the natural coordinate system is the rectangular coordinates, it is useful to think of the fields in the conical region (say at the plane $z = 0$) in its rectangular components. At the $z = 0$ plane, the relationship between the field components of the TEM wave on the curved plates (Figure 3.7) and the field components of the TEM wave on the conical plates is given by

$$\begin{aligned}\vec{E}(x, y, z) &= L_c \cdot L_s \cdot \vec{E}_{\text{curved plates}} \\ \vec{H}(x, y, z) &= L_c \cdot L_s \cdot \vec{H}_{\text{curved plates}}\end{aligned}\quad (3.18)$$

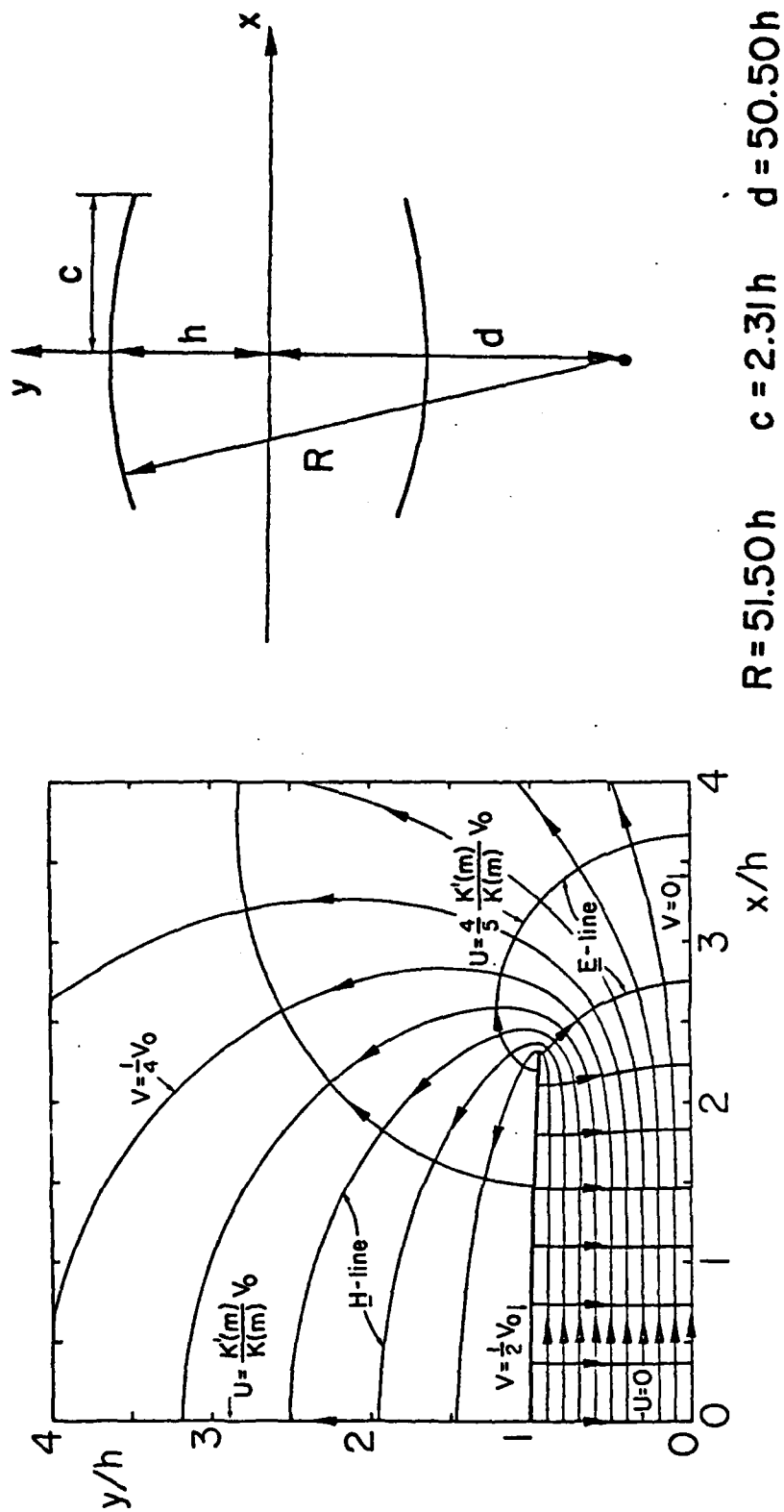


Figure 3.7. Field lines of the TEM mode for $R = 51.50h$, $c = 2.31h$, and $d = 50.50h$. The characteristic impedance of the transmission line Z_c is 102.8Ω

with

$$L_s = \begin{pmatrix} \cos(\phi) & \sin(\phi) \\ -\sin(\phi) & \cos(\phi) \end{pmatrix} L \sec^2(\theta/2) \quad (3.19a)$$

and

$$L_c = \begin{pmatrix} \cos(\theta) \cos(\phi) & -\sin(\phi) \\ \cos(\theta) \sin(\phi) & \cos(\phi) \\ -\sin(\theta) & 0 \end{pmatrix} \begin{pmatrix} e^{-\gamma r} \\ r \end{pmatrix} \quad (3.19b)$$

Representative plots of these rectangular field components are available [3.3] and show that the fields are mainly concentrated in the region between the conical plates.

C. Future Work

The subject of non-TEM modes in the conical region has not been addressed to date, and certainly merits attention. After analyzing the higher order mode propagation in the conical plate region, we could explore the feasibility of incorporating suitable design modifications in the simulators to suppress any dominant, i.e., comparable in strength to the TEM mode, higher order modes. One can also identify problems needing attention with regard to the wave matching of the input conical plate transmission line with the pulse generator on one side and the two-parallel plate transmission line on the other side. However, we shall include these problems in Section VIII where they are more appropriate.

IV PARALLEL-PLATE TRANSMISSION LINE

IV.1 Introduction

The central parallel-plate region in this class of bounded wave simulators is the key electromagnetic component in the simulator because it is largely in this region that one attempts to simulate the threat-like NEMP environment for meaningful testing of aircraft systems. Ideally, what is desired is a planar traveling pulse that uniformly illuminates the aircraft and is properly terminated at the other end. What makes the problem hard is that the spectral content of the desired pulse is such that the plate separation (2b) extends from being small fractions of wavelength to several wavelengths. Consequently, if one conceptually divides the frequency regime of interest into low, intermediate and high frequencies, the simulator is, respectively, a transmission line, a radiator, and an optical diffracting structure in the three frequency regimes. At low frequencies, critical dimensions of the simulator are small compared to the wavelengths and, hence, the structure behaves like a transmission line with quasistatic considerations becoming applicable. In the intermediate frequency region, the dimensions are of the order of the wavelength and the structure behaves partially like an antenna. As the frequency is further increased with the structural dimensions becoming several wavelengths, one can resort to ray-optic methods for estimating the fields.

Since the incident pulse encompasses a wide range of frequencies, one can recognize that at late times (>1000 ns), the working volume fields asymptotically approach the TEM values. However, at any given frequency, the measured fields in the working volume can be represented as a result

of the superposition of parallel-plate transmission line modes. This representation appears to be the best available mathematical framework for interpreting and understanding the working volume fields. In view of these considerations, a lot of emphasis has been placed, in the past, on the analysis of TEM and non-TEM modes in finitely wide two-parallel-plate transmission lines. In making use of such modal representations, one has to be aware of the implicit assumptions/limitations. For example, the theoretical treatments that determine TEM and non-TEM modes are for infinitely long, finitely wide transmission lines and, in practice, the length of the central parallel-plate region is not even several times the separation. In addition, being an open transmission line, for complete representation one needs to include the continuous spectrum. In other words, the currents on the simulator plates can be expressed as an infinite sum added to an infinite integral. The sum represents the discrete spectrum, each term corresponding to a propagating mode (TEM and non-TEM) while the integral comes from the contributions of the continuous spectrum. It is also important to note that the discrete spectrum in open waveguides, unlike those in the closed waveguides, is not square integrable in a cross section. The fields do satisfy source-free Maxwell's equations and the boundary conditions on simulator plates, but are unbounded as one moves away in the transverse plane. The total field, comprised of the discrete and continuous spectra, however, is bounded and possesses finite amounts of energy. Although a lot of information is currently available on the discrete spectrum, much work still needs to be done on the contributions of the continuous spectrum. Despite such limitations and approximations, we still can think of the simulator working

volume fields at any given frequency as a superposition of the principal TEM and, typically, a few non-TEM modes. In view of these considerations, the main emphasis in this section is placed on reviewing the available methods of evaluating these modes and also on being able to represent the measured fields in terms of their superposition.

A simple and straightforward way of calculating these modes is to take the classically derived fields in a rectangular waveguide and let the width go to infinity [4.1]. When the width is finite, conformal mapping techniques [4.2, 4.3 and 4.4] are useful in calculating the TEM mode characteristics. Integral equation formulations and efficient numerical analysis procedures in Fourier transform domain have been employed [4.5, 4.6 and 4.7] in computing non-TEM modes on finitely wide and infinitely long plates. The problem of source radiation in the open parallel-plate waveguide of finite width is considered in reference [4.8]. On the experimental side, we have available the CW measurements in the ALECS facility [4.9] and more extensive field mapping data on the laboratory model simulator [4.10 and 4.11] at Harvard University. In the remainder of this section, we shall briefly review all of the above and then present a method of expressing the measured fields as a superposition of modes and then apply this method to a specific frequency on the laboratory simulator.

IV.2 Infinitely Wide and Infinitely Long Parallel Plates

Figure 4.1 shows an open waveguide made of two parallel plates that are infinitely wide and long when they are separated by a distance $2b$. By starting with the fields in a rectangular waveguide of width $2a$ and

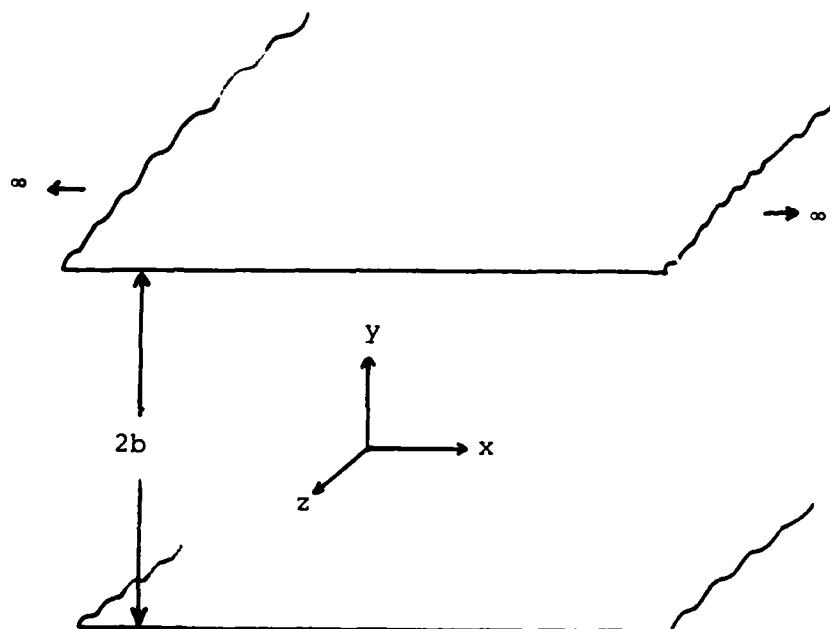


Figure 4.1 Two parallel-plate open waveguide of infinite width (x direction) and infinite length (z direction) with separation = $2b$

height $2b$, and then letting the width go to infinity,
the field components can be written as:

TEM mode

$$E_y(y) = V/b, H_x(y) = I \quad \text{with} \quad E_z = H_z = E_x = H_y = 0 \quad (4.1)$$

TM_{0n} modes

$$\left. \begin{aligned} E_x &= 0 \\ E_{yn}(y, z) &= -V_n(z) \sqrt{\frac{2}{b}} \cos(n\pi y/b) \\ E_{zn}(y, z) &= -j\zeta I_n(z) \frac{n\lambda}{2b} \sqrt{\frac{\epsilon_n}{b}} \sin\left(\frac{n\pi y}{b}\right) \\ H_x(y, z) &= I_n(z) \sqrt{\frac{2}{b}} \cos\left(\frac{n\pi y}{b}\right) \\ H_y &= 0 \\ H_z &= 0 \end{aligned} \right\} \quad (4.2)$$

TE_{0m} modes

$$\left. \begin{aligned} E_x(y, z) &= V_m(z) \sqrt{\frac{2}{b}} \sin\left(\frac{m\pi y}{b}\right) \\ E_y &= 0 \\ E_z &= 0 \\ H_x &= 0 \\ H_y(y, z) &= I_m(z) \sqrt{\frac{2}{b}} \sin\left(\frac{m\pi y}{b}\right) \\ H_z(y, z) &= -j\eta V_m(z) \frac{m\lambda}{2b} \sqrt{\frac{2}{b}} \cos\left(\frac{m\pi y}{b}\right) \end{aligned} \right\} \quad (4.3)$$

where

$V \equiv$ potential of the top plate w.r.t. the central ground plane (i.e., the bottom plate is at $-V$ volts)

$b \equiv$ half separation

$I \equiv$ current flowing in unit width of top plate

$V(z), I(z) \equiv$ voltage and currents along the line satisfying the transmission line equations

$n, m \equiv 1, 2, 3, \dots$ (modal indices)

$\eta \equiv$ free space characteristic admittance

$\zeta \equiv$ free space characteristic impedance

$\lambda \equiv$ free space wavelength

$j \equiv \sqrt{-1}$ with $e^{j\omega t}$ time dependence being implicit.

As an example, we have shown in Figure 4.2 the electric field lines for TEM, TM_{01} , TM_{02} and TM_{03} modes in the region above the ground plane ($y \geq 0$) for a distance of one wavelength on either side of the origin along the propagation direction. It is noted that the modal distributions are invariant in the transverse x -direction. We shall leave the subject of modes on infinitely wide plates at this stage and will have occasion to use them later for representing the measured fields.

IV.3 Finitely Wide and Infinitely Long Parallel Plates

The computation of modes on two parallel plate transmission lines when they are of finite width ($2a$) has been classically treated for the TEM mode and more recently for the non-TEM modes. The TEM mode evaluation uses the standard technique of conformal mapping whereas for

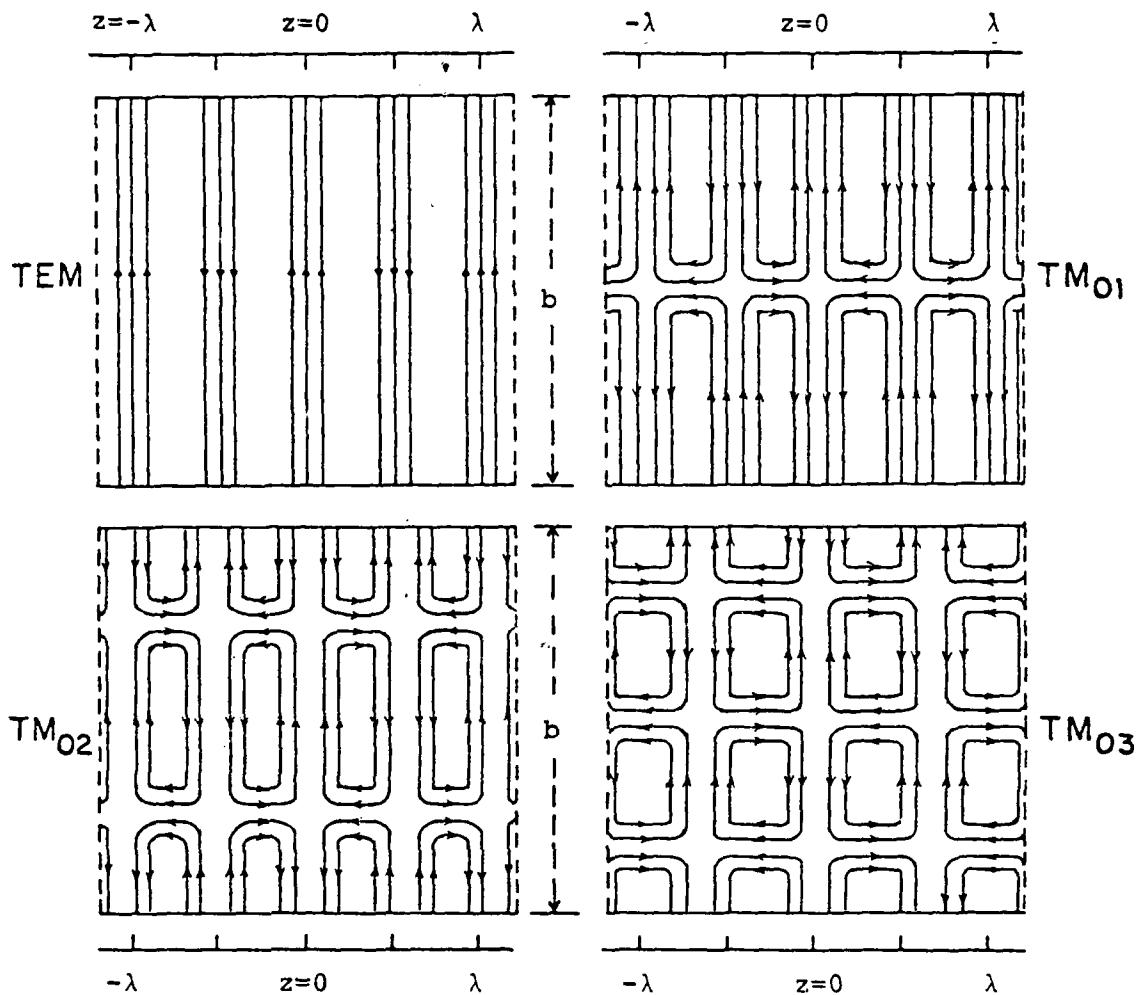


Figure 4.2. Electric field lines for four parallel plate modes (TM and TM_{0n} for $n = 1, 2$, and 3)

determining the non-TEM modes, the approach is to formulate the integral equations for current and charge on the plates. From a knowledge of the current and charge distributions on the plates, the fields are uniquely determined.

a) TEM mode

Figure 4.3 shows the transverse x-y plane of a finitely wide (2a) two-parallel plate transmission line. In this figure, any point in the transverse plane where the TEM quantities (potentials and fields) are desired, is specified by its complex coordinate ($z = x + iy$). This z is a complex coordinate and is not to be confused with the propagation direction coordinate. The available conformal transformation which takes us from the complex coordinate plane to the complex potential plane [4.2, 4.3] was recognized to have a deficiency because it was not an analytic transformation in the complex variable sense. By making suitable variable changes, reference [4.4] gives the slightly modified transformation as

$$\frac{z}{b} = \frac{x + iy}{b} = f(w) = \left[\frac{-2K(m)}{\pi} Z(iw + K(m) + iK(m_1)|m) - i \right] \quad (4.4)$$

where

$K(m) \equiv$ complete elliptic integral of the first kind

$Z(p|m) = E(p|m) - p \frac{E(m)}{K(m)} \equiv$ Jacobi zeta function

$E(m) \equiv$ complete elliptic integral of the second kind

$m_1 = 1 - m$

$m =$ parameter obtained from knowing the geometrical ratio
(a/b)

by solving

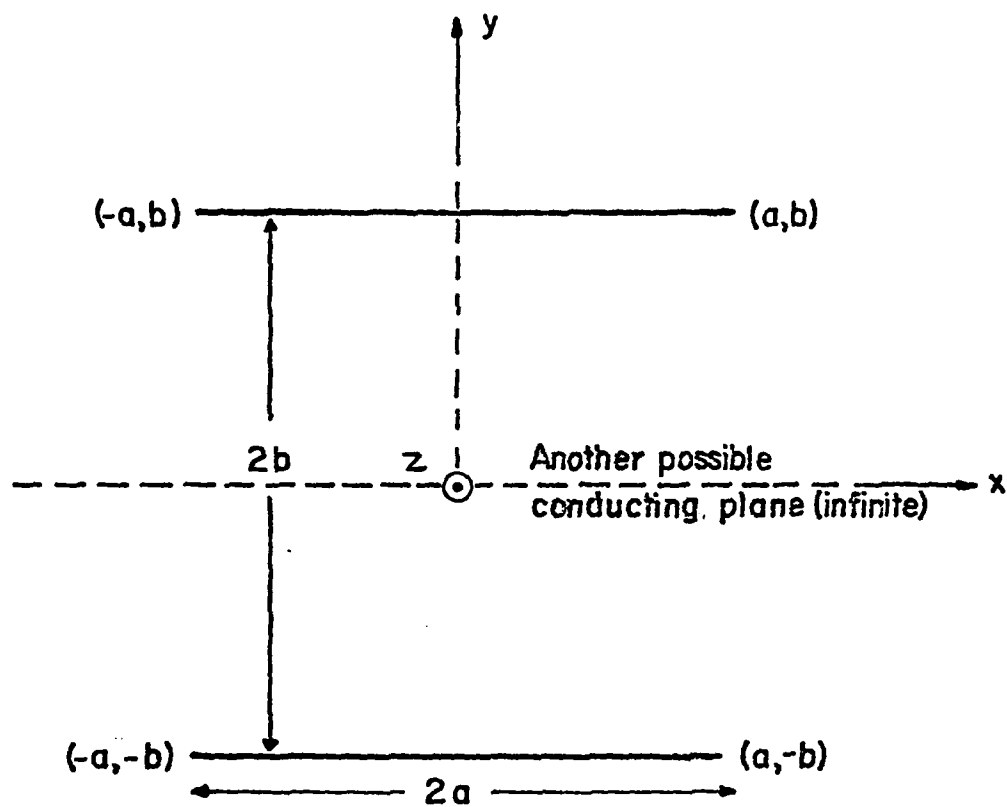


Figure 4.3. Cross section of a symmetrical two-parallel-plate transmission line

$$\frac{a}{b} = \frac{2}{\pi} \left\{ K(m) E(\phi_0|m) - E(m) F(\phi_0|m) \right\} \quad (4.5)$$

with

$$\sin(\phi_0) = \left[\frac{1}{m} \left(1 - \frac{E(m)}{K(m)} \right) \right]^{1/2} \quad (4.6)$$

Note that for a specified point in the transverse plane, the transcendental equation (4.4) needs to be solved for the complex potential, and later the complex field (electric or magnetic) is obtained by computing the gradient of the potential. To facilitate these computations, one recognizes that the entire first quadrant of the complex coordinate z -plane maps into a rectangle of finite dimensions in the complex potential $w = u + iv$ plane. This fact, coupled with the principle of the argument in complex variable theory, helps us to write down the complex potential in a closed integral form

$$w = \frac{1}{2\pi i} \oint w_1 \frac{f'(w_1)}{f(w_1) - (z/b)} dw_1 \quad (4.7)$$

Knowing the potential, the fields are easily determined via algebraic computation of (dw/dz) . An extensive parametric study of the TEM properties in terms of tables and plots was reported [4.4] for dimensions ranging from narrow to wide plates. One example of these calculations is illustrated in Figure 4.4, which shows the contour plots for the transverse electric field components E_x , E_y , the magnitude of the electric field $\sqrt{E_x^2 + E_y^2}$, as well as the magnitude of the differential quantity $|[(E(x,y) - E(0,0))/E(0,0)]|$. This quantity is useful for design purposes where one is concerned with the uniformity of fields near the object location.

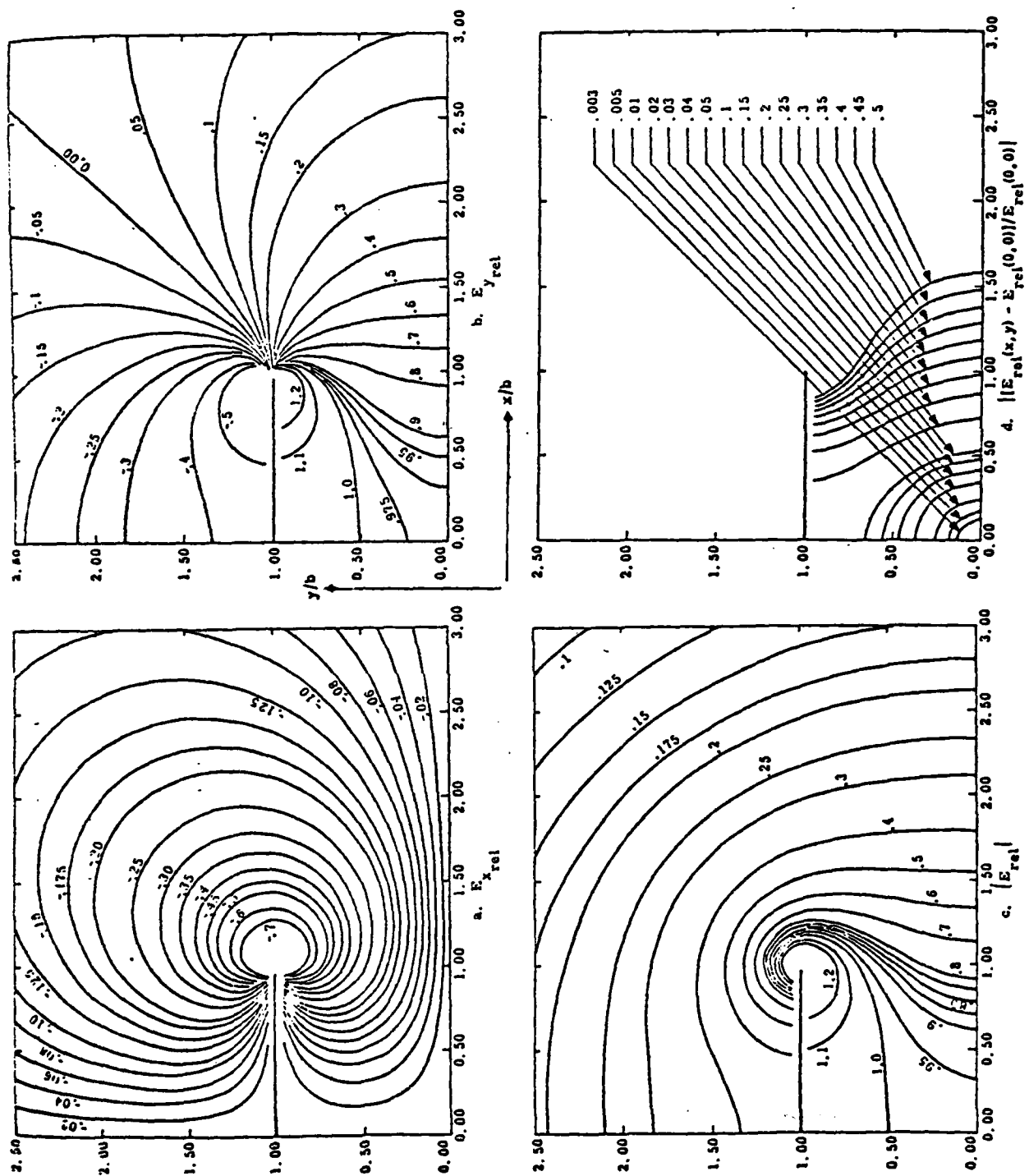


Figure 4.4. TEM quantities for a hypothetical case of $b/a = 1$ (\sim ALECS)

b) Non-TEM Modes

When the cross sectional dimensions of the simulator become comparable to the CW wavelength of operation, it can be expected that non-TEM modes will also propagate in the working volume. In the transient situation, it is desirable to launch fast rising pulses whose rise time is significantly smaller than the transit time across the simulator, resulting in frequency components in the pulse at which non-TEM modes can be supported. As was pointed out earlier, our approach here is to represent the working volume fields as a superposition of parallel-plate transmission line modes and then explore ways of suppressing the undesirable non-TEM modes.

Consider an open waveguide formed by two finitely wide parallel plates as shown in Figure 4.5. Setting incident fields as $\vec{E}^{inc}(\vec{r}, t)$ and $\vec{H}^{inc}(\vec{r}, t)$, the scattered fields $\vec{E}(\vec{r}, t)$ and $\vec{H}(\vec{r}, t)$ are determined by Laplace transform methods,

$$\tilde{\vec{E}}(x, y, \zeta, s) = \int_{-\infty}^{\infty} \int_{-\infty}^{\infty} \vec{E}(\vec{r}, t) e^{-\zeta z} e^{-st} dz dt \quad (4.8)$$

Since there is a translational invariance along the propagating or z direction, it can be Laplace transformed ($z \rightarrow \zeta$) along with the time ($t \rightarrow s$). Also, one can get the transverse components of electric and magnetic fields from the axial components by using

$$\begin{aligned} \tilde{\vec{E}}_t(x, y, \zeta, s) &= (-\zeta/p^2) \nabla_t \tilde{E}_z(x, y, \zeta, s) - (s\mu_0/p^2) \vec{1}_z \times \nabla_t \tilde{H}_z(x, y, \zeta, s) \\ \tilde{\vec{H}}_t(x, y, \zeta, s) &= (-\zeta/p^2) \nabla_t \tilde{H}_z(x, y, \zeta, s) + (s\epsilon_0/p^2) \vec{1}_z \times \nabla_t \tilde{E}_z(x, y, \zeta, s) \end{aligned} \quad (4.9)$$

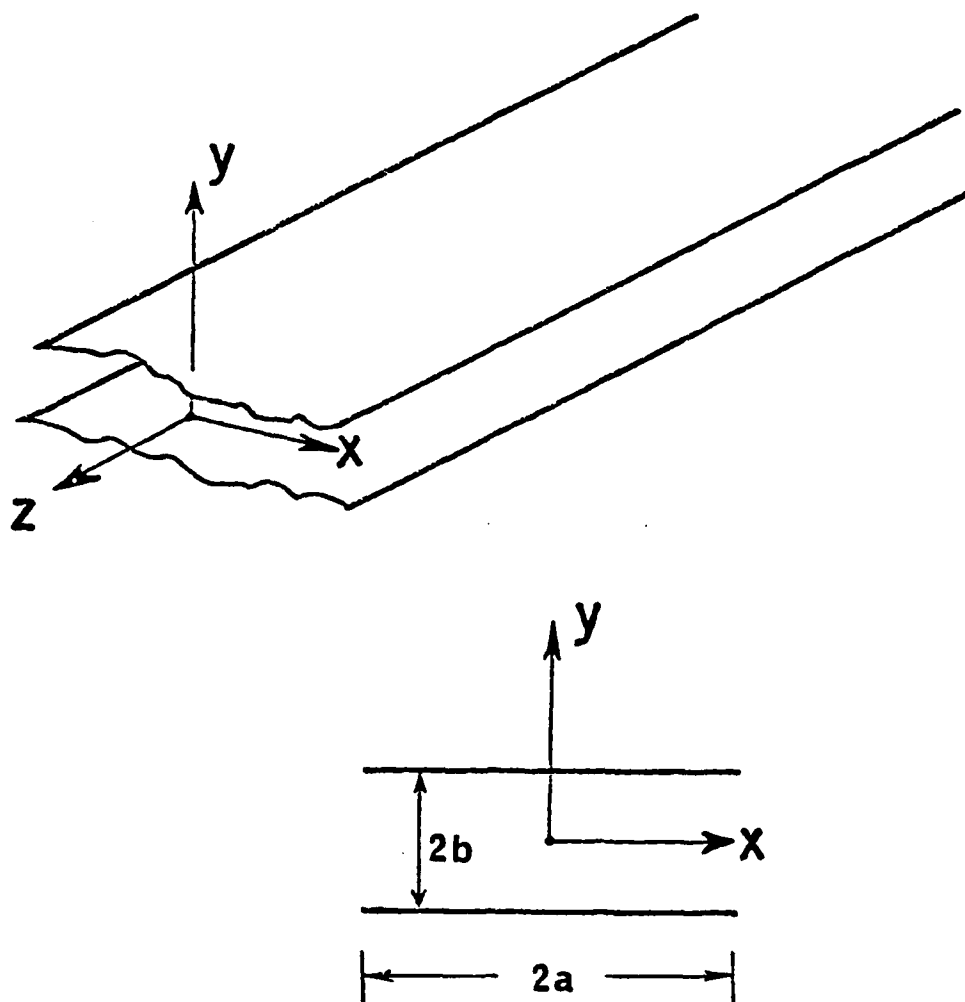


Figure 4.5. Two finitely wide parallel plates

where $p = \sqrt{r^2 - \zeta^2}$ and $\gamma = s/c$ with $c =$ vacuum speed of light.

Marin [4.5], has set up integral equations for the discontinuity $\tilde{g}_{\pm}(x)$ in the tangential magnetic field (equal to induced current) across the top and bottom plate, and the discontinuity $\tilde{f}_{\pm}(x)$ in the normal derivative of the tangential field $(\partial E_z / \partial y)$. Now by requiring the total tangential electric field on the top and bottom plate to vanish, one gets a coupled pair of integral equations for $\tilde{f}_{+}(x)$ and $\tilde{f}_{-}(x)$ as:

$$\begin{aligned} \int_{-a}^a \tilde{F}_{11}(x, x') \tilde{f}_{+}(x') dx' + \int_{-a}^a \tilde{F}_{12}(x, x') \tilde{f}_{-}(x') dx' \\ = -\tilde{E}_z^{\text{inc}}(x, b, \zeta, s) \end{aligned} \quad (4.10)$$

$$\begin{aligned} \int_{-a}^a \tilde{F}_{21}(x, x') \tilde{f}_{+}(x') dx' + \int_{-a}^a \tilde{F}_{22}(x, x') \tilde{f}_{-}(x') dx' \\ = -\tilde{E}_z^{\text{inc}}(x, -b, \zeta, s) \end{aligned}$$

and similarly for $\tilde{g}_{+}(x)$ and $\tilde{g}_{-}(x)$ as:

$$\begin{aligned} \left(\frac{\partial^2}{\partial x^2} - p^2 \right) \left[\int_{-a}^a \tilde{G}_{11}(x, x') \tilde{g}_{+}(x') dx' + \int_{-a}^a \tilde{G}_{12}(x, x') \tilde{g}_{-}(x') dx' \right] = \beta_{+}(x) \\ \left(\frac{\partial^2}{\partial x^2} - p^2 \right) \left[\int_{-a}^a \tilde{G}_{21}(x, x') \tilde{g}_{+}(x') dx' + \int_{-a}^a \tilde{G}_{22}(x, x') \tilde{g}_{-}(x') dx' \right] = \beta_{-}(x) \end{aligned} \quad (4.11)$$

where all of the \tilde{F} and \tilde{G} kernels are known and the forcing functions in equation (4.11) are given by

$$\beta_{\pm}(x) = p^2 \tilde{E}_x^{\text{inc}}(x, \pm b, \zeta, s) + \zeta \frac{\partial \tilde{E}_z^{\text{inc}}}{\partial x}(x, \pm b, \zeta, s) \quad (4.12)$$

In principle, once the integral equations are solved for the unknown functions $\tilde{f}_{\pm}(x)$ and $\tilde{g}_{\pm}(x)$, all of the electric and magnetic field components can be obtained. However, in actual computations, a distinction has been made between narrow (width \ll separation, or $b/a \gg 1$) and wide (width \gg separation, or $b/a \ll 1$) plates. This distinction makes certain approximations to the integral equations possible. References [4.5] and [4.7] deal respectively with narrow ($b/a \gg 1$) and wide plates ($b/a \ll 1$). It is noted that for the narrow plates TE modes are more attenuated as they propagate along the simulator than are the TM modes, whereas for the wide plates TM modes are more attenuated as they propagate along the simulator than are the TE modes. In other words, for the narrow plates TM modes are more important and for the wide plates, TE modes. For a general value of (b/a) , depending on the nature of excitation, one can expect to see both TM and TE modes. The results [4.5 and 4.7] are presented by first computing the p-plane singularities and then the field plots. Since there are two planes of symmetry ($x = 0$ and $y = 0$), the modes are classified into symmetric or anti-symmetric (about $y = 0$ plane) even or odd (about $x = 0$ plane) modes. Transcendental equations for obtaining the p-plane singularities have been derived in these references and they are summarized below.

Narrow plates (b/a >> 1)

Mode type	transcendental p equation
even TM	$\ln(4/pa) - \gamma + K_0(2pb) = 0$
odd TM	$\ln(4/pa) - \gamma - K_0(2pb) = 0$
TE modes	not supported when $ pa \ll 1$

Wide plates (b/a << 1)

Mode type	transcendental p equation
even sym. TM	$16\sqrt{\pi} (pa)^{3/2} \exp(2pa) - 1 = 0$
odd sym. TM	$16\sqrt{\pi} (pa)^{3/2} \exp(2pa) + 1 = 0$
even antisym. TM	$8 \sqrt{\frac{\pi pa^3}{b^2}} \exp\{2pa + (2pb/\pi) [\ln(2\pi/pb) - \gamma + 1]\} - 1 = 0$
odd antisym. TM	$8 \sqrt{\frac{\pi pa^3}{b^2}} \exp\{2pa + (2pb/\pi) [\ln(2\pi/pb) - \gamma + 1]\} + 1 = 0$
even sym. TE	$2\sqrt{\pi} \sqrt{pa} \exp(2pa) + 1 = 0$
odd sym. TE	$2\sqrt{\pi} \sqrt{pa} \exp(2pa) - 1 = 0$
* even antisym. TE	$1 - \exp\{2pa + (2pb/\pi) [\ln(2\pi/pb) - \gamma + 1]\} - b\sqrt{\frac{p}{a\pi}} = 0$
* odd antisym. TE	$1 + \exp\{2pa + (2pb/\pi) [\ln(2\pi/pb) - \gamma + 1]\} - b\sqrt{\frac{p}{a\pi}} = 0$

*least attenuated

The p-plane singularities, which are poles in p-plane, each corresponding to a branch point in the usual s-plane, can be denoted by $p_{m,n}^{(\pm, \pm, E \text{ or } H)}$, where m and n are the modal indices corresponding to the number of half cycle variations in x and y directions. In the superscript, the two \pm denote respectively the symmetry or antisymmetry with respect to $x = 0$ or $y = 0$ planes, while E (TM modes) and H (TE modes) indicate the modes. This notation can uniquely identify a mode type. In the next few pages, we have reproduced from the two references [4.5 and 4.7] examples of p-plane singularity plots and typical field distribution plots.

Figures 4.6 to 4.8 are for the case of narrow plates. In Figure 4.6 the p-plane singularity plots for the odd and even TM modes are shown. It is seen from Figure 4.6 that the p-plane singularities are like the natural frequencies (s_α) in the complex frequency (s) plane in the SEM representation. It is however emphasized that each pole in the p-plane corresponds to a branch point in the s-plane. In Figures 4.7 and 4.8, the magnitude of the principal electric field component $|E_y|$ is plotted for the TEM and three lowest antisymmetric TM modes, as functions of normalized y (i.e., y/b) and normalized x (i.e., x/a) coordinates. It is seen from Figure 4.8 that the amplitude of the principal electric field grows unbounded as one moves away in the transverse x -direction. This is to be expected for leaky mode description.

Figures 4.9 to 4.12 illustrate the example of wide plates. Figures 4.9 and 4.10, respectively, show the transverse propagation constants for the antisymmetric TE (odd and even) and the symmetric TE and TM modes. The transverse variation (along the x direction) of the principal electric (E_y) and magnetic (H_x) field components

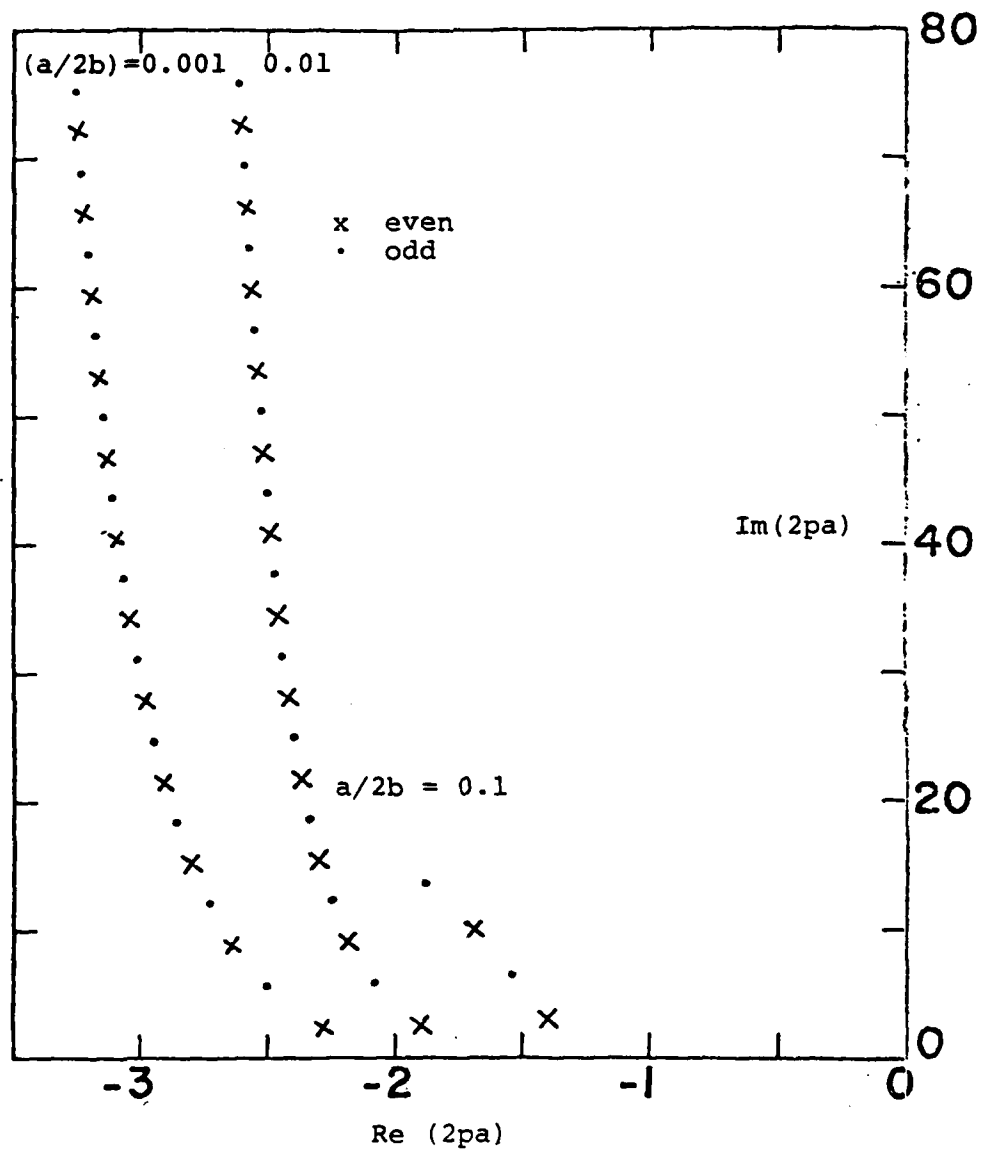


Figure 4.6. Transverse propagation numbers for odd and even TM modes

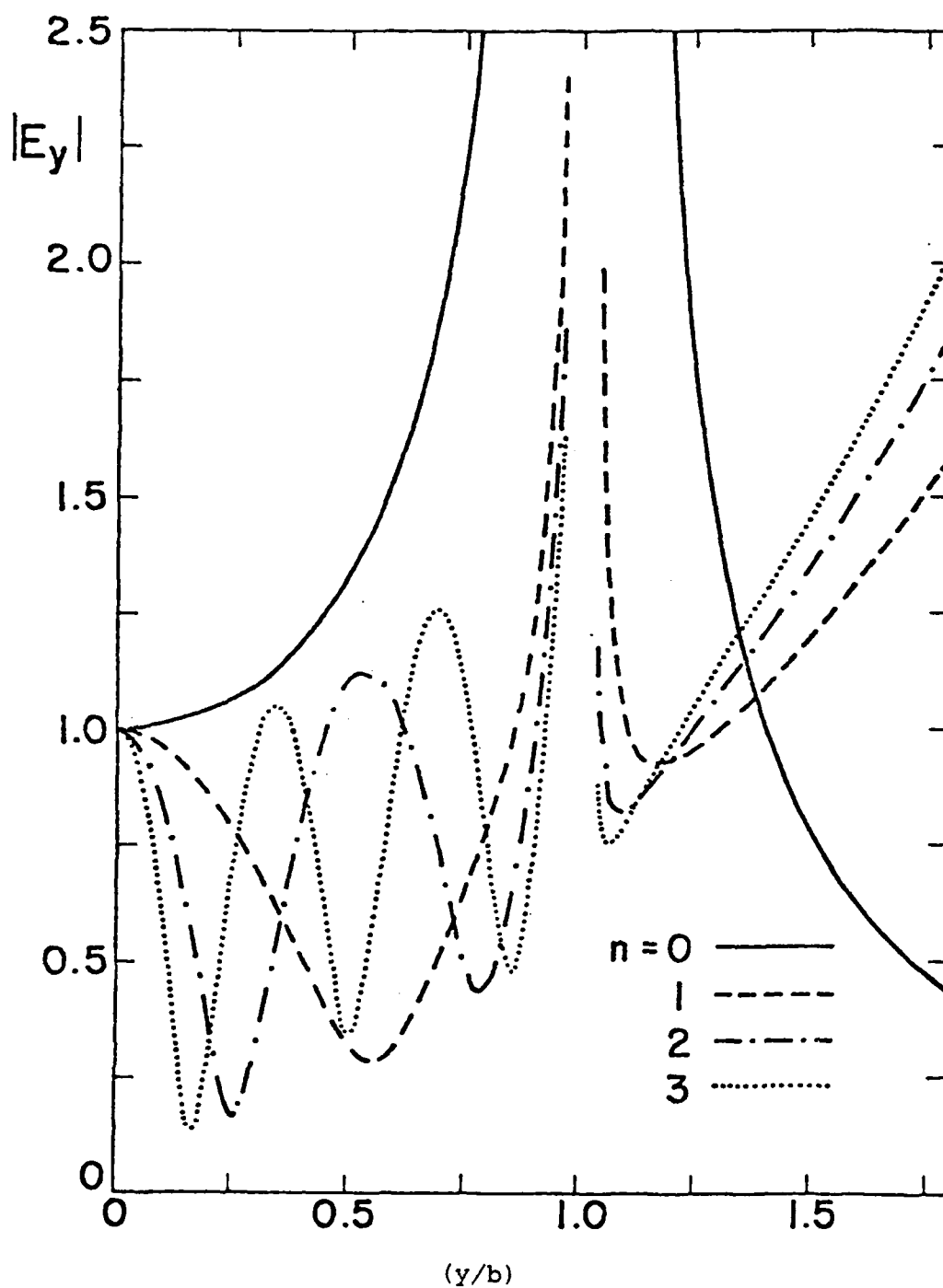


Figure 4.7. The variation along the y -axis of the magnitude of E_y for TEM ($n = 0$) and three lowest antisymmetric TM_{0n} modes

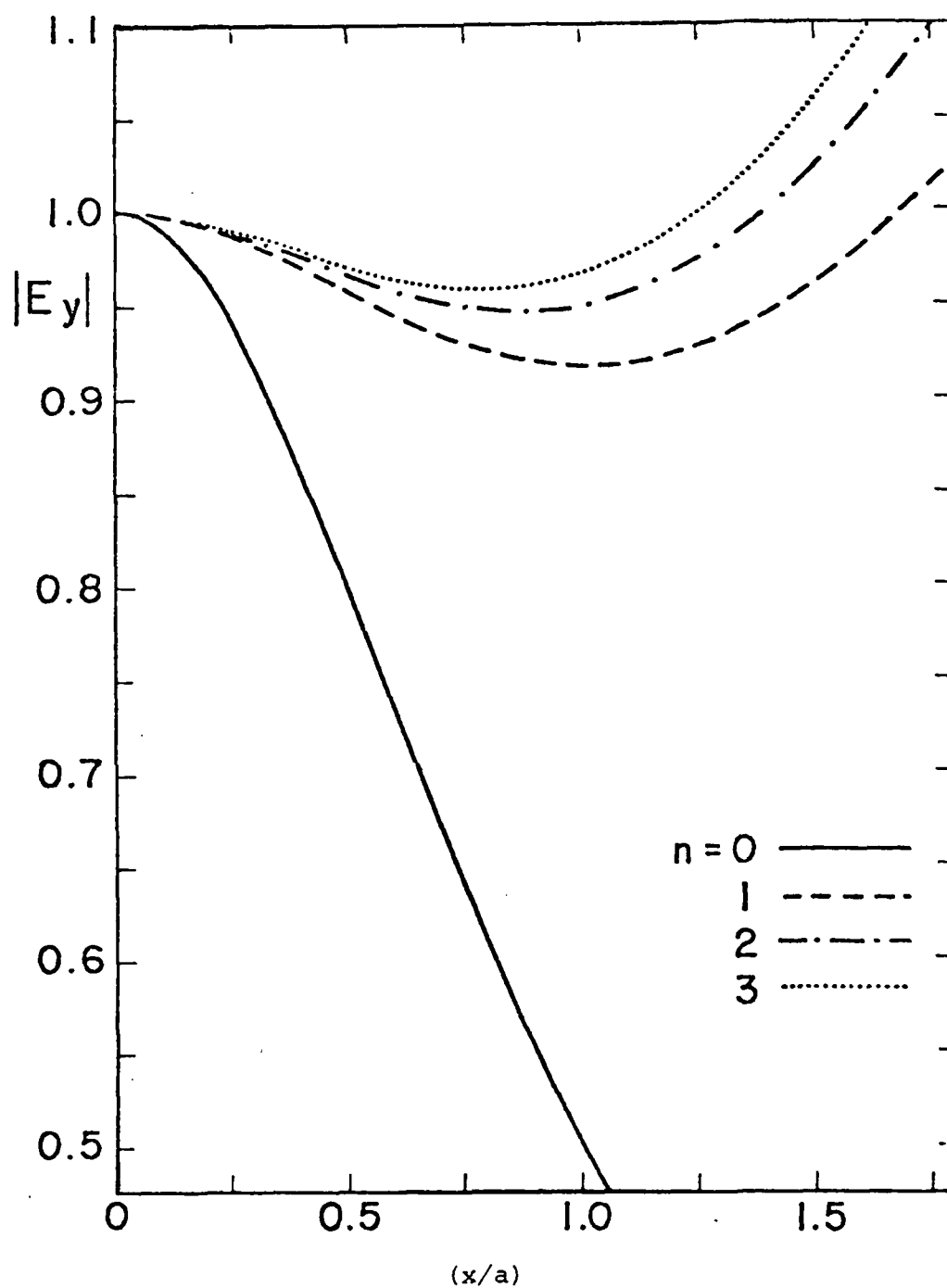


Figure 4.8. The variation along the x-axis of the magnitude of E_y for the TEM mode ($n = 0$) and three lowest antisymmetric TM modes

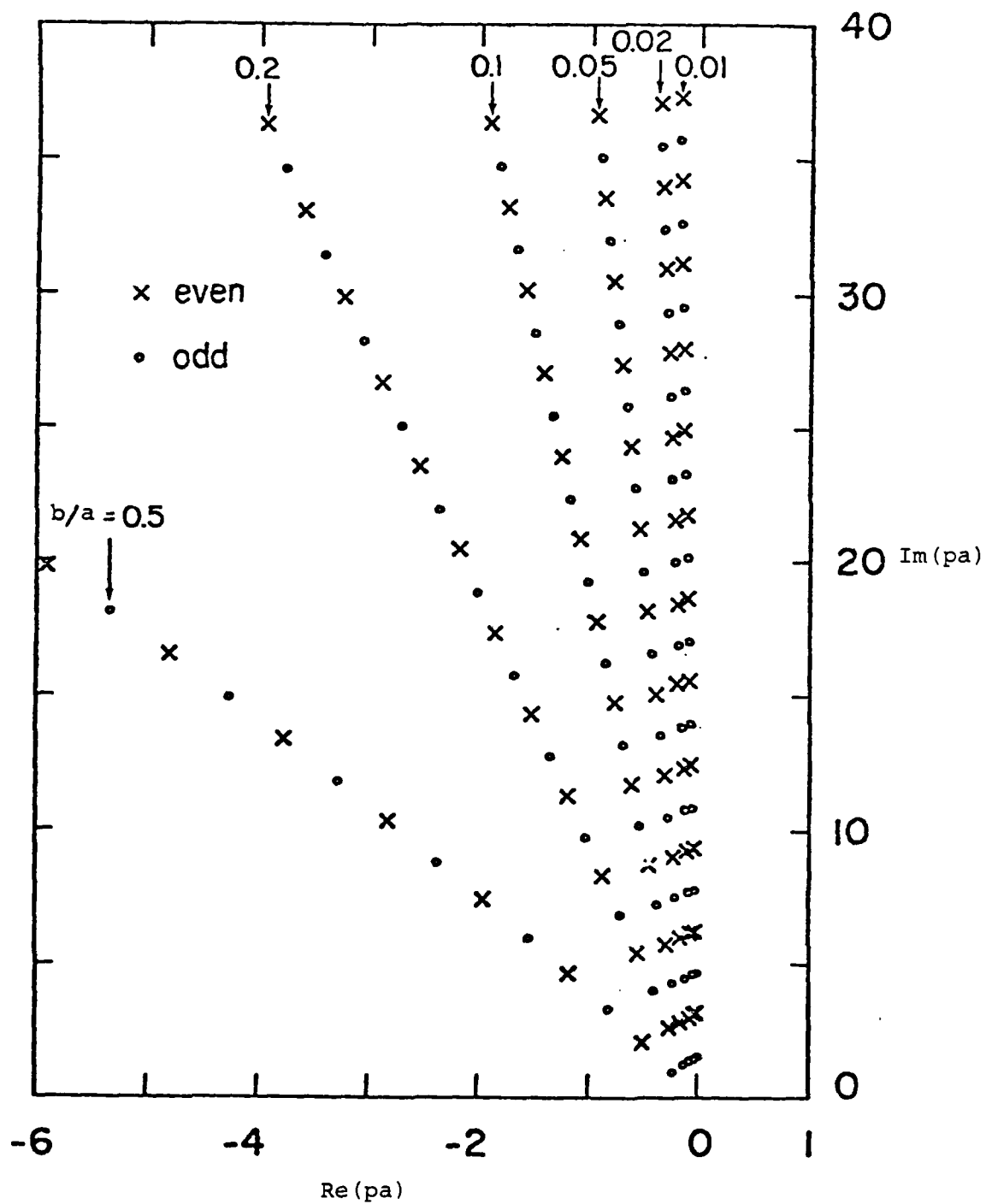


Figure 4.9. The p-plane singularities for the antisymmetric TE modes on wide plates

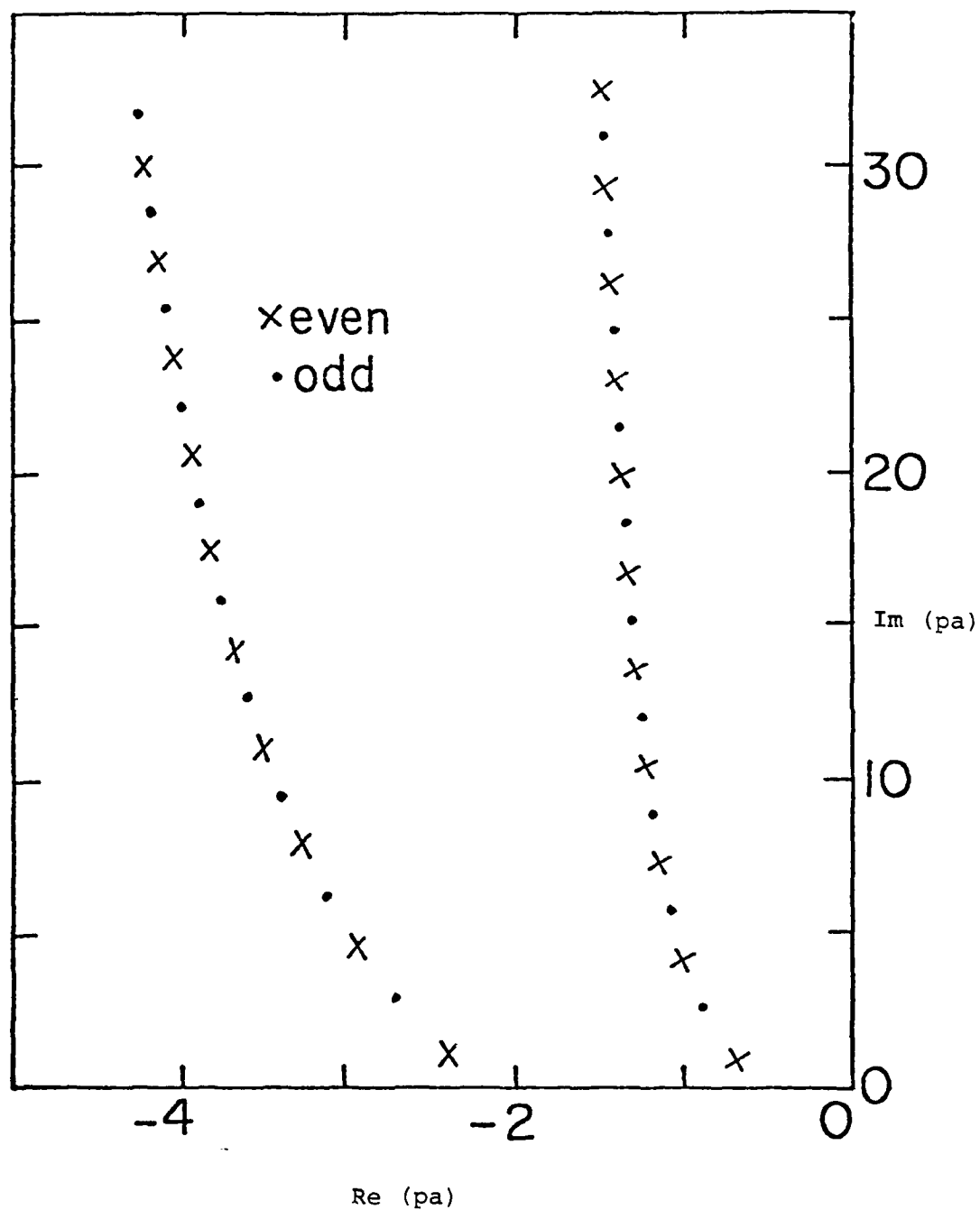


Figure 4.10. The p-plane singularities for the symmetric TE modes (1st layer) and the symmetric TM modes (2nd layer) as (b/a) tends to zero

for the four lowest odd antisymmetric TE modes are also shown respectively in Figures 4.11 and 4.12.

The general unrestricted case, when the plates are neither wide nor narrow, has recently received much attention from Dikewood Industries under the present effort; extensive field plots reported by them are not reproduced here.

Thus, extensive computations of the transverse wave numbers and field plots are available in the literature for both the special cases of narrow and wide plates as well as the unrestricted case.

IV.4 Source Excitation

It is well known that the fields in the working volume can be represented by

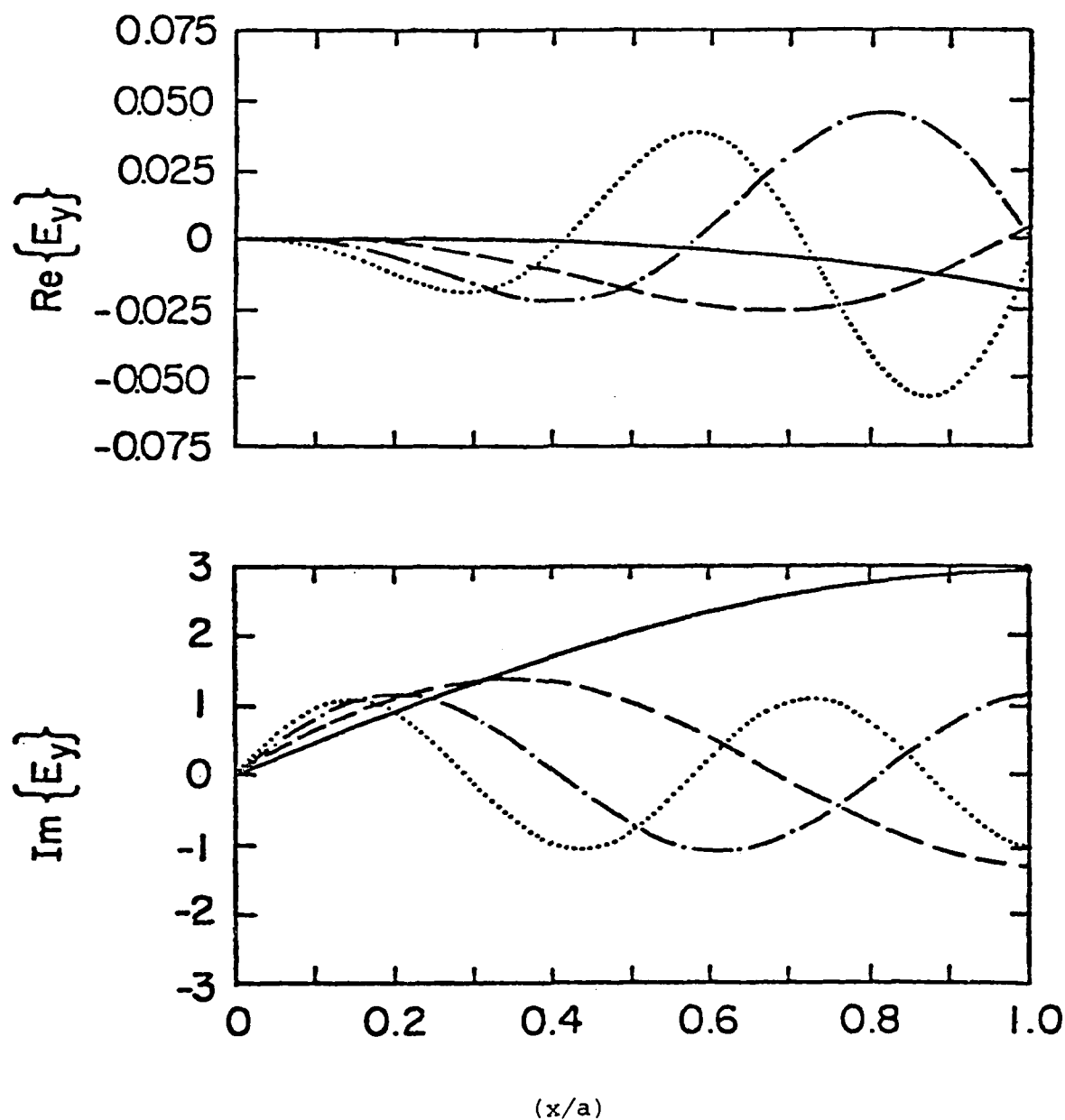
$$\tilde{E}(\vec{r}, s) = \tilde{E}_1(\vec{r}, s) + \tilde{E}_2(\vec{r}, s) \quad (4.13)$$

where

$$\tilde{E}_1(\vec{r}, s) \equiv \text{discrete spectra} = \sum_n \tilde{A}_n(x, y) e^{-\gamma_n z} \quad (4.14)$$

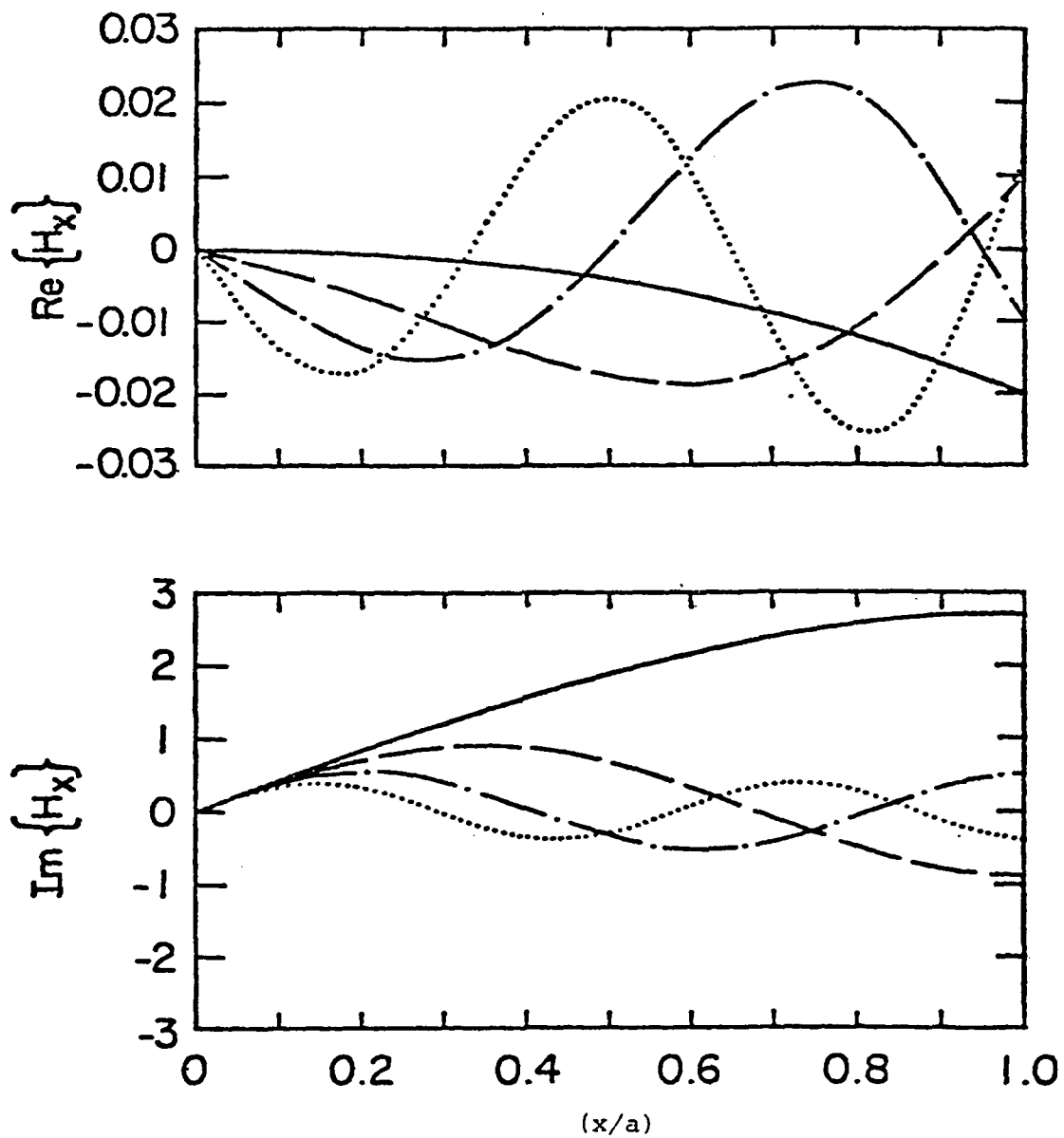
$$\tilde{E}_2(\vec{r}, s) \equiv \text{continuous spectra} = \iiint \tilde{B}(\alpha, \beta) e^{-(\gamma_1 x + \gamma_2 y + \gamma_3 z)} d\alpha d\beta \quad (4.15)$$

The contribution from the continuous spectrum is perhaps negligible for certain geometries and source configuration, but in general it is important to know their relative contributions. With this goal in mind, [4.8] computes the



$\rho_a = -0.010 - i1.54$ _____, $-0.028 - i4.62$ -----
 $-0.045 - i7.71$ -.-.-.-.-, $-0.062 - i10.81$

Figure 4.11. Variation of E_y along normalized x direction for the four lowest odd anti-symmetric TE modes



$\text{pa} = -0.010 - i1.54$ _____, $-0.028 - i4.62$ -----
 $-0.045 - i7.71$ _____, $-0.062 - i10.81$

Figure 4.12. Variation of H_x along normalized x direction for the four lowest odd anti-symmetric TE modes

total electric field $\vec{E}_T(\vec{r}, s)$ for a specific geometry with a prescribed source configuration. It employs the moment method which is suitable for a guide with small to moderate cross sections. The source consists of a y-direction oriented current $\vec{J}^{inc}(\vec{r}) = \hat{1}_y J^{inc}(x, y) e^{-j\beta z}$. The variation in the x-direction is assumed to be a Dirac delta function while in the y-direction, the source is sinusoidal. It propagates in the z-direction according as $e^{-j\beta z}$. With such a prescribed source, the total field has been computed to assess the relative contributions of discrete and continuous spectra. However, the computations are not complete, since one is required to perform a spectral integration with respect to the variable β to obtain a complete field excitation solution. We conclude that, although the formulation is available, much more work needs to be done before meaningful conclusions can be drawn concerning the contribution of the continuous spectrum.

IV.5 Experimental Results

Two readily available sources for the experimental data in bounded wave simulators are the ALECS CW measurement reports [4.9] and more recently from the laboratory model measurements [4.10 and 4.11], in addition to the time domain data report [4.12] in the early years of ALECS facility development.

In the time domain, [4.12] has shown that at early times, the fields in the working volume (for approximate step function source) are well described by $(1/r)$ variation of the spherical wave from the conical launcher and followed by: a) edge diffraction and b) specular reflections off the top plate. In the late times,

quasi-static TEM fields are obtained. In the high frequency (early time) range, experimentally about $\pm 15\%$ ripple has been observed in ALECS fields at midheight in the working volume and about $\pm 35\%$ ripple has been observed near the ground plane.

From the experimental results reported in reference [4.9], one can, in addition, draw the following conclusions.

a) Input impedance

The TDR data indicates that the input impedance of the ALECS facility is fairly constant at $\sim 90\Omega$. This is consistent with the principal TEM mode being dominant at the simulator ends where the non-TEM modes cannot be supported. The impedance data [4.9] have also been presented on Smith charts for various experimental configurations.

b) Ripples in measured fields

The measured electric and magnetic fields display significant ripples at all locations, with the largest effects appearing near the ground plane at high frequencies.

c) Notch at 25 MHz

The swept CW measurements also show a deep notch in the measured magnetic field (H_x) at the center at nearly 25 MHz. This has also been experimentally confirmed on the laboratory model simulator at Harvard. The notches in ALECS and the model simulator are quite similar in terms of notch frequency, location, depth and width.

At the notch frequency, the fields can be represented by a superposition of TEM and TM_{0n} modes and the notch itself is due to TEM and TM_{0n} standing waves. Work is in progress to improve the termination for minimizing TEM reflections. In addition, mode suppression

techniques are also being attempted to selectively load or damp the non-TEM modes. A detailed account of the experimental results on the laboratory model bounded wave simulator appears in Section VI.

IV.6 Modal Representation of Measured Fields

In the experimental field maps performed at $f_1 = 626.5$ MHz and $f_2 = 264$ MHz on the laboratory model simulator, it was observed that the measured fields were fairly uniform in the transverse x-direction except near the edges. The frequencies f_1 and f_2 correspond roughly to 60 MHz and 25 MHz in ALECS. At these two frequencies, the laboratory model has b/a ratios of 1.23 and 0.83. The characteristic principal TEM mode impedances Z_C^{TEM} are respectively 100Ω and 80Ω . These values are summarized below:

- 1) Lab. model frequency of operation = $f_1 = 626.5$ MHz
 (corresponding ALECS frequency ≈ 60 MHz)
 half separation $\equiv b = 1.08$ m
 half width $\equiv a = 0.875$ m
 $(b/a) = 1.23$
 $Z_C^{TEM} \approx 100\Omega$

- 2) Lab. model frequency of operation = $f_2 = 264$ MHz
 (corresponding ALECS frequency ≈ 25 MHz)
 half separation $\equiv b = 0.75$ m
 half width $\equiv a = 0.875$ m
 $(b/a) = 0.83$
 $Z_C^{TEM} \approx 80\Omega$

Extensive field plots are available elsewhere in this report, but the objective here is to represent the fields in terms of superposition of modes. At the higher frequency f_1 , Figure 4.13 demonstrates that the transverse variation is minimal away from the edges. For this reason, at least for the present purposes, we may use the parallel plate modes of infinitely wide plates [4.1] in the superposition process. It is seen that at f_1 , $\lambda_1 = 48$ cm, four modes, i.e., TEM, TM_{01} , TM_{02} and TM_{03} , are well above the cut off. They have respectively guide wave numbers of

$$\left. \begin{aligned} k_{g0} &= k = (2\pi/\lambda_1) = 0.1309 \text{ cm}^{-1} \\ k_{g1} &= 0.977k = 0.128 \text{ cm}^{-1} \\ k_{g2} &= 0.893k = 0.117 \text{ cm}^{-1} \\ k_{g3} &= 0.748k = 0.098 \text{ cm}^{-1} \end{aligned} \right\} \quad (4.16)$$

The corresponding guide wavelengths are

$$\left. \begin{aligned} \lambda_{g0} &= \lambda_1 = 48 \text{ cm} \\ \lambda_{g1} &= 49.1 \text{ cm} \\ \lambda_{g2} &= 53.7 \text{ cm} \\ \lambda_{g3} &= 64.2 \text{ cm} \end{aligned} \right\} \quad (4.17)$$

At each cross section ($z = \text{constant}$), the principal electric field E_y is a superposition of the four modes in varying amplitudes. That is

$$\begin{aligned} E_y(z) &= A(z) + B(z) \cos(\pi y/b) + C(z) \cos(2\pi y/b) \\ &\quad + D(z) \cos(3\pi y/b) \end{aligned} \quad (4.18)$$

where $A(z)$, $B(z)$, $C(z)$ and $D(z)$ are complex [e.g.,

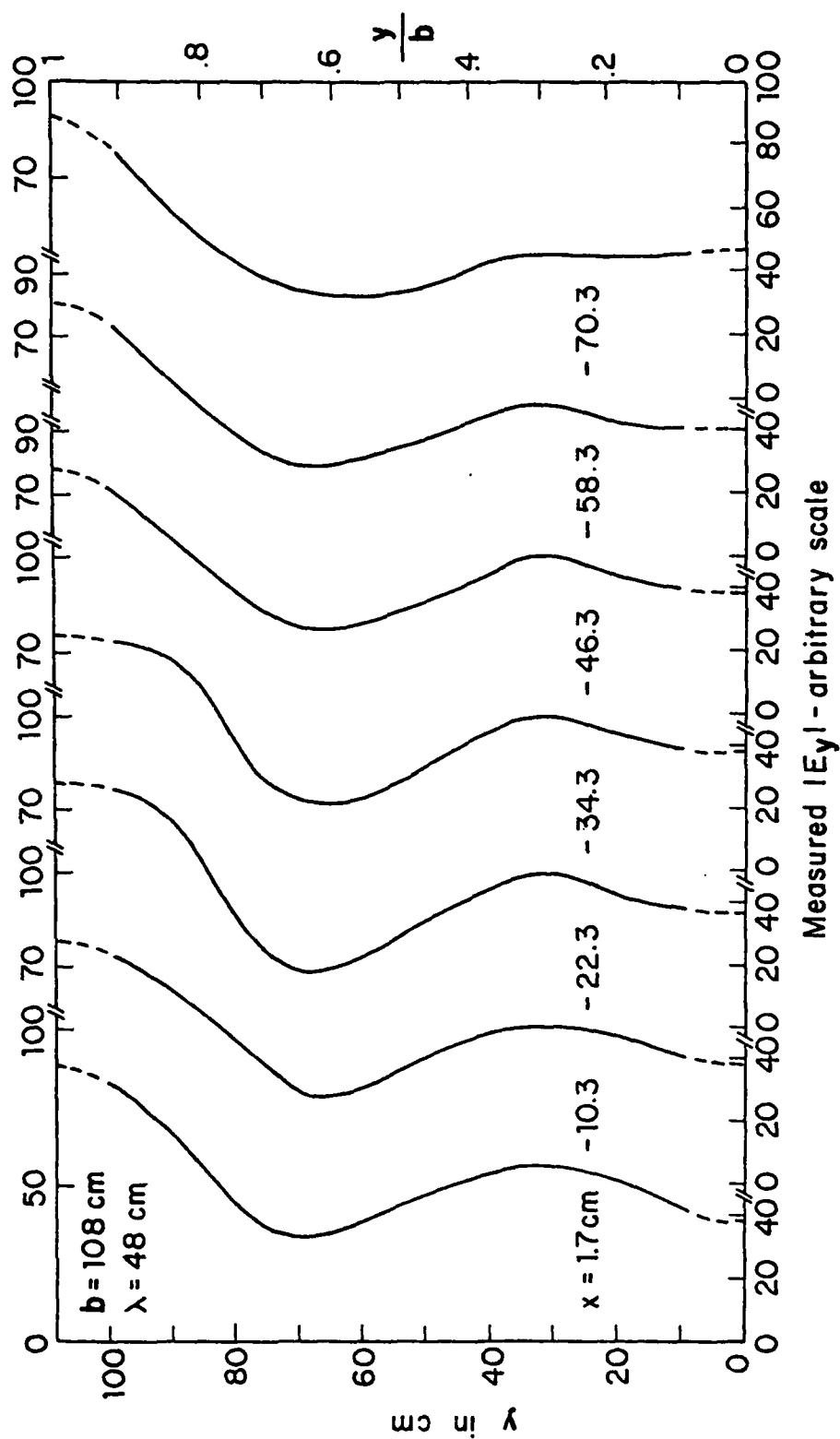


Figure 4.13. Measured electric field near central plane ($z = 0$) in parallel-plate region

$A(z) = A_R(z) + i A_I(z)$ amplitude coefficients. They are determined by fitting the measured distribution with the distribution of equation (4.18). Since transverse x does not play a significant role, the fitting is done at $x = 0$ with the origin ($x = 0, y = 0, z = 0$) taken as the phase reference. The coefficients are shown plotted in Figure 4.14. With known complex amplitudes of TEM and the TM_{0n} modes, the electric field $E_y(y, z)$ can be computed as a function of y at any desired cross section using equation (4.18). Figures 4.15a and 4.15b use broken lines to show the calculated vertical distributions of the real and imaginary parts of E_y at the various locations and solid lines for the measured distributions. From these two figures, it is evident that the fields in the work volume at this frequency, f_1 , are well represented by a superposition of TEM and three TM_{0n} modes.

A similar superposition representation has also been carried out at the lower frequency, $f_2 (= 264 \text{ MHz})$, and it was observed that the working volume fields at f_2 can be represented as a superposition of TEM and TM_{01} modes only. For the sake of simplicity, this analysis is not presented here.

We conclude that if sufficiently detailed field mapping is carried out at single CW frequencies, the measured working volume fields can always be represented as a sum of the principal TEM and a few non-TEM modes. From the experimental findings at Harvard on the laboratory model simulator, it is satisfactory to use the modes on infinitely wide plates. Of course, if more accuracy is desired, (it may well be for certain other geometries or frequencies) the mode calculations on finitely wide plates can also be used in the representation of measured fields as a superposition of modes.

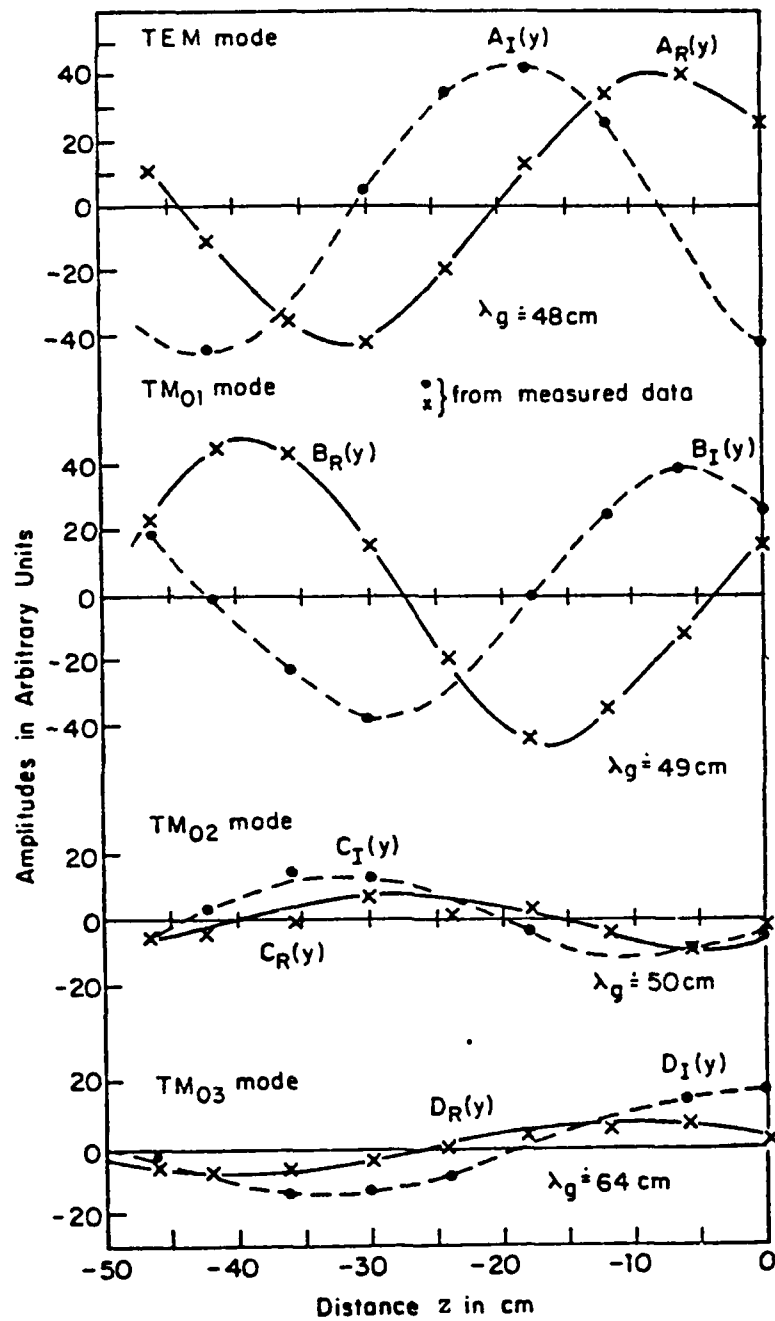


Figure 4.14. Complex amplitudes of TEM, TM₀₁, TM₀₂, and TM₀₃ modes at f_1

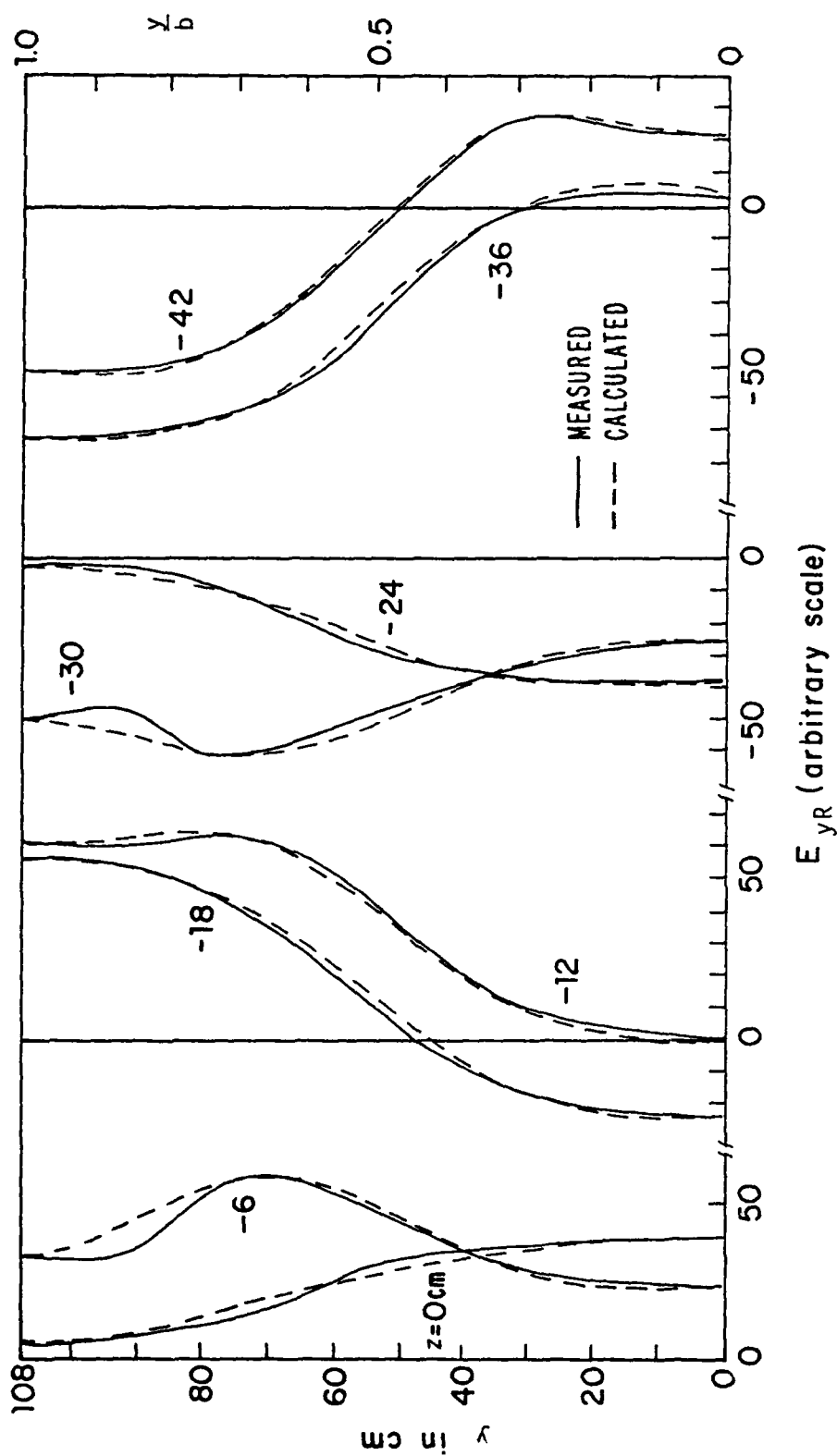


Figure 4.15a. Real part of vertical electric field in working volume. (Phase reference: $x = y = z = 0$)

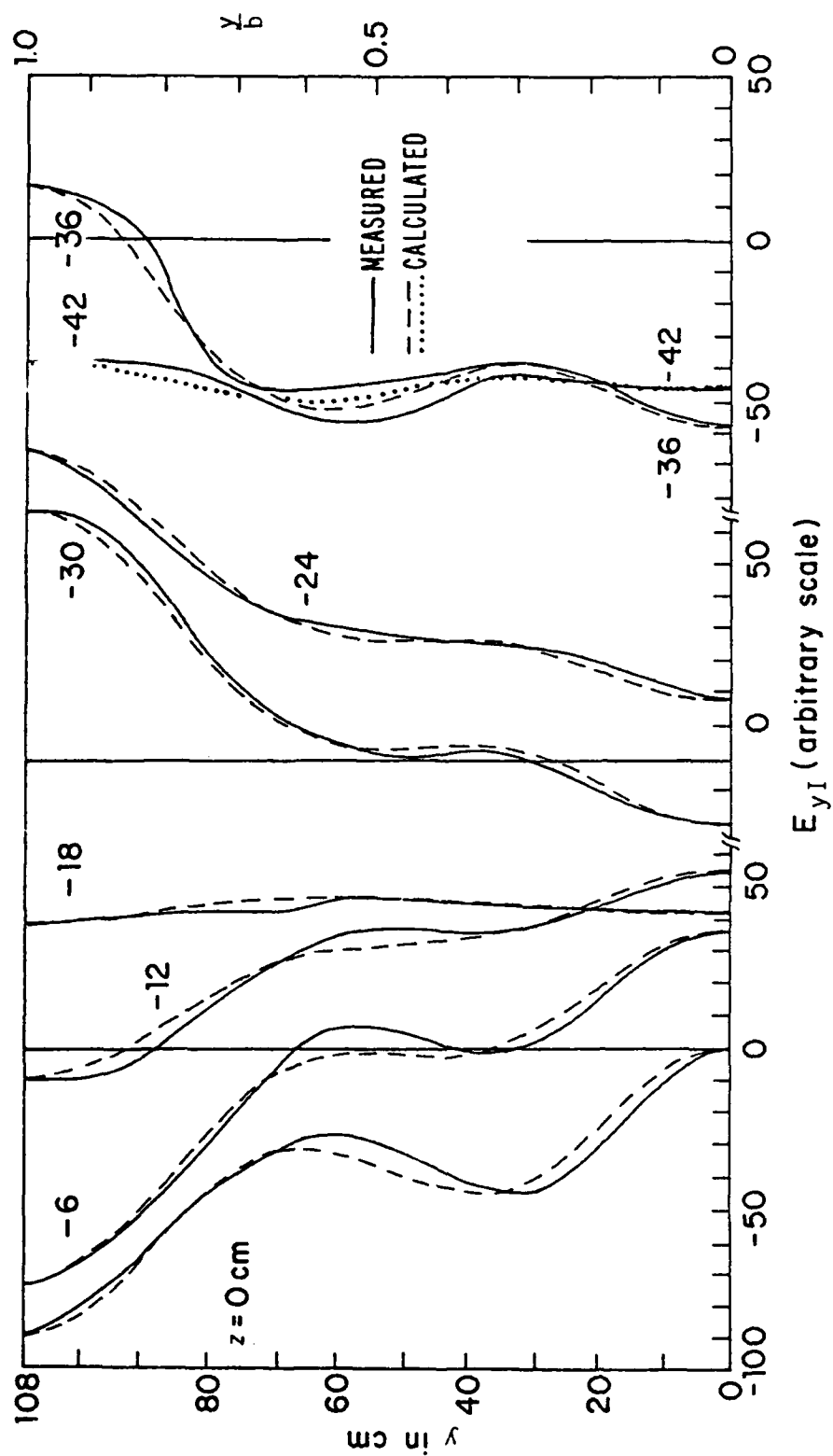


Figure 4.15b. Imaginary part of vertical electric field in working volume. (Phase reference: $x = y = z = 0$)

It is rewarding for those of us concerned with this technology to realize that we are now in a better position to understand and interpret the measured fields. Such interpretations go a long way in enhancing our ability to suggest modifications in the simulator design and construction for improved simulation fidelity.

V TERMINATIONS FOR THE SIMULATORS

V.1 Introduction

In the preceding sections, the parallel-plate simulator structure is considered, starting from the source end (pulser, wave launcher) through the working volume (parallel-plate region). In this section, we consider the problem of effectively terminating the wave after its incidence on the test object in the working volume.

If the parallel-plate transmission line ends abruptly just beyond the working volume, the wave traveling along the transmission line is reflected back to the working volume and interacts with the test object before the object response is complete. Building a long transmission line to delay reflections from interacting with the object while it is still responding to the incident wave necessitates a costly structure and is not practical. In fact, for an aircraft under test, the clear time for the reflected wave is of the order of microseconds and the transmission line must extend at least a few hundred meters past the working volume, if an efficient terminator is absent.

The technique most commonly used in reducing reflections is to terminate the transmission line in an impedance nearly equal to the characteristic impedance of the parallel-plate structure. For a proper termination, it is necessary to consider many aspects of the design, such as (1) whether to have the termination perpendicular to the transmission line or at an angle, (2) the values of the terminating elements, (3) the distribution of the terminating elements, and (4) the practical aspects of the design. These and other features of terminators are considered in this section.

V.2 Values of the Terminating Elements

At sufficiently low frequencies where the transmission-line cross-section dimensions are small compared with the wavelength, it is well known from transmission-line theory that a terminating impedance of value equal to the characteristic impedance of the line terminates the line perfectly. Under this situation, the reflection coefficient ρ as defined below, is identically zero.

$$\rho = \frac{Z_L - Z_C}{Z_L + Z_C} \quad (5.1)$$

where Z_L is the terminating impedance and Z_C is the characteristic impedance of the line.

The condition $Z_L = Z_C$ is reasonably accurate at low frequencies where the terminating impedance can be considered as being distributed uniformly at the terminating plane which is perpendicular to the direction of propagation of the incident wave. This is the same as considering a lumped terminating element. At higher frequencies, this is no longer true and one has to consider the distributed nature of the termination as well as the effect of the free space medium just outside the termination. Indeed, if the cross-sectional dimensions are no longer small compared with wavelengths, one has to take into account the effect of free space (outside the terminator) on the termination. In fact, the impedance seen by the incident wave consists of the parallel combination of the terminating impedance Z_L and the free-space impedance Z_0 . We thus have a problem to contend with: at low frequencies, the incident wave sees an impedance Z_L ; at high frequencies, it sees $Z_L || Z_0$; and at intermediate frequencies, the impedance is between the above two values.

To design for an efficient match, it is clear that Z_L must be frequency dependent so that the incident wave is

always matched, i.e., the combined impedance at the end is equal to the wave impedance inside the simulator. Baum [5.1] first suggested the form of the terminating impedance to be the series combination of a resistance R and an inductance L , i.e.,

$$\tilde{Z}_L(s) = R + sL \quad (5.2)$$

where s denotes the complex frequency. For low frequencies, i.e., $s \rightarrow 0$, the wave sees only the real part of Z_L and behaves as $Z_L \simeq R$. The transmission line is matched by making $R = Z_C$. At high frequencies, the plate separation is large compared to the wavelength and the electric and magnetic fields of the incident wave are related by Z_0 . At these frequencies, i.e., $s \rightarrow \infty$, $Z_L \rightarrow \infty$ and the parallel combination of Z_L and Z_0 remains to be Z_0 and the incident wave is again matched.

In between these two frequency extremes the wave reflection is very complicated. The lumped element representations of the termination no longer works satisfactorily. Instead, one needs to use distributed analysis. However, let us study the reflection characteristics of a step incident wave to gain some qualitative insights. For frequencies low enough so that the wave sees mainly Z_L , the reflection is given by equation (5.1), i.e.,

$$\frac{\tilde{V}^r(s)}{\tilde{V}^{inc}(s)} = \frac{\tilde{Z}_L(s) - Z_C}{\tilde{Z}_L(s) + Z_C} \quad (5.3)$$

For a unit step incident voltage, i.e.,

$$\tilde{V}^{inc}(s) = V_0/s \quad (5.4)$$

and with $\tilde{Z}_L(s)$ as given by (5.2), we have

$$\frac{v^r(t)}{V_0} = \left\{ \frac{R - Z_C}{R + Z_C} + \frac{2Z_C}{R + Z_C} \exp\left(-\frac{R + Z_C}{L} t\right) \right\} u(t) \quad (5.5)$$

The total voltage as given by

$$\frac{v^{\text{total}}(t)}{V_0} = u(t) + [V^r(t)/V_0]$$

is plotted in Figure 5.1.

V.3 Idealized Analyses

From discussions in the preceding subsection, it is clear that at intermediate frequency range, the termination needs to be treated as a distributed element to understand the wave-terminator interaction.

The underlying principal was first discussed by Baum [5.1] who suggested the use of an admittance sheet containing resistive and inductive quantities. Latham and Lee [5.2] solved the idealized problem using the extended Wiener-Hopf technique. Baum [5.3] has further extended the terminating concept to a sloped admittance sheet plus coplanar conducting flanges. Performance evaluations are done by Varvatsis and Sancer for both the perpendicular case [5.4] and the sloped case [5.5]. These geometries are illustrated in Figure 5.2.

In all these analyses, the authors idealize the problems to be two-dimensional, i.e., assuming that there is no variation in the transverse direction of the parallel-plate. Furthermore, the electric field is assumed to be constant at the infinitesimally thin admittance sheet. Under these idealized assumptions, Latham and Lee [5.2] draw the following conclusions for the perpendicular case.

(1) For the admittance sheet to have a positive real part, the plate separation h must be less than $1/3$ of the wavelength. (This implies that for a perfect match, reactive termination is necessary.)

(2) In the two-dimensional case, for a good match, at time $> h/2c$, the resistive part is given by

$$R = Z_0$$

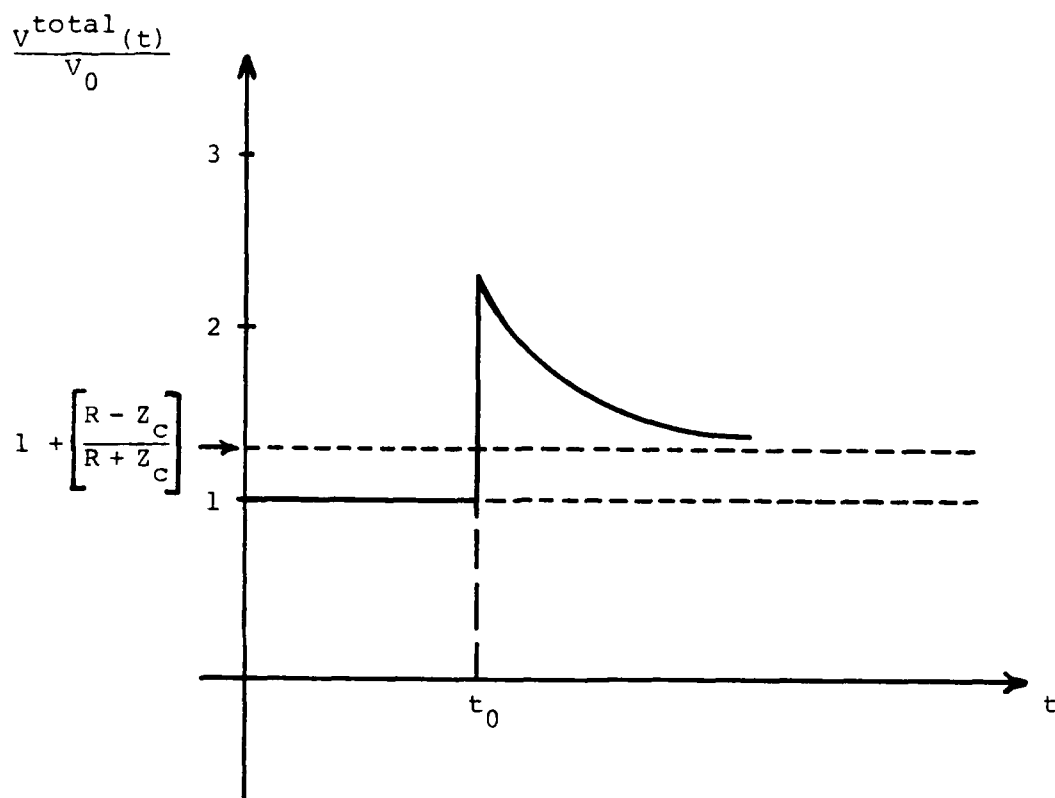
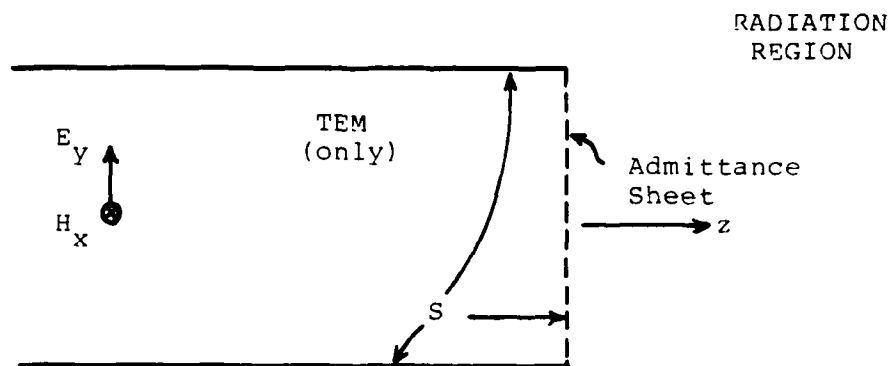
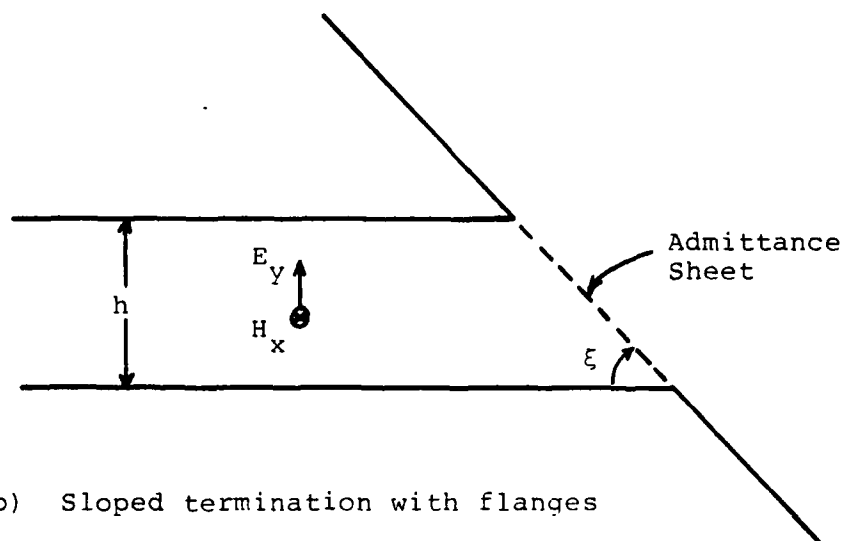


Figure 5.1. Step response of an RL terminator



(a) Infinitely wide parallel plates



(b) Sloped termination with flanges

Figure 5.2. Two idealized termination configurations

and the inductive part is given by

$$L \approx 0.6 \mu_0 h \quad (5.8)$$

where h , as shown in Figure 5.2, is the plate separation and μ_0 is the permeability of free space.

For the sloped terminations with flanges, the advantage of the sloping is that the required current in the terminator more quickly approaches (for a step-function incident wave) the late-time limiting current [5.3]. This is similar to a linear antenna where the induced current is "damped" out faster if it makes a sharper angle with the incident field.

Using a somewhat different approach, parameter studies for various values of the inductance L have been performed to find the minimum reflection [5.4, 5.5]. In the perpendicular case, the maximum TEM reflection coefficient is 0.032 when $L \approx 1.1 \mu_0 h$. For the sloped case with flanges, the following optimum values of L are obtained

Angle ξ	90°	75°	60°	45°	30°
$L/(\mu_0 h)$	1.10	1.06	0.91	0.67	0.40

In all these cases, the resistive part is given by

$$R = Z_0 \sin \xi \quad (5.7)$$

The optimum inductance value differs from that of reference [5.2] by a factor of 2.

It has to be cautioned that the above studies are for an idealized two-dimensional terminating sheet only. Results in [5.2] give the admittance values as a function of the vertical coordinate y , whereas the other references give only the total admittance value. All these values do not yield perfect matches over the entire frequency spectrum. Furthermore, in actual applications, the terminator is not in the form of a sheet,

but rather consists of many lumped resistances properly spaced to approximate the distributed effect. Also, in practice, the terminator contains no flanges.

V.4 Practical Considerations

1. Finite width terminator with lumped elements

It is far less expensive and mechanically superior to use arrays of resistor strings to approximate the admittance sheet described in the preceding subsection. Each resistor has its own internal inductance and each resistor string also has inductance due to coupling between the strings.

There are two main types of resistors that are suitable for this application: wire-wound resistor and carborundum resistor, the former contains more internal inductance than a comparable one of the latter type. A suitable design of the terminator may require no additional inductors to satisfy the requirements for a good termination.

Consider the termination as shown in Figure 5.3 with height h and width w , and making an angle ξ with the ground. There are N identical strings each with M resistors, each resistor has a length ℓ_R , radius r_R , resistance R and inductance L_R . For this configuration, the total internal inductance due to the $M \times N$ resistors is

$$L_i = \frac{M}{N} L_R \quad (5.10)$$

However there is also inductance due to the coupling between strings (the external inductance) [5.3] and [5.6],

$$L_e = \frac{M \ell_R}{N-1} \frac{\mu_0}{2\pi} \sin^2(\xi) \ln(d/2\pi r_R) \quad (5.11)$$

where $d = w/(N-1)$ is the string separation. Ignoring inductance due to the fringing field, the total resulting inductance of the terminator is

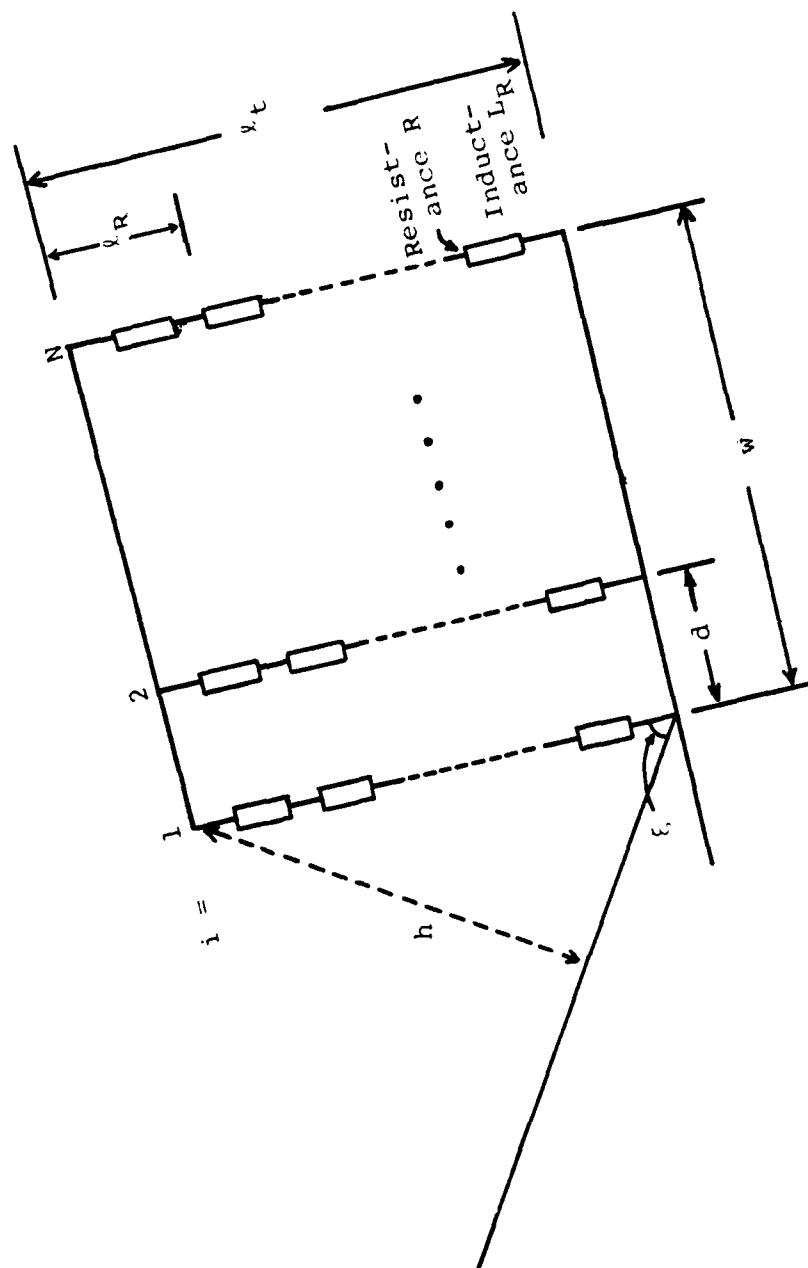


Figure 5.3. A practical terminator with resistor strings

$$L_t = L_i + L_e \quad (5.12)$$

and the resistance is

$$R_t = (M/N) R \sin \xi \quad (5.13)$$

It must be pointed out that the above formulas can be easily modified to cases where there is more than one type of resistor, or where the number of resistors is not the same on each string.

It is possible then to design so that R_t and L_t are good matches for the transmission line. For a practical terminator of finite width, the following values of impedance are considered to be optimum:

$$R_{opt} = Z_c \quad (5.14)$$

and

$$L_{opt} = (\ell_t/w) h \mu_0 \sin \xi \beta_h^{opt} f_a \quad (5.15)$$

$$\text{where } \beta_h^{opt} \approx \sin \xi \quad (5.16)$$

and f_a is a factor accounting for the fringe fields and $0 \leq f_a \leq 1$. Giri, et al. [5.6] estimated that

$$f_a \leq f_{TEM} \quad (5.17)$$

where f_{TEM} is the TEM mode fraction and is the fraction of the curvilinear squares contained within an area bounded by the simulator cross-section. The values of f_{TEM} can be estimated by studying TEM field plots [5.7].

2. Voltage and energy limitations

The resistors used must be able to withstand the voltage and energy that the transmission line delivers to the terminators.

(i) Air breakdown

For no breakdown of air, it is required that

$$\text{Maximum available voltage/h} < 10^6 \text{ V/m} \quad (5.18)$$

(ii) Resistor breakdown

For no breakdown of the resistors, it is required that

$$\text{Maximum rated voltage} > \text{maximum available voltage}$$

(iii) Energy deposition

The allowable energy deposition of the resistors must be larger than the available energy, i.e.,

$$(M \times N \times \text{allowable energy deposition}) > \frac{1}{Z_c} \int_0^{\infty} V^2(t) dt \quad (5.19)$$

where $V(t)$ is the voltage across the terminator.

3. Terminator geometry

The preceding discussions assume that the termination is rectangular in shape, that the resistor strings are in parallel, and that all resistors are identical. In practice, these conditions may not be met. As a matter of fact, there are advantages of using different configurations.

For a parallel-plate transmission structure such as ALECS, there is more current at the outer edges of the transmission line, consequently

- (1) less inductance should be placed near the outer edges
- (2) more resistor strings should be placed near the outer edges to withstand the higher current density there.

It is also desirable to put the largest impedance at the bottom center of the terminator since this location represents the maximum differential transit time between the incident TEM wave and the diffraction from the top of the terminator. This would tend to further "push" more current to the edges.

It has to be emphasized that the final configuration of the terminator is not easily designed but rather one should first design an idealized terminator and then experimentally adjust the elements to yield an optimum terminator. The experimental procedures are described in the following subsection.

4. Reflected energy

Since most of the energy of the EMP is contained at the lower end of the frequency scale, the spectrum of the reflected signal is also important in deciding if a terminator is satisfactory.

Assuming an EMP of the following waveform [5.8]

$$E(t) = E_0(e^{-\beta t} - e^{-\alpha t}) \quad (5.20)$$

where

$$\alpha = 2.2 \times 10^8 \text{ sec}^{-1}$$

$$\beta = 2.0 \times 10^6 \text{ sec}^{-1}$$

then for a particular radian frequency ω_0 , the fraction of EMP energy above ω_0 is given by

$$f_E(\omega > \omega_0) = \frac{\int_{\omega_0}^{\infty} |E(\omega)|^2 d\omega}{\int_0^{\infty} |E(\omega)|^2 d\omega} \quad (5.21)$$

Table 5.1 presents f_E as a function of frequency.

TABLE 5.1. PERCENTAGE OF ENERGY IN THE EMP WAVEFORM ABOVE A FREQUENCY f (MHz)

f (MHz)	0.01	0.1	1	5	10
f_E (%)	98	81	20	4	2

We observe that about 18% of the total EMP energy is between 1 to 10 MHz. This is the frequency region where principal resonances of aircraft occur. The simulator should be properly terminated within this frequency range. The range above 10 MHz is relatively less important.

V.5 Experimental Evaluation and Optimization

The design procedures given in the preceding subsection obtain, at best, parameter values that are close to optimum values. In practice, it is necessary to fine tune the parameters to yield optimum performances. The final adjustment can be done only with experimental procedures.

The method devised is based on the fact that after reflection from an interface, the reflected electric and magnetic fields are out-of-phase for the TEM mode. Let us denote the incident fields with a superscript (i) and the reflected fields with (r). Then, for the TEM mode

$$\tilde{E}_y^{(i)}(s) = \alpha \tilde{B}_x^{(i)}(s) \quad (5.22)$$

where α is a constant related to the characteristic impedance of the transmission line. The reflected fields are ideally given by

$$\tilde{E}_y^{(r)}(s) = \alpha(s) \tilde{E}_y^{(i)}(s) \quad (5.23)$$

and

$$\tilde{B}_x^{(r)}(s) = -\alpha(s) \tilde{B}_x^{(i)}(s) \quad (5.24)$$

This method of experimental procedures measures the time domain differential mode quantity $\tilde{\mathcal{E}}(t)$ which is the inverse Laplace transform of $\tilde{\mathcal{E}}(s)$ given by

$$\tilde{\mathcal{E}}(s) = \tilde{E}_Y^{(T)}(s) - \alpha \tilde{B}_X^{(T)}(s) \quad (5.25)$$

where the superscript (T) denotes the total fields. From equations (5.22) to (5.25), it is clear that, for the ideal TEM situation

$$\tilde{\mathcal{E}}(s) = \rho(s) [\tilde{E}^{(i)}(s) + \alpha \tilde{B}^{(i)}(s)] \quad (5.26)$$

Thus, if the incident electric and the magnetic fields are time synchronized for zero relative phase, and if their amplitudes are equalized, recording data in the differential mode has two advantages. First, the amplitude of the reflection is approximately doubled, and second, the two signal (incident) waveforms cancel, yielding an essentially horizontal baseline with the reflection showing up as the predominant feature. Henceforth, we will refer to this measurement as the differential mode of operation [5.6]. Time synchronization to within 0.5 ns was easily achieved by using signal cables of equal lengths. Amplitude matching was achieved by setting the vertical attenuator of the weaker signal channel to a convenient calibrated level and reducing the stronger signal to match using the (uncalibrated) variable attenuator. The experimental setup is illustrated in Figure 5.4. As can be observed in (5.26), if the terminator represents a perfect match, $\tilde{\mathcal{E}}(t)$ as measured would vanish. Thus, the fine tuning of the terminator parameters can be carried out, trying to minimize $\tilde{\mathcal{E}}(t)$.

V.6 Example

The preceding subsections give an overview of the theory and practice of terminators. Currently, the resistor strings approximation to the admittance sheet is the most

DIKEWOOD INDUSTRIES INC ALBUQUERQUE NM F/6 20/14
PARALLEL-PLATE TRANSMISSION LINE TYPE OF EMP SIMULATORS: SYSTEM--ETC(U)
MAY 80 D V 6IRI, T K LIU, F M TESCHE F29601-78-C-0045
DC-FR-1299-4 AFWL-TR-79-139 NL

UNCLASSIFIED

2 OF 2
AD
4085414

END
DATE
FILMED
8-80
DTIC

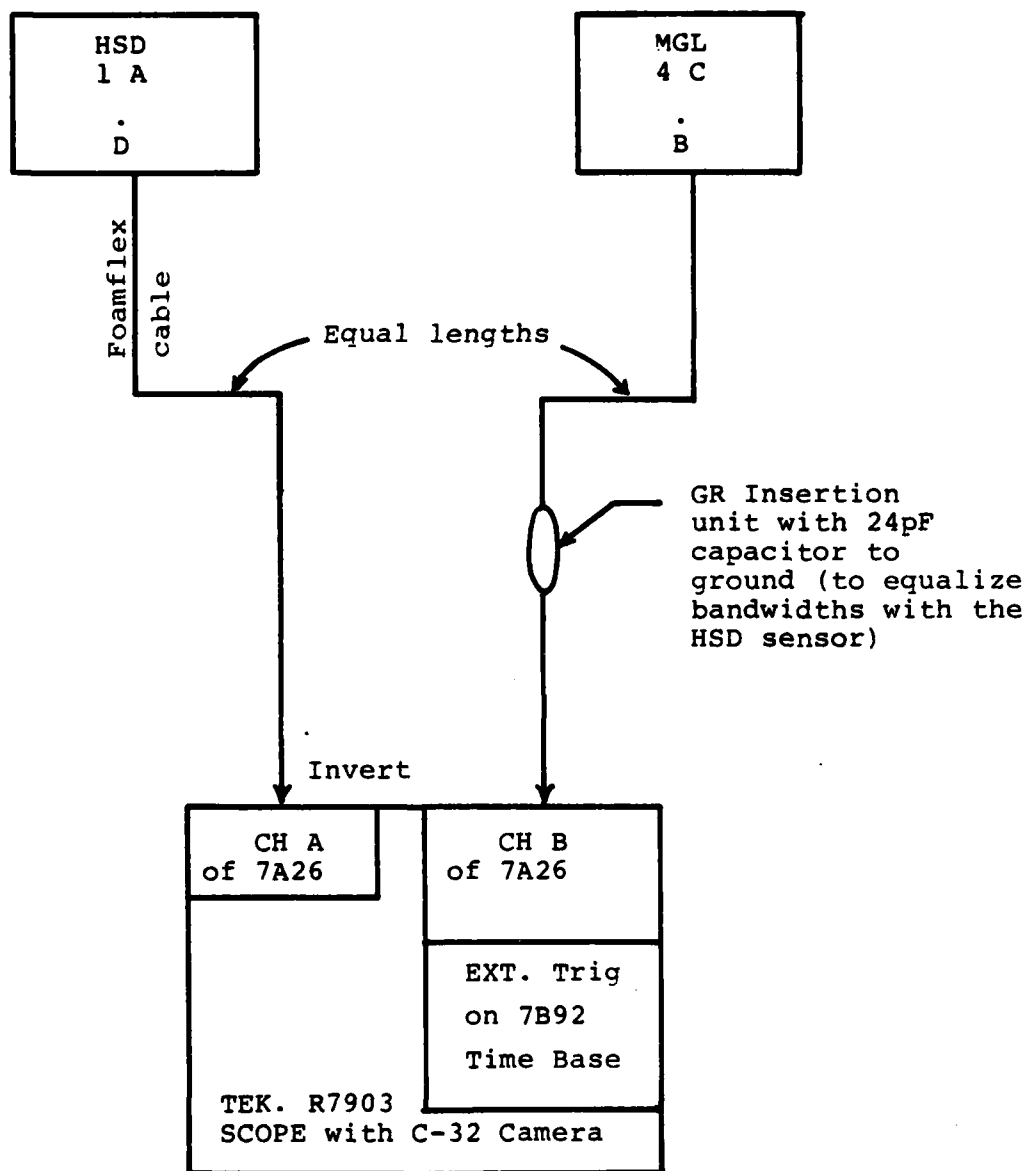


Figure 5.4. Equipment configuration including the capacitive insertion unit in channel B to equalize the bandwidths of the two sensors

useful approach. It is appropriate here to give a practical example of a terminator currently in use at AFWL. The example chosen is for the ALECS facility [5.6]. The final configuration of the terminator is shown in Table 5.2.

TABLE 5.2. FINAL TERMINATOR CONFIGURATION IN ALECS FACILITY

STRING NO. SPACE NO. i	1	2	3	4	5=N
1	SHORT	C-41	SHORT	C-01	SHORT
2	C-33	C-19	C-01	C-15	C-43
3	C-36	C-07	C-03	C-06	C-47
4	C-35	C-05	C-10	C-09	C-32
5	C-44	C-11	C-04	C-14	C-37
6	C-48	C-45	C-46	C-18	C-39
7 = M	C-31	C-41	C-30	C-40	C-13

Note: C refers to Carborundum resistors; also note that there are 5 strings with 7 resistors in each string, some of which were replaced by shorting aluminum inserts.

Initially, two types of resistors were used: the carborundum type denoted by C ($R = 70\Omega$ and $L_i = 0.008 \mu H$) and the wire-wound type denoted by w ($R = 80\Omega$ and $L_i = 1.2 \mu H$). However, the final configuration consisted of only the carborundum type. The terminator has the following pertinent parameters:

Terminator height h : 2.44 m
 Terminator width w : 4.57 m
 Terminator angle ξ : 36°
 Estimated final R_t : 89Ω
 Estimated final L_t :

We note that the two-dimensional analysis gives the following values:

Varvatsis and Sancer [5.4, 5.5]

$$R_t = Z_0 \sin \xi = 222\Omega$$

$$L_t = 1.5 \mu\text{H}$$

Latham and Lee [5.2]

$$R_t = Z_0 \sin \xi = 377\Omega$$

$$L_t = 3.4 \mu\text{H} \quad \text{for a } \xi = 90^\circ \text{ termination}$$

It is emphasized that in the final terminator configuration (see Table 5.2), there are no wire-wound resistors, and it is also observed that the inductance L_t is of the order of that of a single wire-wound resistor. Thus, one has to be very careful in arranging the resistors to obtain the low total inductance value.

V.7 Recommendations

The practical design procedures are very effective in bringing about a reasonably good terminator, which could be improved through experimental procedures (the differential mode of operation and evaluation). This technique should be implemented for other terminator designs and installations. However, experimental efforts are time consuming, particularly in the ATLAS I (TRESTLE) facility, whose terminator is very high above ground level. Thus, accurate design is essential to minimize experimental efforts in changing individual resistors, etc.

As mentioned earlier, wire-wound resistors have very high internal inductances, and very careful design is necessary to obtain the required total inductance. The design of the ALECS terminator had initially utilized a combination of carborundum and wire-bound types of resistors, but in the final configuration only the carborundum resistors were

found useful. In spite of using the low-internal inductance carborundum resistors, the residual reflection was found to be inductive, indicating that a further reduction in inductance was desirable, but not practical at the time. It may be possible, however, to design different configurations to achieve the same R_t and L_t values.

In conclusion, one might point out that other alternate designs are possible for the resistor arrangement and an efficient experimental scheme or procedure is available for the evaluation of termination performance.

VI A REVIEW OF AVAILABLE EXPERIMENTAL WORK

VI.1 Introduction

The purpose of an HEMP simulator is to provide an electromagnetic environment that approximates a traveling electromagnetic pulse composed of a spectrum of frequencies extending from very low to moderately high. For each component frequency the electromagnetic field is a plane wave with mutually perpendicular electric and magnetic vectors that satisfy the relation $\vec{E} = \vec{c} \times \vec{B}$, where \vec{c} is in the direction of propagation. It has the magnitude $c = 3 \times 10^8$ m/sec. One type of structure that is designed to generate an approximation of such a field is the guided-wave simulator which ideally has the properties of a uniform transmission line for the TEM mode at sufficiently low frequencies. That is, it has a characteristic impedance that is independent of the frequency and position along the direction of propagation, and it can be terminated to provide a pure traveling wave at every cross section. Unfortunately, it is not obvious nor easily proved that the electromagnetic field in an actual simulator adequately approximates the desired properties at any or all frequencies in the pulse. The geometries of the different structures in actual use are such that a rigorous, quantitatively accurate analysis is very difficult. It follows that recourse must be had in numerical investigations or in direct measurements. Actually, an accurate and complete experimental study of the electromagnetic field in the working volume of a guided-wave simulator is faced with many difficulties. It is the purpose of this section to describe such a study in the model simulator at Harvard University and, in order to make them meaningful, to interpret the measurements with the help of approximate, but instructive, theoretical results.

VI.2 The Harvard EMP Simulator

A detailed experimental study has been made of the electric field in the guided-wave simulator shown schematically in Figures 6.1 and 6.2. The simulator consists of a rectangular metal plate between sloping triangular plates supported over a large aluminum ground plane (7.93×3.35 m) by dielectric cables and styrofoam blocks. It is driven at one end by the vertical extension of the inner conductor of a coaxial line connected to a CW power oscillator. The simulator is terminated at the other end in standard two-watt resistors in parallel. The three-dimensional region under the rectangular plate is where the fields have been mapped. The length ℓ of the simulator is 115 cm, and its width $2a$ is 175 cm. Its height b above the ground plane is adjustable with the help of hinged joints between it and the sloping triangular plates combined with movable feed and load points. Two heights and frequencies have been used. They are $b \approx 108$ cm with $f \approx 625$ MHz or $\lambda = 48$ cm so that $b/\lambda = 2.25$, and $b = 75$ cm with $f = 264$ MHz or $\lambda = 113.6$ cm so that $b/\lambda = 0.66$. The altitude of each of the identical triangular plates is 331 cm and their projections on the ground plane when $b = 108$ cm are 311.5 cm, when $b = 75$ cm the projections are 322 cm. These dimensions provide a characteristic impedance of 100Ω when $b = 108$ cm, of 80Ω when $b = 75$ cm. A small corner reflector is placed behind the driven end; absorbing material completely surrounds the edges of the ground plane.

Cartesian coordinates are used to describe the location of a point in and near the working volume of the simulator. The origin is on the ground plane directly below the center of the parallel plate. The unit vectors \hat{i}_x , \hat{i}_y , \hat{i}_z define, respectively, the transverse, vertical, and longitudinal directions, as indicated in Figure 6.2. Note that \hat{i}_z points in the direction of propagation. For preliminary measurements

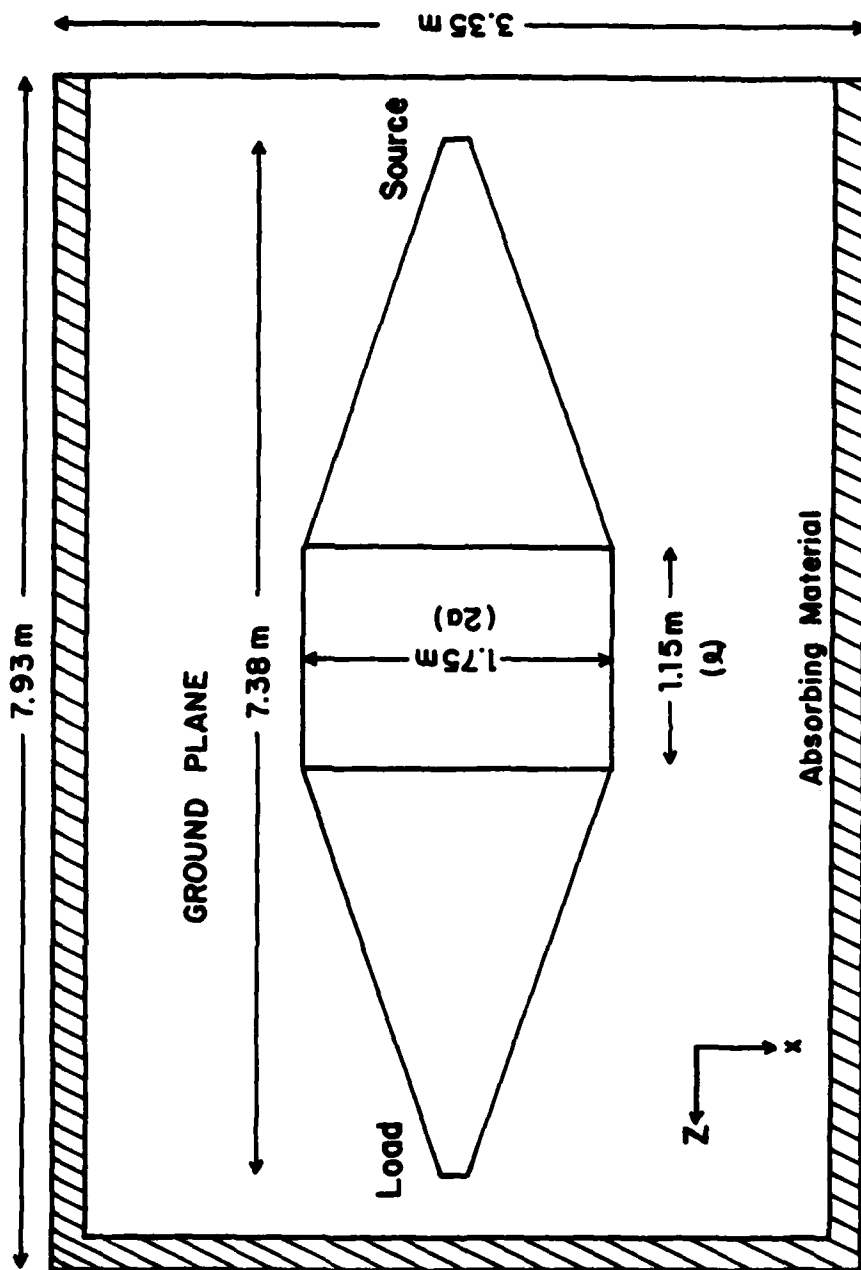


Figure 6.1 Top view of simulator setup

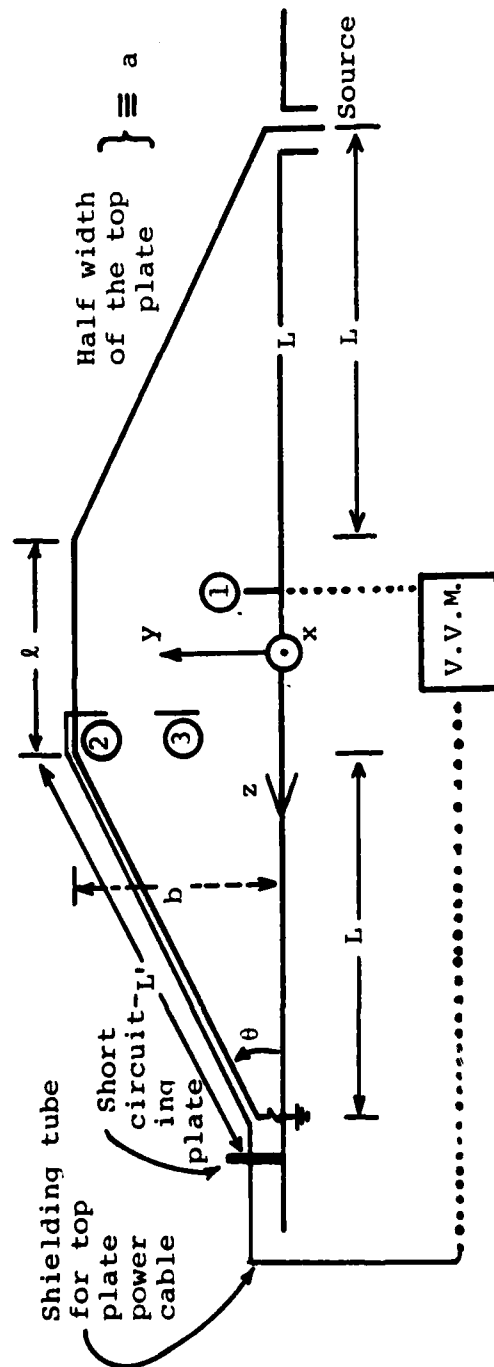


Figure 6.2. Simulator with (1) ground-plane probe, (2) top-plate probe and (3) space probe in the parallel plate region; the dimensions are $L = 3.11 \text{ m}$, $L' = 3.31 \text{ m}$, $l = 1.15 \text{ m}$, $a = .875 \text{ m}$, $b = 1.08 \text{ m}$ and $.75 \text{ m}$

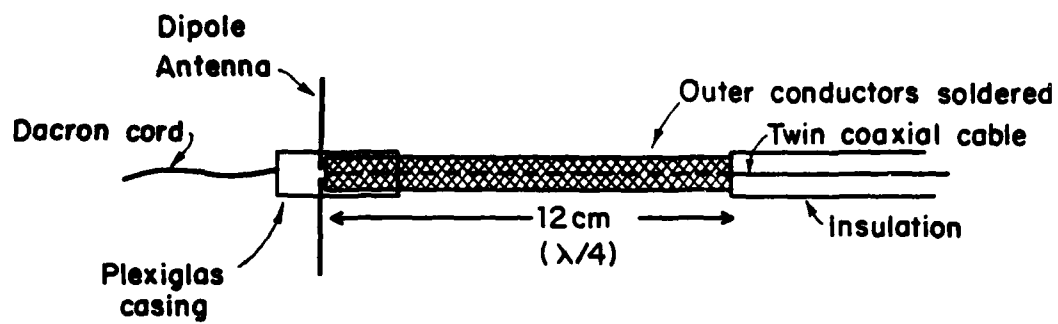
the spherical coordinates (r, ϕ, θ) are also used with the origin $(r=0)$ on the ground plane at the driving point. When $b = 108$ cm, the load is at $(r, \phi, \theta) = (738, 90^\circ, 0^\circ)$, where r is in centimeters.

In order to determine the electric field in the parallel plate region and in the adjacent conical sections as well as along the surfaces of the ground plane and the upper parallel plate, a system of movable probes was designed and constructed for the direct measurement of both the amplitude and phase of E_z and E_y . As explained later, a small component E_x exists primarily near the open sides where fringing occurs, but this could not be measured. The component E_y on the ground plane was measured with a monopole probe, 4 cm long, mounted on a brass disk 10 cm in diameter and designed to slide along the ground plane when moved by means of a pulley system. The probe cable was constrained to lie flat on the ground plane and was, therefore, always perpendicular to the electric field. The measurement of E_y on the underside of the upper parallel plate was accomplished with a monopole probe that projects down into the parallel plate region through longitudinal slots cut into the parallel plate. The probe was mounted on a brass block which was machined to slide in the slots. The output cable from the base of the probe was placed in a shielding tube constructed to lie along the upper surface of the sloping triangular plate leading to the load. The cable in its shielding tube extended beyond the load parallel to the ground plane and over its edge to the instrumentation below, as shown in Figure 6.2. The section over the ground plane constituted a transmission line with a characteristic impedance of 100Ω . It was short-circuited at a distance of $\lambda/4$ from the load by a metal plate and so acted like an open circuit at the load.

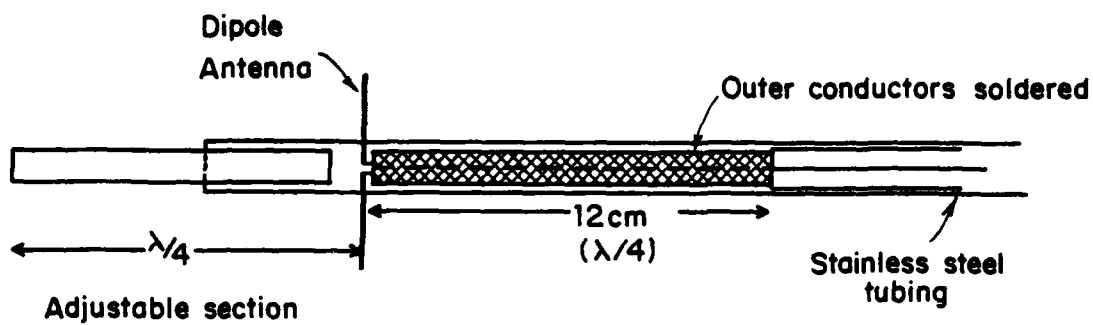
The electric field throughout the parallel plate region was measured with a dipole antenna that could be oriented vertically to measure E_y and horizontally to measure E_z . It was continuously movable in the parallel plate region and adjacent sections below the conical plates. The probe cable consisted of twin coaxial lines that were held parallel to the transverse x-axis as the probe was moved. This assured that the coaxial lines were perpendicular to both E_z and E_y , but necessarily parallel to E_x --which could excite axial standing-wave distributions of current and charge on their surfaces. Since the standing wave distributions would have a charge maximum at the end adjacent to the terminals of the dipole, they could induce an undesired voltage across the terminals if complete geometrical symmetry did not obtain. No such difficulty was encountered with $f = 625.5$ MHz and the simple space probe (a) shown in Figure 6.3 was used to measure E_z and E_y throughout the parallel plate region. At $f = 264$ MHz, an undesired voltage due to E_x was observed--presumably because the long twin cable from the probe in the working volume to the vector voltmeter under the ground plane happened to be near a resonant length. This difficulty was avoided by enclosing the twin cables in a metal tube provided with an adjustable extension beyond the dipole, as shown in the diagram for space probe in Figure 6.3b. When the extension was adjusted to a quarter wavelength, the dipole was located at a charge minimum, instead of a charge maximum, in any standing wave induced on the tube by E_x . The undesired voltage across the terminals of the evidently not perfectly symmetrical dipole was thus reduced to a nonobservable value.

VI.3 Preliminary Measurements

Before measurements were made in the model simulator, the standing-wave pattern on the ground plane with its surrounding absorbing walls was investigated. The source was a



SPACE PROBE (a)



SPACE PROBE (b)

Figure 6.3 Diagrams of space probes

short monopole at the location of the driving-point of the simulator, $(r) = (0)$, backed by a small corner reflector. The frequency was $f = 626.5$ MHz or $\lambda = 48$ cm. By means of the movable monopole probe, the electric field E_y along the radial line $\theta = 0^\circ$ was measured in both amplitude and phase, as shown by solid lines in Figure 6.4. It corresponds to the spherical traveling wave $E_y = Ae^{ikr}/r$ with a superimposed standing-wave ripple. In order to determine the predominant cause of the reflections that generate the standing wave, a reflecting plane was placed successively in three positions. For the first location normal to the direction of propagation at $r = s = 606$ cm, the field distribution shown in Figure 6.4 in dotted lines was obtained. This resembles the graphs in solid line, but with a substantially higher standing-wave ratio. For the second location the reflecting plate was moved away from the source a distance of one quarter wavelength to $s = 618$ cm. The new field distribution was like the dotted one in Figure 6.4, but with the entire standing-wave pattern moved away from the source a distance of a quarter wavelength. A theoretical curve for the field when the reflecting plane at $s = 606$ cm is infinite in extent is shown in Figure 6.5 for comparison with the measured dotted graphs in Figure 6.4. The third location of the reflecting plane was normal to the x-direction and flat against the absorbing material on one side at $x = -136$ cm. The field measured in this case differed negligibly from that in the absence of any reflecting plane, shown in solid lines in Figure 6.4. These tests indicate that the reflections that produce the small standing wave shown by the solid-line graphs in Figure 6.4 originate at the rear edge and wall of the absorbing material. Their small amplitude shows that while there is some reflection from the edge of the ground plane and the absorbing material, this latter is generally effective in providing a predominantly traveling wave that closely approximates that over a plane of infinite extent.

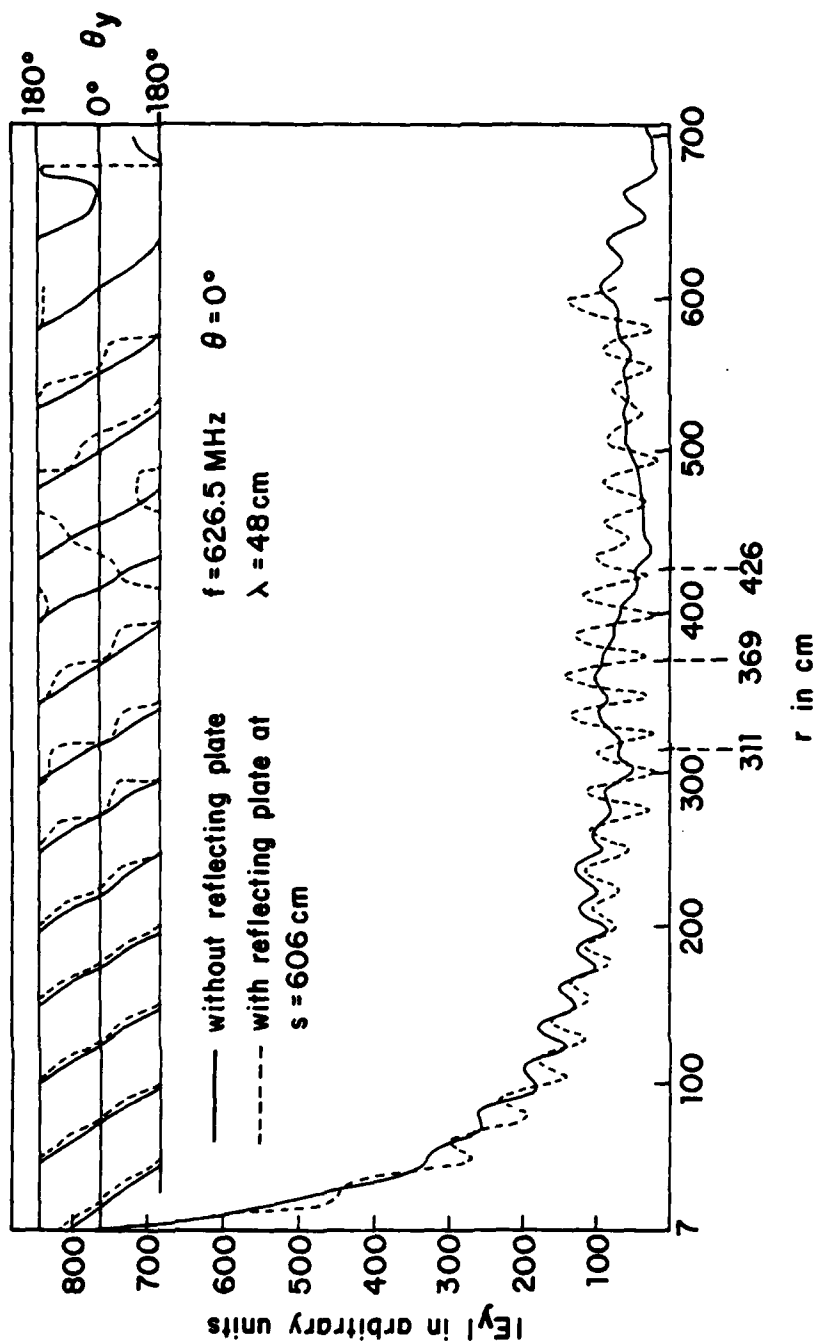


Figure 6.4. Measured E_y along $\theta = 0^\circ$ on ground plane excited by monopole and corner reflector

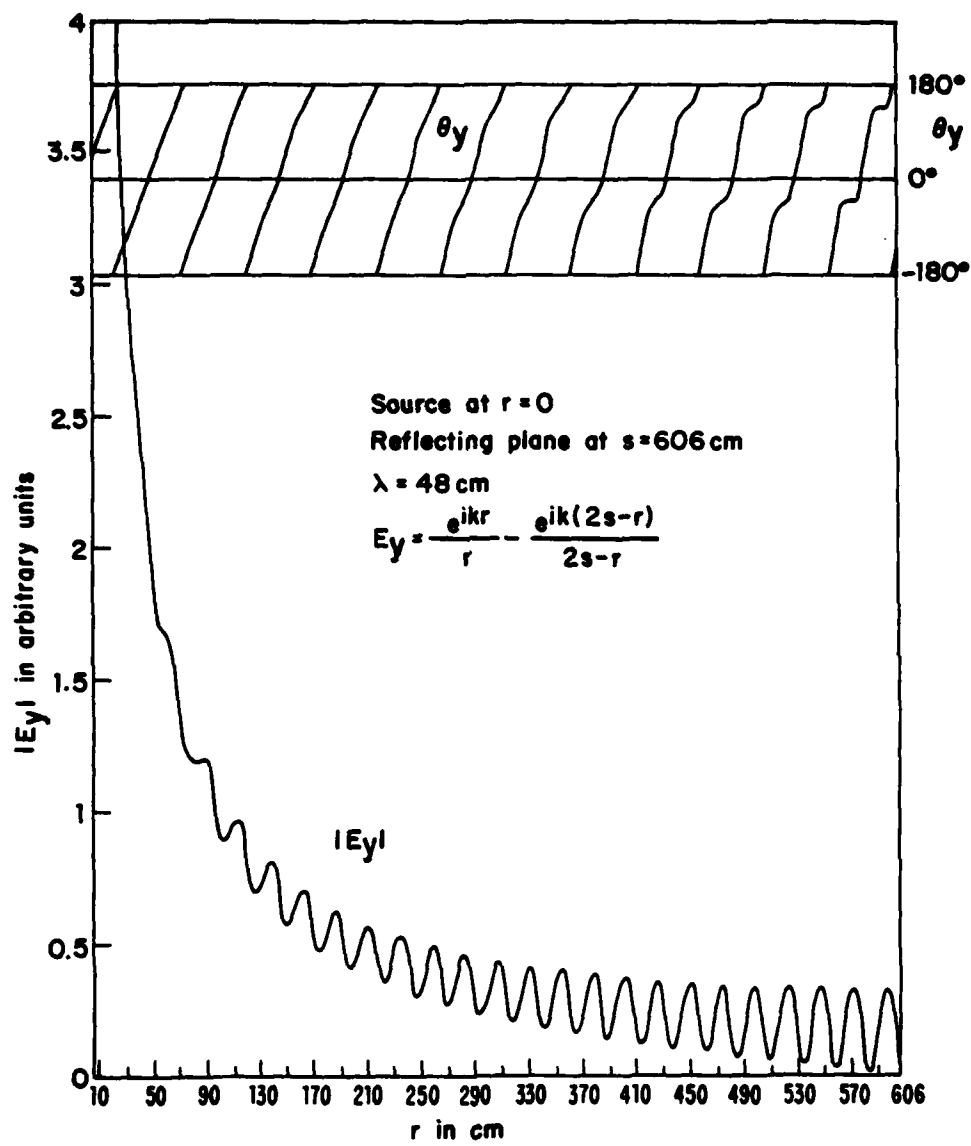


Figure 6.5. Theoretical electric field along $\theta = 0^\circ$ on ground plane for comparison with measured graphs in Figure 6.4

The next set of preliminary measurements was carried out with the parallel rectangular and sloping triangular plates of the simulator in place and with a load of 105Ω as the termination. This value was chosen after measurements showed that it provided the lowest standing-wave ratio in the region near the load. Graphs of $|E_y|$ and $|\theta_y|$ are shown in Figure 6.6 for a distance of more than a wavelength adjacent to the 105Ω load. The standing-wave ratio of 3.7 shows that there is substantial reflection even with the "matched" load at this frequency of 626.5 MHz. There are other parameters related to the terminator, namely, the location, orientation of resistors, that one can vary. It is expected that such experimental optimization of the terminator will be attempted later. In Figure 6.7 are shown the graphs of E_y and θ_y along the ground plane corresponding to those in solid lines in Figure 6.4, but now with the simulator plates in place. There is no dramatic difference. The main outline is still that of a traveling spherical wave with a superimposed standing wave. The latter is somewhat reduced near the source, somewhat enhanced near the load.

It may be concluded from these and other preliminary measurements of E_y along the ground plane, that the field incident on the parallel-plate region is essentially a traveling spherical wave with a superimposed standing wave of relatively small amplitude.

VI.4 Introductory Description of the Field in the Parallel Plate Region

In order to provide a meaningful set of measurements of the electromagnetic field in the parallel-plate region and adjacent sections of the tapered ends, it is necessary to review briefly the elementary theoretical foundations. Consider first the field at frequencies that are sufficiently low to make the height b a negligible fraction of a wavelength, i.e., $kb = 2\pi b/\lambda \ll 1$. In this important range, the entire

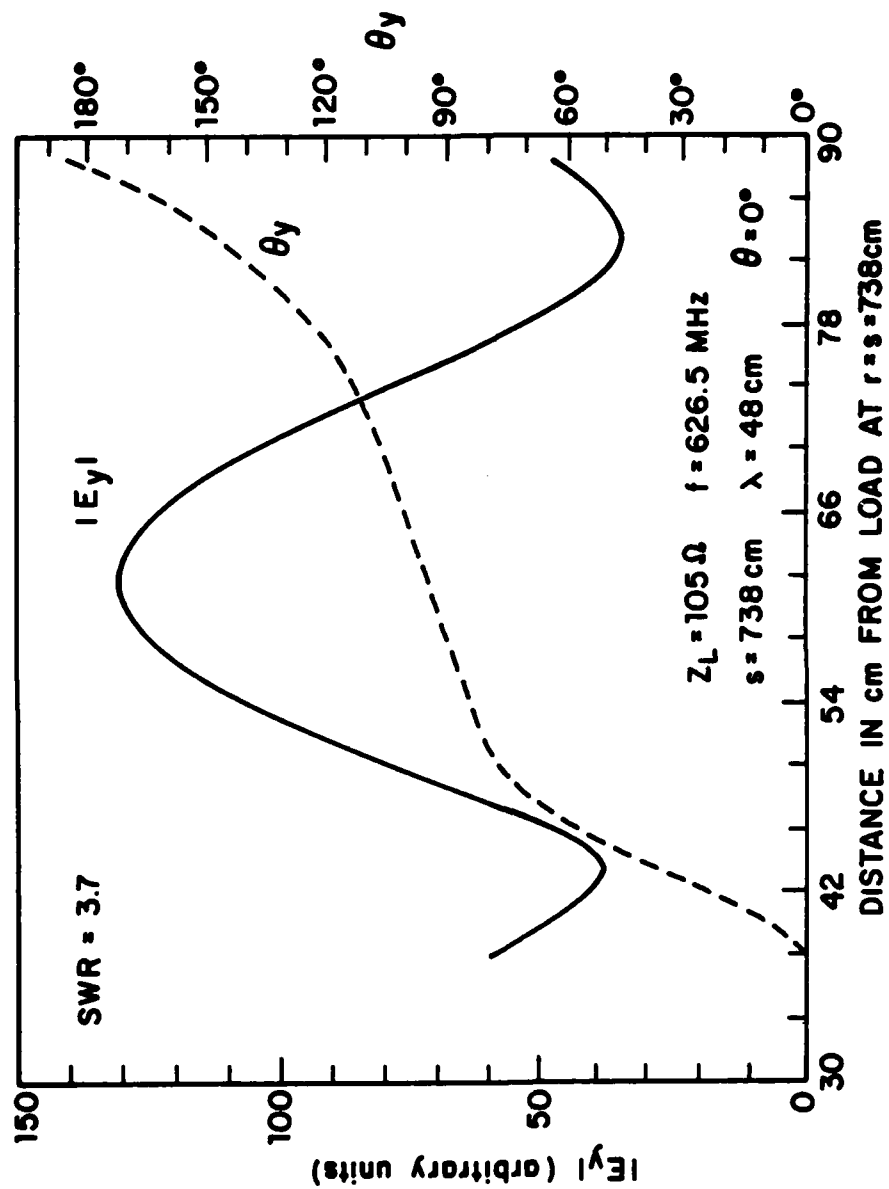


Figure 6.6. Standing wave of the $|E_y|$ near load

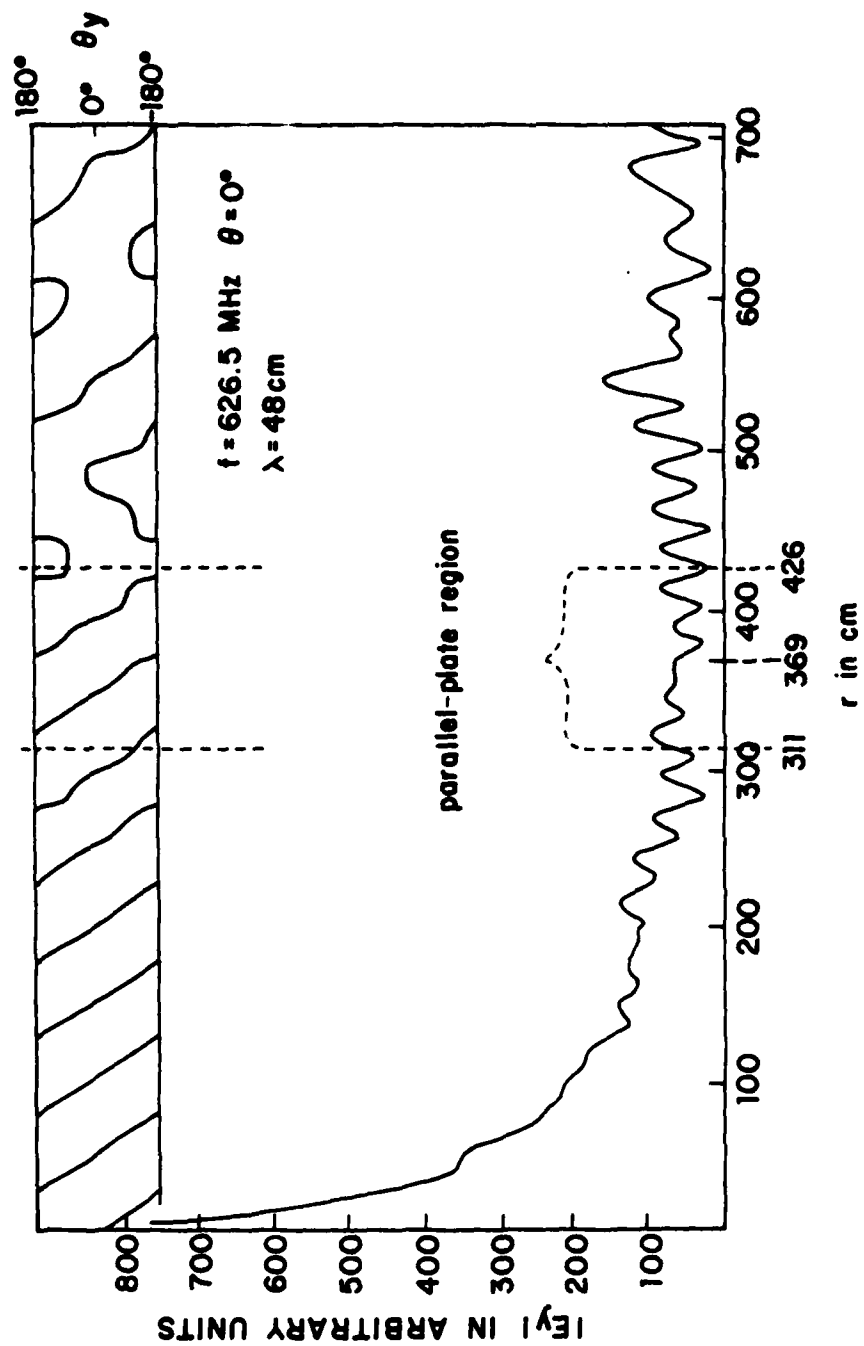


Figure 6.7. Measured E_y along $\theta = 0^\circ$ of ground plane of terminated simulator

structure has the properties of an end-loaded transmission line operating in the TEM mode with negligible radiation, low line losses, a constant characteristic impedance, and a standing-wave ratio determined by the terminating load impedance. The TEM electric field in the working volume is vertically directed and approximately independent of the transverse coordinates x and y at points not too close to the side edges of the plates where fringing effects occur. That is, $\vec{E}(x,y,z) \approx \hat{z} E_y(z)$. $E_y(z)$ is proportional to $V(z)$, the transmission-line voltage across the conductors. The planes $z = \text{constant}$ are ideally surfaces of constant amplitude $|E_y|$ and phase θ_y . The incident wave travels in the positive z -direction, the reflected wave in the negative z -direction. With a proper termination $Z_L = Z_c$, the reflected wave from the load can be reduced to a negligible value. However, reflections do take place at the discontinuities at the junctions of the parallel plate and the sloping triangular end plates.

When the frequency is so high that kb is not small, in particular, when $kb = 2\pi b/\lambda = 4.5\pi$ or $b = 2.25\lambda$ as for the Harvard simulator at the operating wavelength $\lambda = 48$ cm and the height $b = 108$ cm, the electric field in the parallel plate region is much more complicated. This is true to a lesser degree when $kb = 1.32\pi$ or $b = 0.66\lambda$ as for the Harvard simulator when $\lambda = 113.6$ cm and $b = 75$ cm. Owing to the wide spacing, most of the energy supplied by the generator is now radiated into the surrounding space, and only a small fraction is dissipated in the load. The structure is essentially an antenna and not a transmission line. This has been confirmed by SooHoo [6.1] in a numerical analysis of a comparable simulator. He concludes that in the high-frequency region the radiated power approaches 80% of that supplied by the generator.

In order to understand the characteristics of the measured field and to relate them to the simple TEM field that

dominates at low frequencies, it is advantageous to have an at least approximate theoretical representation of the field in the working volume. Owing to its finite size and connection to the sloping triangular driving and loading members, the working volume is not simply a section of an ideal parallel-plate waveguide of infinite length. No general analytical treatment of the complete simulator has been made. Analyses are available of infinitely long, parallel-plate waveguides with plates that have a finite width that is arbitrary, Dudley and Quintenz [6.2], Rushdi, et al. [6.3], or that is very narrow Marin [6.4], very wide Marin [6.5], Marin and Lewis [6.6], or infinitely wide Marcuvitz [6.7]. None of these provides any information on the fields in and the transmission-line properties of the long sloping triangular sections or of the junction region between them and the parallel-plate region. Unfortunately, they also provide primarily qualitative information about the fields in the parallel-plate section since this is only 115 cm long, but 175 cm wide and (with image) 216 cm (or 150 cm) high. Thus, the condition of infinite length (or at least great length compared with the transverse dimensions) implicit in all of the analyses of parallel-plate waveguides is not satisfied. Indeed, the parallel-plate section is relatively so short that end effects can be expected to be significant over much of its length. Even so, the theoretical representation of the field in an ideal parallel-plate waveguide in terms of propagating TEM, TM, and TE modes should provide the best available framework for interpreting the measured field in the working volume of the model simulator.

VI.5 The Field in the Parallel-Plate Section; TEM and TM Modes

Since the field incident on the parallel-plate section of the simulator is a spherical wave, it is of interest to

determine the nature of the phase fronts which characterize the electromagnetic field in that section. Measured graphs of the wave fronts or contours of constant phase, $\theta_y = \text{constant}$, of the vertical component E_y of the electric field in the parallel-plate region when $b = 108 \text{ cm}$ and $f = 626.5 \text{ MHz}$ are shown in Figures 6.8a and 6.8b in vertical yz planes at discrete values of x ranging from $x = 1.7 \text{ cm}$ near the center at $x = 0$ to $x = -70.3 \text{ cm}$ near the edge at $x = -87.5 \text{ cm}$. Also shown are the wave fronts of a spherical wave originating at the driving point ($x = 0, z = -369 \text{ cm}, y = 0$). Clearly the phase fronts throughout the parallel-plate region are essentially spherical with a superimposed oscillation due to reflections from the top plate.

It is not convenient to describe the field in a parallel-plate waveguide in terms of spherical wave fronts originating at an outside point. The natural representation is in terms of a superposition of plane waves known as parallel-plate modes. The simplest form is given by the mode theory of infinite parallel planes [6.7]. Applicable to the parallel-plate section of the simulator are the TM modes symmetric in y supplemented if desired with the more complicated theory for plates of finite width [6.2 to 6.6]. The significance of TE modes is considered in a later section. Using the relevant TM modes* given in reference [6.7] one can write the field quantities for the various modes.

For the Harvard working volume and with the operating frequency at $f = 626.5 \text{ MHz}$, the TEM mode with $n = 0$ and three TM_{0n} modes with $n = 1, 2, 3$, can propagate. For the TEM mode, $k = k_{g0} = 0.1309 \text{ cm}^{-1}$; for the TM_{0n} modes, $k_{g1} = 0.977k = 0.128 \text{ cm}^{-1}$, $k_{g2} = 0.893k = 0.117 \text{ cm}^{-1}$, and $k_{g3} = 0.748k = 0.098 \text{ cm}^{-1}$. The corresponding guide wavelengths

* When referred to the full height with image, b is replaced by $2b$, and $n = 0, 2, 4, 6, \dots$, instead of $0, 1, 2, 3, \dots$.

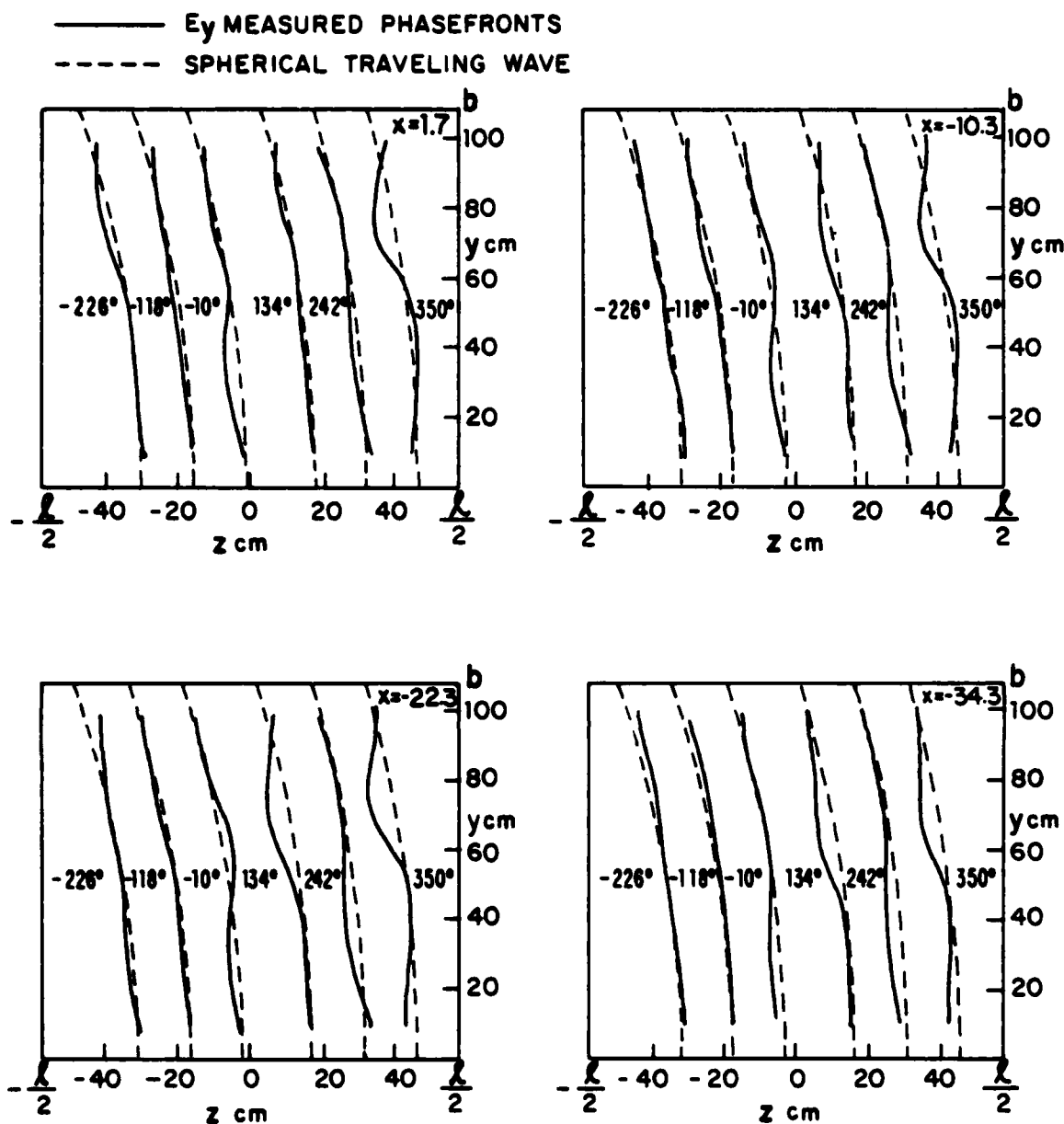


Figure 6.8a. Measured constant phase curves in the working volume; $b = 108$ cm, $l = 114.8$ cm, $f = 626.5$ MHz

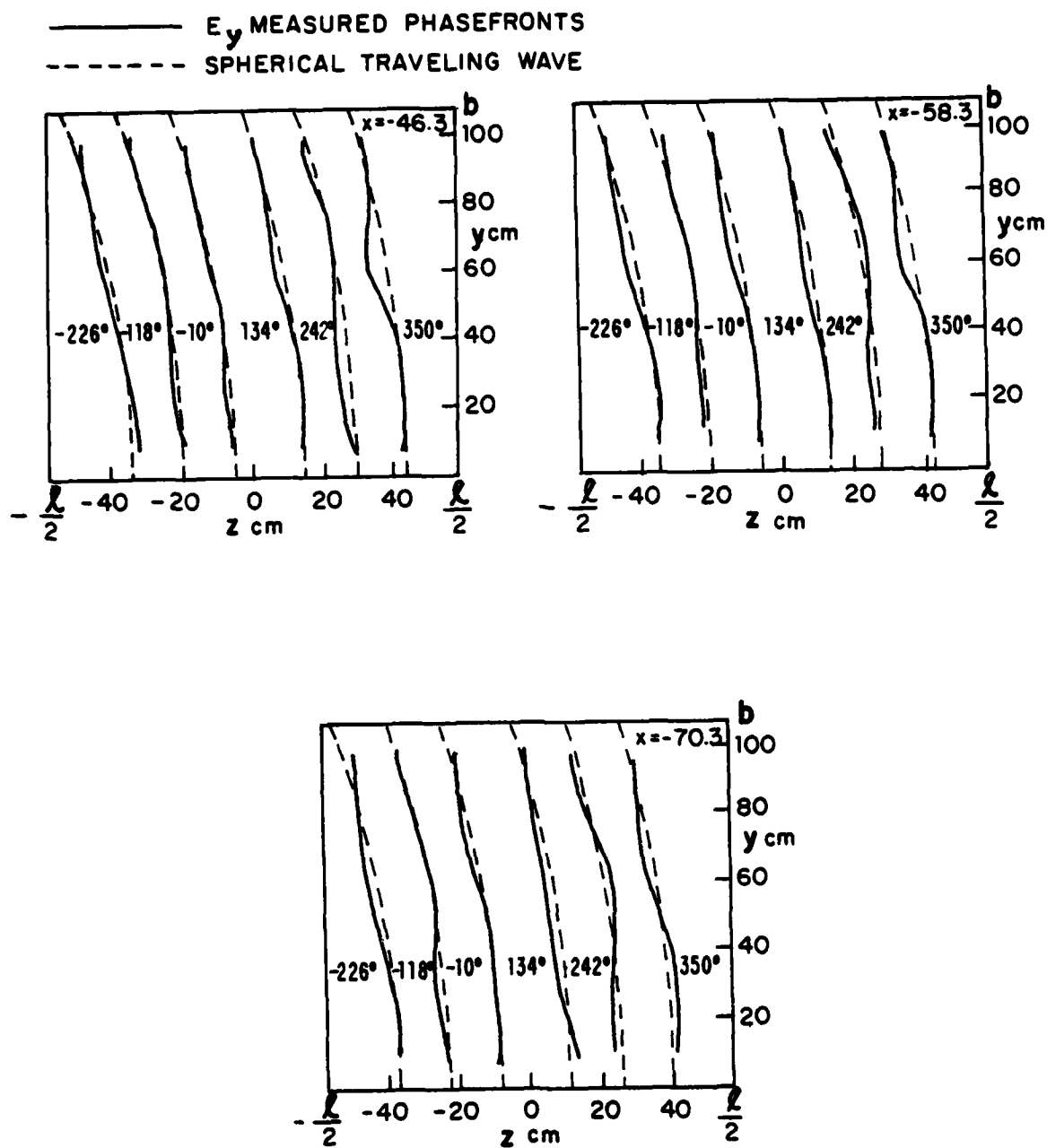


Figure 6.8b. Measured constant phase curves in the working volume; $b = 108$ cm, $l = 114.3$ cm, $f = 626.5$ MHz

are $\lambda = \lambda_{g0} = 48$ cm for the TEM mode and $\lambda_{g1} = 49.1$ cm, $\lambda_{g2} = 53.7$ cm, and $\lambda_{g3} = 64.2$ cm for the TM_{0n} modes. The fields for the four modes are:

$$\text{TEM: } E_z = 0, \quad E_y = 0.096V_0(z), \quad H_x = 0.096I_0(z) \quad (6.1)$$

$$\begin{aligned} \text{TM}_{01}: E_z &= -111.4I_1(z)\sin(.029y), \quad E_y = -0.136V_1(z)\cos(.029y) \\ H_x &= 0.136I_1(z)\cos(.029y) \end{aligned} \quad (6.2)$$

$$\begin{aligned} \text{TM}_{02}: E_z &= -122.8I_2(z)\sin(.058y), \quad E_y = -0.136V_2(z)\cos(.058y) \\ H_x &= 0.136I_2(z)\cos(.058y) \end{aligned} \quad (6.3)$$

$$\begin{aligned} \text{TM}_{03}: E_z &= -134.2I_3(z)\sin(.087y), \quad E_y = -0.136V_3(z)\cos(.087y) \\ H_x &= 0.136I_3(z)\cos(.087y) \end{aligned} \quad (6.4)$$

The relative amplitudes of the incident and reflected waves for each of these modes are not readily determined analytically. However, they can be estimated at any cross section of the parallel plate region by comparison with the measured field.

The electric field lines characteristic of the TEM and first three TM_{0n} modes are shown in the yz -plane in Figure 6.9. At the upper left are the exclusively vertical field lines of the TEM mode. They have alternate upward and downward maxima at intervals of $\lambda/2 = 24$ cm. Note that there is no associated component E_z . At the upper right are the electric field lines for the TM_{01} mode. These resemble the TEM mode near the top conductor, but are oppositely directed near the ground plane since they are parts of closed loops with an E_z component in the region halfway between the conducting surfaces. The alternating upward and downward maxima now occur at intervals of $\lambda_{g1}/2 = 24.6$ cm. On the lower left are the E-lines for the TM_{02} mode, on the lower right those of the TM_{03} mode. These have additional closed loops in the vertical

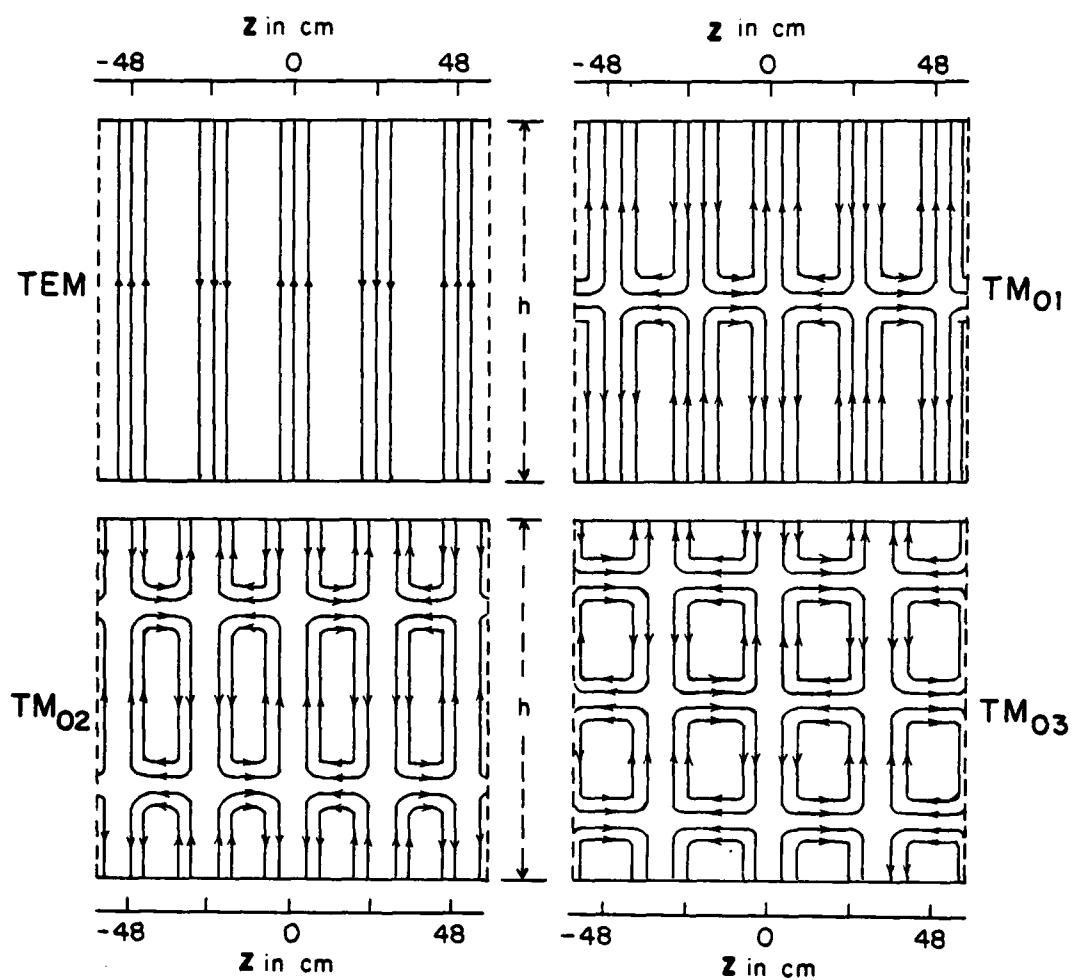


Figure 6.9. Electric field lines for four parallel-plate modes in working volume $\lambda = 48$ cm

direction with associated E_z -components and a wider spacing between successive maxima in the horizontal direction. Thus, for the TM_{02} mode, the maxima occur at intervals of $\lambda_{g2}/2 = 26.8$ cm, for the TM_{03} mode at intervals of $\lambda_{g3}/2 = 32.1$ cm. Axial distributions of the four modes are shown in Figure 6.10 with an assumed standing-wave ratio of 1.36 for each: Note that for the TEM mode at the bottom, there are four half-wavelengths in the range $-48 \text{ cm} \leq z \leq 48$ cm, whereas for the TM_{03} mode at the top, there are only three half-wavelengths in the same range.

When $b = 75$ cm and $f = 264$ MHz or $\lambda = 113.6$ cm, the only propagating TM modes are the TEM mode and the TM_{01} mode. For the latter, the cut-off wavelength is $\lambda_{c1} = 2b = 150$ cm and the guide wavelength is $\lambda_{g1} = 174$ cm.

VI.6 The Measured Field in the Working Volume:

$$b = 2.25\lambda = 108 \text{ cm}; \quad f = 626.5 \text{ MHz}$$

The principal components, E_y and E_z , of the electric field in the working volume were measured as functions of the longitudinal variable z with the transverse variables x and y as the parameters. Consider first the field with $f = 626.5$ MHz when $b = 108 \text{ cm} = 2.25\lambda$ and $\lambda = 48$ cm. (The field with $b = 75 \text{ cm} = 0.66\lambda$ with $\lambda = 113.6$ cm is studied in the next subsection.)

In Figure 6.11 are shown measured distributions of $|E_y|$ and $|E_z|$ in the yz -plane at $x = 1.7$ cm, i.e., very near the central plane $x = 0$ of the parallel-plate region. The parameter y/b ranges from 0 at the bottom to $y/b = 1$ at the top. The field along the ground plane $y/b = 0$ was measured with the monopole probe mounted on the movable metal disk; the field along the underside of the top plate was measured with the monopole probe that moves in the longitudinal slots. The field at all other values of y/b was measured with the movable dipole space probe that is supported by a

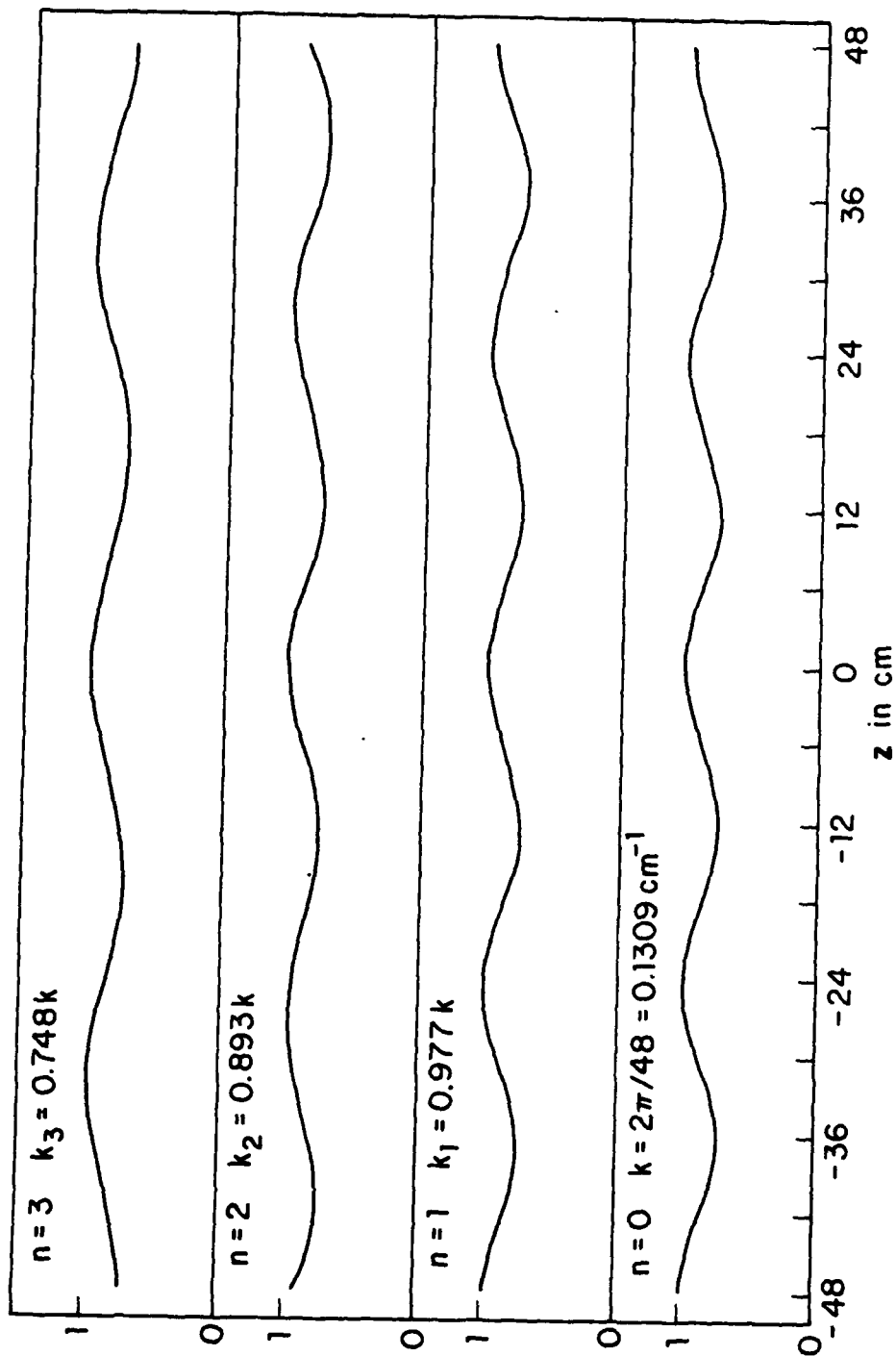
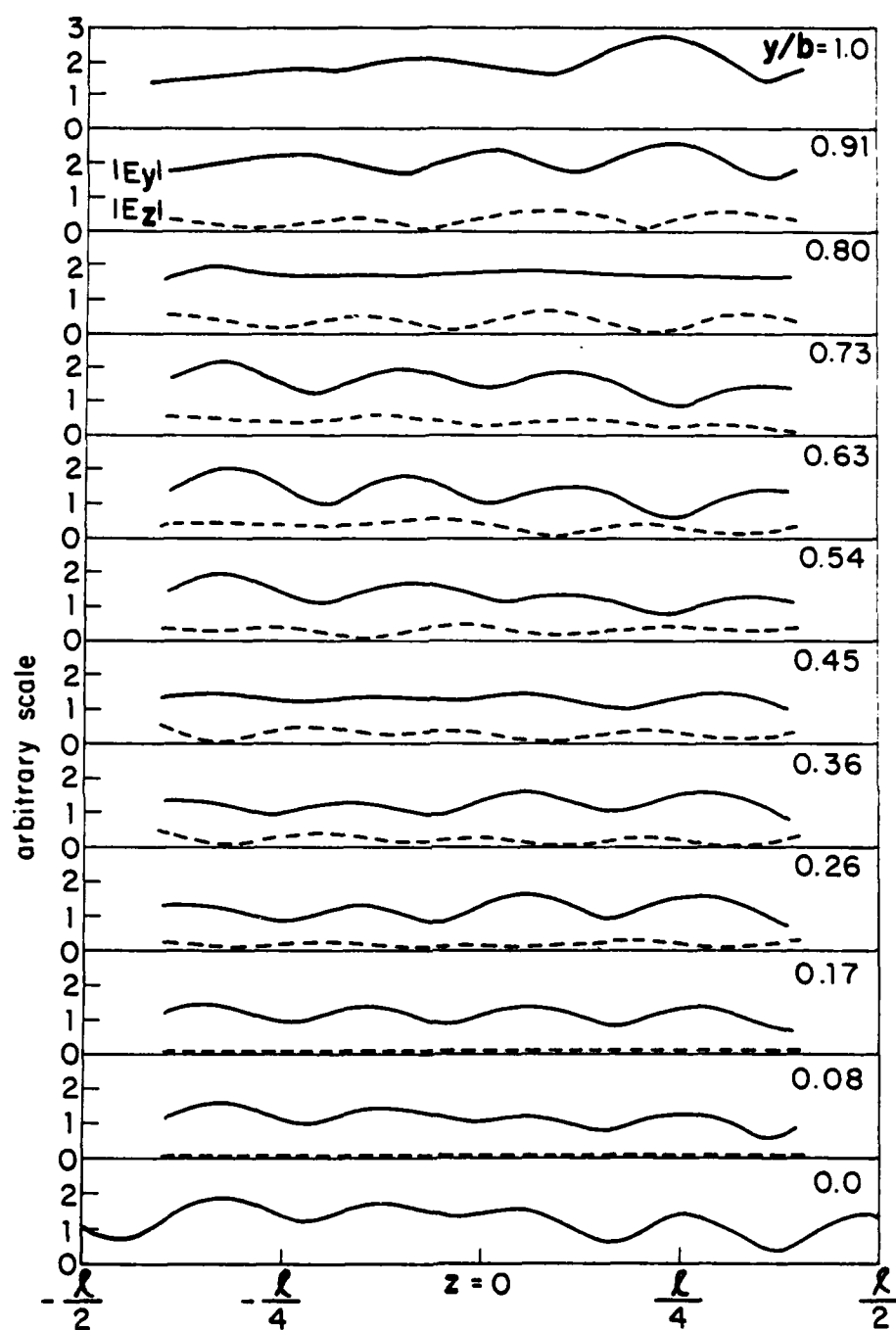


Figure 6.10. Distribution of standing waves in working volume for each mode; SWR = 1.36, $\lambda = 48$ cm



Longitudinal cross section of working volume y - z plane $x=1.7\text{ cm}$
 $l = 115\text{ cm} = 2.4\lambda$; $b = 108\text{ cm} = 2.25\lambda$

Figure 6.11. Measured magnitude of the vertical and longitudinal components of the electric field in the working volume

long tube parallel to the x-axis that moves laterally and vertically. The component E_y was measured with the dipole in the vertical position, the component E_z with the dipole in the horizontal position. Only the magnitudes $|E_y|$ and $|E_z|$ are shown in Figure 6.11. Actually, both magnitude and phase were measured. Furthermore, for each height y/b shown in Figure 6.11 except $y/b = 0$, the fields were measured at seven values of x covering one-half of the parallel plate region.

Extensive field measurements were made at $y/b = 0.08$, 0.45, and 0.91 as measured with the space probe and at $y/b = 1$ as measured by the monopole probe protruding from the top plate and have been reported in Wu, et al. [6.8] and Krook, et al. [6.9]. Of particular interest are the four graphs of $|E_y|$ shown in Figure 6.12. They reveal the striking change in the standing-wave pattern in the plane $x = 1.7$ cm from near the top ($y/b = 0.91$) to the near bottom ($y/b = 0.079$). Clearly there are three standing-wave maxima at the top, four at the bottom. Actually, the standing-wave pattern for $|E_y|$ at $y/b = 0.08$ near the ground plane and shown at the bottom in Figure 6.12 is a good approximation of the TEM field shown at the bottom of Figure 6.10. The successive maxima are quite uniformly spaced at $\lambda/2 \doteq 24$ cm and $E_z = 0$. On the other hand, the standing-wave pattern of $|E_y|$ at $y/b = 0.91$ near the top plate is quite different in that there are more nearly three instead of four standing half-wavelengths in the distance $-48 \text{ cm} \leq z \leq 48 \text{ cm}$. This is shown at the top in Figure 6.12. Thus, the measured graph at the top in Figure 6.12 resembles the graph at the top in Figure 6.10 for the standing-wave distribution of the $n = 3$ mode in the parallel-plate region. It is also evident from Figure 6.11 that E_z is significant. It has a standing-wave distribution with a wavelength near λ_{g3} and is displaced from that of $|E_y|$ by nearly $\lambda_{g3}/4$.

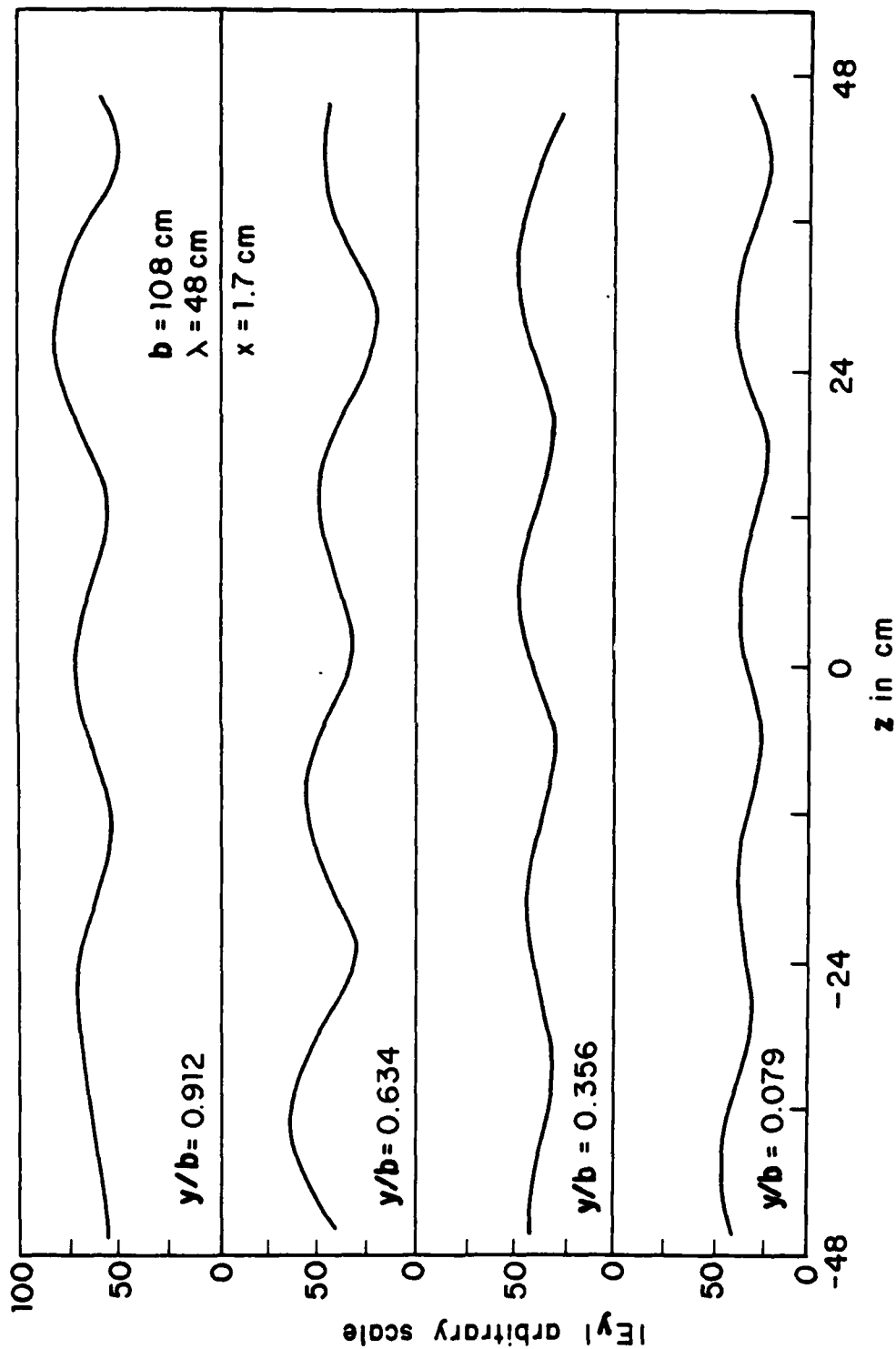


Figure 6.12. Measured $|E_y|$ near center ($x = 1.7$ cm) of working volume at four heights

In order to interpret the extensive data contained in the measured field in the working volume, the graphs shown in Figure 6.13 were constructed from the measured data. They show the measured $|E_y|$ as a function of the vertical coordinate y at seven different transverse positions x across the central plane ($z = 0$) of approximately one-half of the parallel plate region. The distributions are seen to be quite comparable in magnitude and shape, thus indicating a field that is reasonably independent of the transverse coordinate x , as is implicit for the ideal TEM and TM_{0n} components. The fact that E_y is approximately independent of x also indicates that the contribution to $|E_y|$ by possible TE_{0l} modes is small. This is considered in a later subsection.

At each cross section ($z = \text{constant}$), E_y can be approximated by a superposition of the TEM and the three propagating TM_{0n} modes. The relative amplitudes of these modes cannot be determined theoretically, but can be obtained from the measured distribution of E_y . This superposition of modes has been demonstrated in Figures 6.14a and 6.14b.

It is evident from these figures that the assumed approximate representation of the field as a superposition of the ideal parallel-plate TEM and TM_{0n} modes is a good one throughout the working volume of the model simulator. It is also evident that the total E_y differs greatly from the part contributed by the TEM mode alone, which is constant in y . Such a representation has also shown that the amplitudes of the TEM and TM_{01} modes are almost the same. Their standing-wave distributions and phases are such that $|E_y|$ is substantially greater near the top plate, $y = b$, than near the ground plane, $y = 0$.

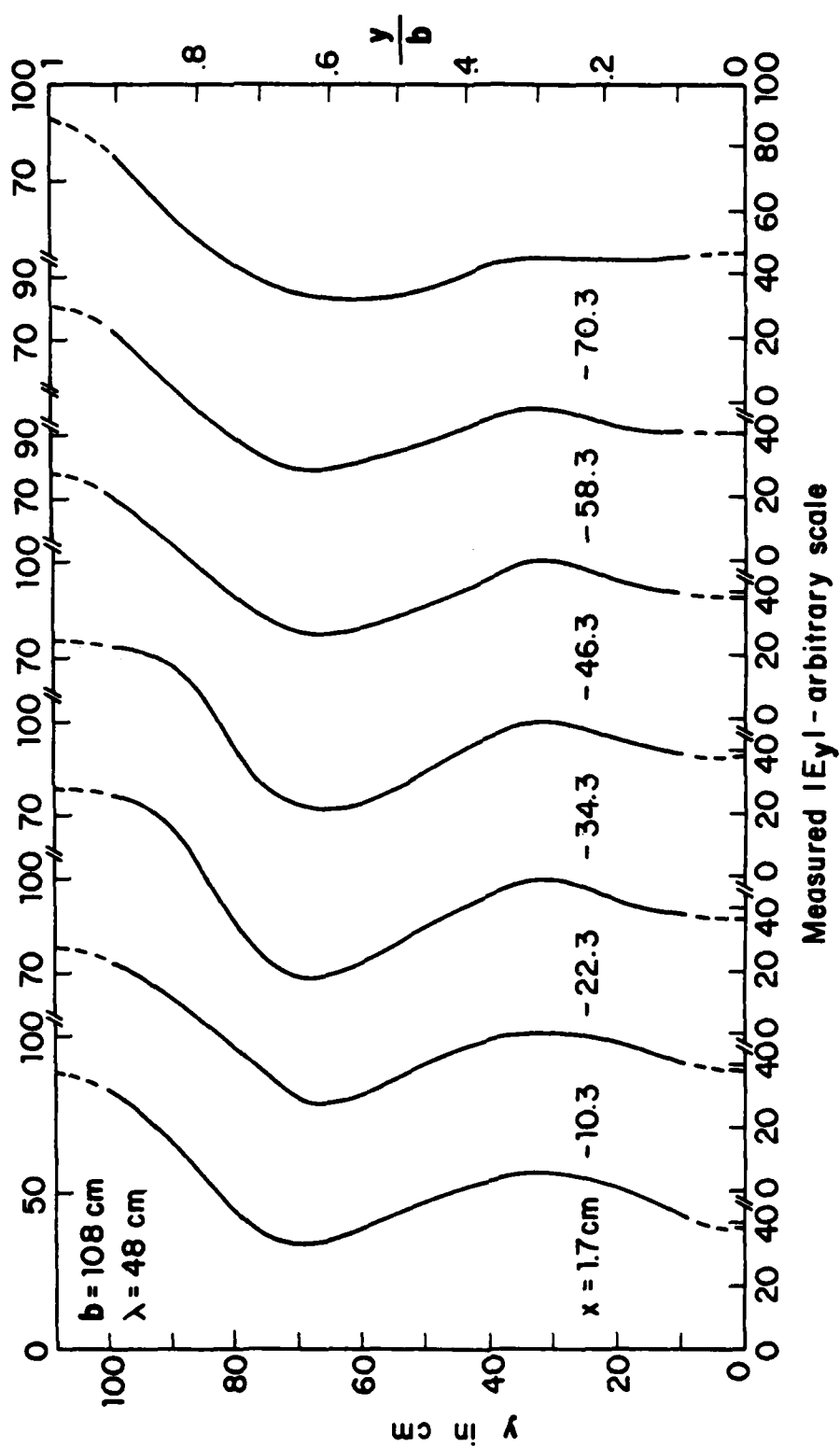


Figure 6.13. Measured electric field near central plane ($z = 0$) in parallel-plate region

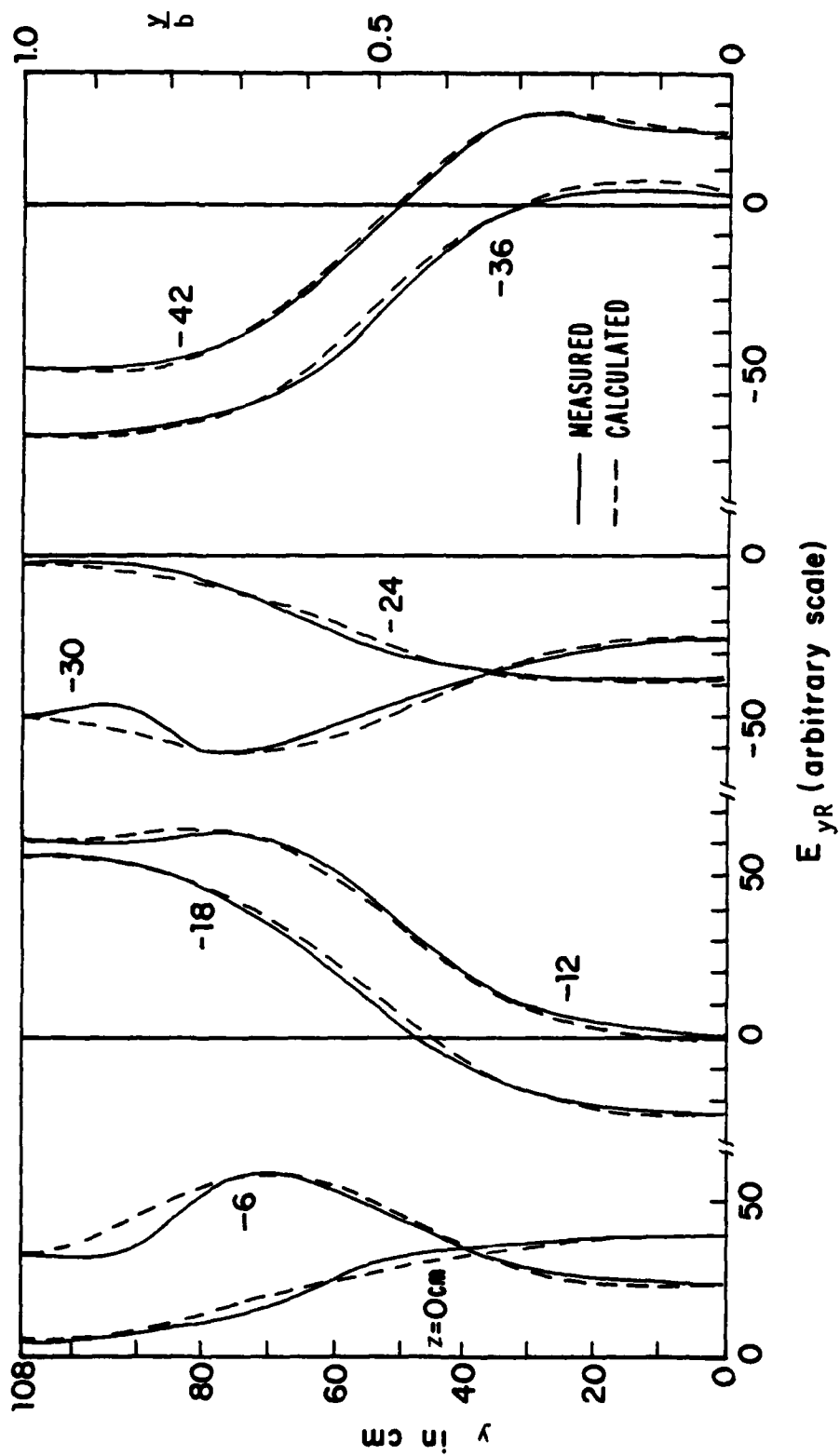


Figure 6.14a. Real part of vertical electric field in working volume. (Phase reference: $x = y = z = 0$)

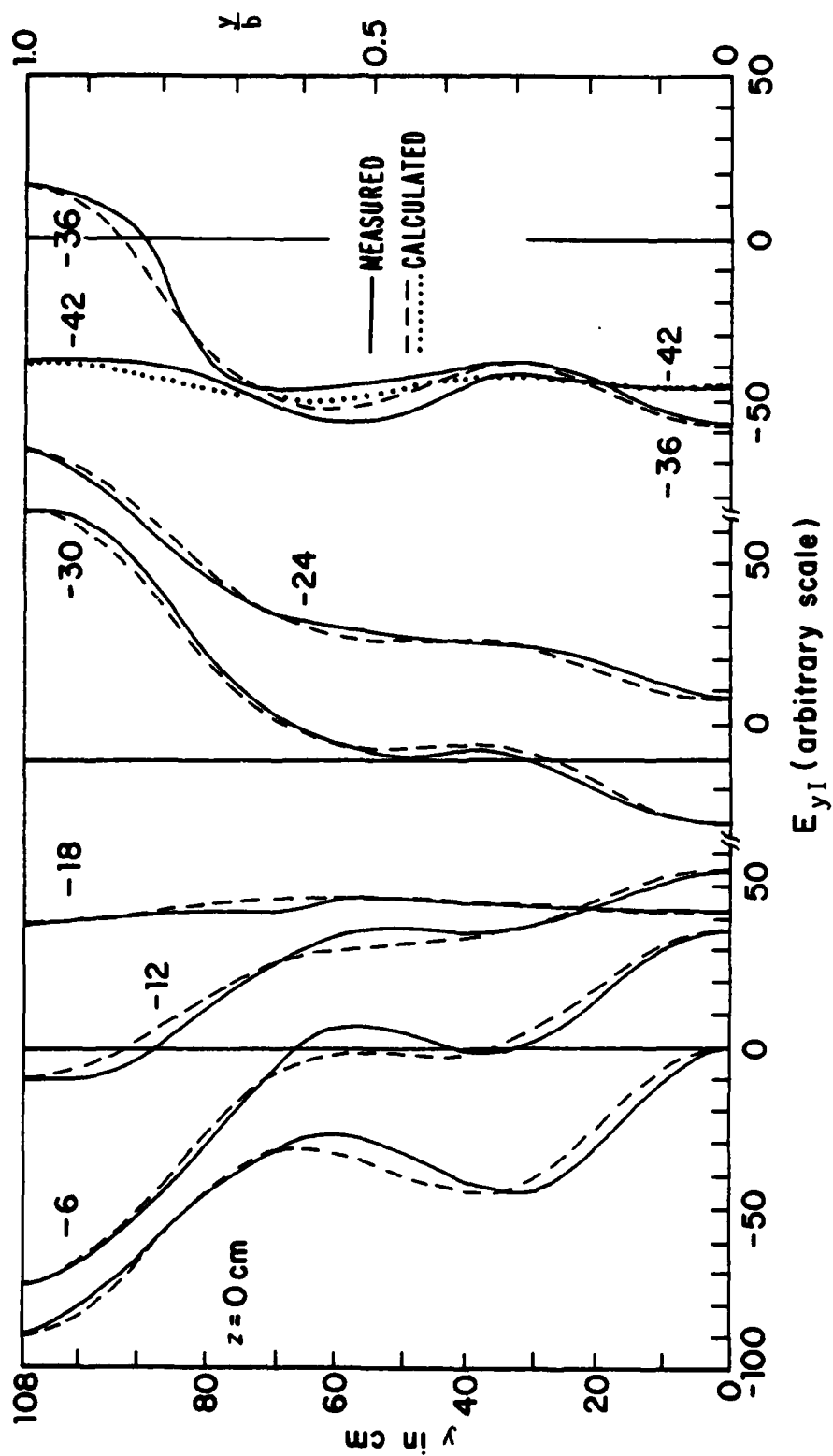


Figure 6.14b. Imaginary part of vertical electric field in working volume. (Phase reference: $x = y = z = 0$)

VI.7 The Measured Field in the Working Volume:

$$b = 0.66\lambda = 75 \text{ cm}; \quad f = 264 \text{ MHz}$$

The components E_y and E_z in the working volume and adjacent regions were also measured with $f = 264 \text{ MHz}$ when $b = 75 \text{ cm} = 0.66\lambda$ and $\lambda = 113.6 \text{ cm}$. To simplify the presentation of the data, these components of the field were measured as functions of y/b with $z = 0$ and x as parameter. The measured graphs of $|E_y|$, $|E_z|$, θ_y and θ_z are shown in Figure 6.15 for eight values of x .

As with the higher frequency and greater height b of the working volume, the approximate representation of E_y and E_z by TEM and TM_{0n} modes was found to be quite satisfactory. The difference is that at $f = 626.5 \text{ MHz}$, it took 3 TM modes, whereas at $f = 264 \text{ MHz}$ it took only the TM_{01} mode in addition to the TEM mode for adequate representation of measured fields.

VI.8 The Transverse Variation of the Electric Field; TE Modes

The approximate representation of the electric field in the parallel-plate region of the simulator in terms of the TEM and TM_{0n} modes tacitly assumes that all of the components of the electromagnetic field are independent of the transverse variable x since all wave fronts are assumed to be planes perpendicular to the longitudinal z -axis. This was taken to be a good approximation because the electric field shown in Figure 6.13 changes relatively little as x is varied in steps from near the center of the parallel plate region to near the edge at $x = \pm a = 87.5 \text{ cm}$. By examining the variation of the field with the x -coordinate in great detail, we have basically concluded that the contribution of TE_{0l} modes, if any, is negligible at both frequencies (626.5 MHz and 264 MHz) compared to the combined contribution of TEM and

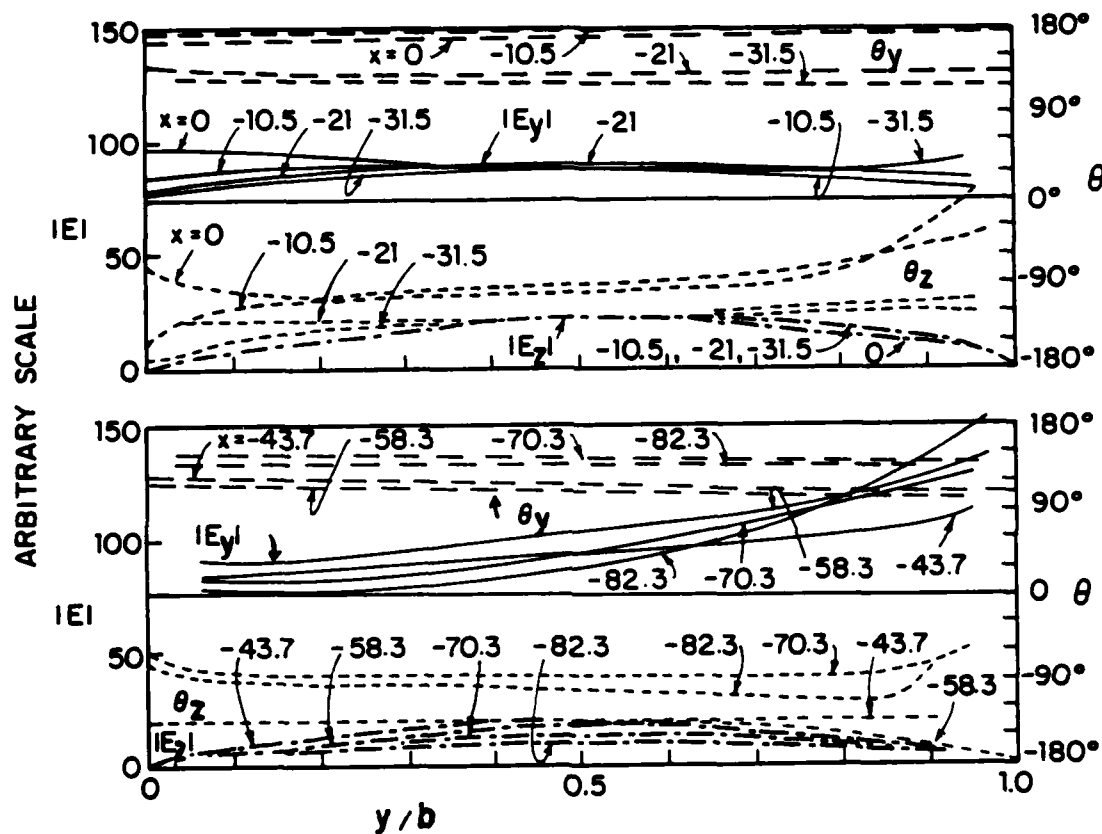


Figure 6.15. Measured electric field in transverse plane $z = 0$ of parallel-plate region; $\ell = 114.8$ cm, $2a = 175$ cm, $b = 75$ cm, $f = 264$ MHz

TM_{0n} modes. This conclusion was reached starting with the nature of the wavefronts or the surfaces of constant phase in the parallel plate region and recognizing this to be a traveling spherical wave with superimposed oscillations due to standing waves. The incident spherical wave can excite antisymmetric components of H_z and can potentially excite antisymmetric TE_{0l} modes. The amplitudes and wave members of TE_{0l} modes are known [6.3] for certain dimensions. From examining the data, it is reasonable to suppose that a superposition of TE_{0l} modes will account for the difference $E_y(x,y,z) - E_y(0,y,z)$ where $E_y(0,y,z)$ is the field represented by TEM and TM_{0n} modes, and to assume that the TE_{11} mode contributes negligibly. For the present purpose of this section, the representation of the electromagnetic field in terms of TEM and TM_{0n} modes is adequate without the addition of a sum of TE_{0l} modes, because it is experimentally verified that the departure of $E_y(x,y,z)$ from $E_y(0,y,z)$ is quite small--on the order of 8%--in the central part of the simulator.

VI.9 The Actual Electromagnetic Field in the Simulator as an Approximation of a Plane Wave

The electromagnetic field which is to be approximated in some volume of the simulator is a plane wave traveling in the positive z -direction with the components $E_y(z,t) = E_y(0)e^{i(kz-\omega t)}$, $H_x(z,t) = E_y(z,t)/\zeta_0$ where $\zeta_0 = (\mu_0/\epsilon_0)^{1/2} = 120\pi$ ohms. The field is independent of the transverse coordinates y and x , and is distributed as shown in the upper left of Figure 6.9 at the instant $t = 0$. As time passes, the entire pattern moves in the positive z -direction with the speed $c = 3 \times 10^8$ m/sec.

The actual field in the parallel-plate section of the simulator is a spherical wave originating at the driving-point on the ground plane and modified by superimposed reflections from the top plate. The field can be approximated by a sum of appropriate parallel-plate modes, but this is merely a change in the representation and not in the nature of the field. Moreover, all of the modes are generated by the incident field and not by reflection at load end.

As the cylindrical wave travels in the parallel-plate region, it experiences reflections at the edges $x = \pm a$ and at the end $z = l/2$. The former maintain the transverse standing waves, the latter the longitudinal standing waves like the one shown in Figure 6.11. They can be decomposed into separate standing waves of the TEM and TM_{0n} modes for the E_y and E_z components. Measurements were also made of the standing-wave pattern of the magnetic field over a wide range of frequencies centering on $f = 264$ MHz with $b = 75$ cm. Selected graphs at $f = 250, 264$, and 270 MHz are shown in Figure 6.16. It is seen that as the frequency is varied, the entire standing-wave pattern moves. Simultaneously, the standing-wave ratio fluctuates. Note in Figure 6.16 how the depth of the minimum varies as its location moves. If the loop probe is fixed at $z = 0.074l = 8.5$ cm, which locates the minimum for $f = 264$ MHz shown in the middle figure in Figure 6.16, and the frequency is then varied, the graph shown in Figure 6.17 is obtained. This shows a succession of minima that occur at $z = 0.074l$ at different frequencies, but with that at $f = 264$ MHz the deepest and sharpest. The maxima and minima in Figure 6.17 are a consequence of the standing waves generated in the working volume by reflections of the field at the ends $z = \pm l/2$ and the adjacent tapered sections. The standing-wave ratio varies somewhat with frequency so that the minimum amplitude at any fixed point increases and decreases with frequency. The

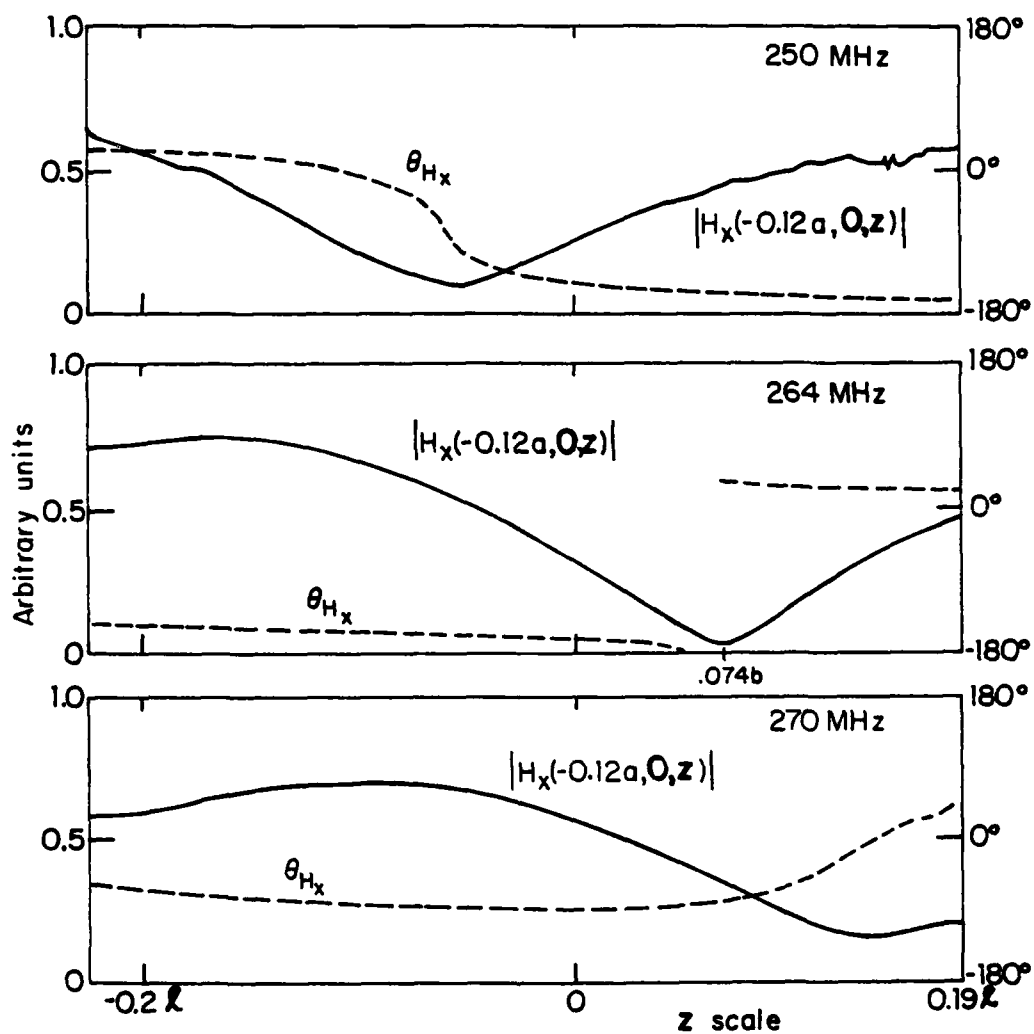


Figure 6.16. Measured magnitude and phase of the transverse component of the magnetic field on the ground plane in the working volume; width $2a = 175$ cm, length $l = 114.8$ cm, height $b = 75$ cm

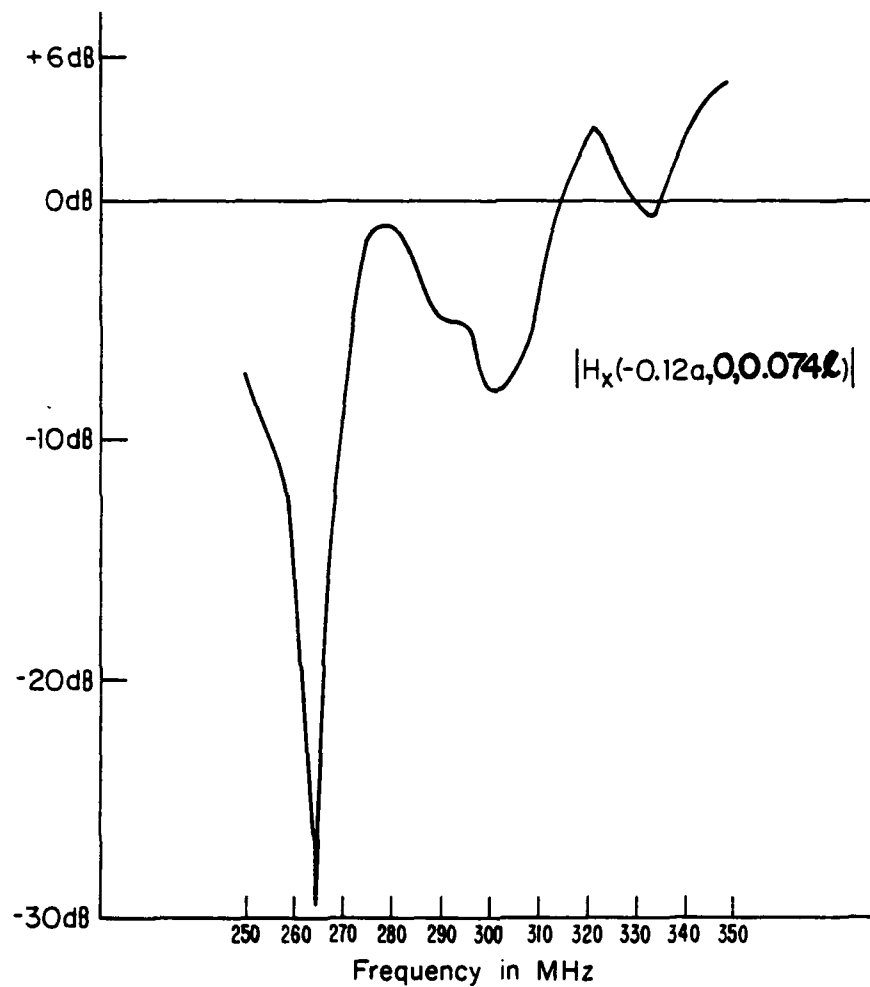


Figure 6.17. Measured magnitude of the transverse magnetic field at a fixed position in the working volume as a function of frequency; $2a = 175$ cm, $\ell = 114.8$ cm, $b = 75$ cm, $p_f = 40$ w

deepest minimum at $z = 8.5$ cm occurs at $f = 264$ MHz. At another location of the probe, the frequency for and the depth of the minimum will be different.

The differences between the actual electromagnetic field in the working volume of the model simulator and a traveling plane wave are significant when $b = 108$ cm $= 2.25\lambda$ with $f = 626.5$ MHz and considerably larger when $b = 75$ cm $= 0.66\lambda$ with $f = 264$ MHz. In the first place, the component E_y of the electric field is not uniform in either the transverse or vertical directions; second, there is a small component E_z ; and, third, there is a significant standing wave. It follows that the electrical environment of a metallic obstacle placed in the working volume is necessarily quite different from what it would be if it were exposed to an incident plane wave. Therefore, it must be expected that currents and charges induced on the surface of an obstacle may also be quite different. A detailed comparison of the distributions of induced currents and charges on obstacles when in the simulator and when exposed to a plane wave will be investigated in detail and reported at a later date. For purposes of comparison, theoretically determined distributions of Burton, et al. [6.10] are available. Although some sample set of measurements has been made of the very sensitive charge density distribution on the surface of a tubular cylinder located at the center of the parallel plate region, it is considered useful to postpone such comparisons until more extensive experimental data become available.

VI.10 Possible Methods to Improve the Field in the Simulator as an Approximation of a Traveling Plane Wave

The lateral and vertical nonuniformity of the field in the simulator on the one hand and the existence of standing waves on the other hand constitute the principal departures

from the desired traveling plane wave. Of these the first is a consequence of the spherical wave fronts that are incident on the parallel-plate section, the second is due to reflections at and beyond the junction of the parallel-plate region and the tapered section leading to the terminating impedance.

It might be supposed that the nonuniformity in the transverse distribution of the electric field is a problem only at high frequencies when modes other than the TEM can propagate in the parallel-plate section. The cut-off wavelength for the TM_{01} mode is $\lambda_{c1} = 2b$ so that at all wavelengths longer than $2b$ only the TEM mode can propagate. However, with the length l ($= 216$ cm or 150 cm) and, therefore, less than λ when this is greater than $2b$, even non-propagating modes may have significant amplitudes in the electrically rather short parallel-plate section. One way to reduce the transverse variation in E_y in the parallel-plate section is to provide an incident field that more nearly approximates a plane wave than does the actual spherical wave. With the geometry of the input structure predetermined, this is not readily accomplished. It involves a modification of the phase velocity of the spherical wave in the tapered section from the generator by some kind of a collimating lens or its equivalent in the form of metal plates or corrugations on the ground plane so that the spherical wave front becomes more nearly planar as it reaches the parallel-plate section.

The existence of standing waves in the parallel-plate section is a consequence of the fact that the entire structure has the characteristics of a terminated transmission line only at low frequencies for which the condition $2\pi b/\lambda \ll 1$ is satisfied. This condition underlies the theory of all open transmission lines, and requires that radiation be negligible in determining the characteristics of the line. When this condition is satisfied, it is possible to design the trans-

mission line so that virtually all of the power supplied by the generator is transmitted along the line to a matched load at the end. As the height b is increased, radiation becomes significant and, for sufficiently large values of b , dominant. The structure then acts like a traveling-wave antenna. Since the standing-wave ratio in the parallel-plate section is reasonably constant (see Figure 6.11), it is evident that the effective load on the open parallel-plate waveguide is at or beyond its junction with the sloping triangular plate at the load end. That is, most of the radiation takes place during reflection at or beyond the discontinuity formed by this sharp junction. (It is to be expected that radiation also takes place at the junction of the sloping triangular plate with the parallel plate at the generator end, but this does not affect the standing-wave ratio in the parallel-plate region.)

It was seen that the amplitudes of the TEM and TM_{01} modes are about equal and those of the TM_{02} and TM_{03} modes negligible when $b = 2.25\lambda = 108$ cm with $f = 626.5$ MHz. In this case, the standing-wave ratio as obtained from Figure 6.11 is less than 2. On the other hand, the amplitude of the TEM mode exceeds that of the TM_{01} mode when $b = 0.66\lambda = 75$ cm with $f = 264$ MHz and in this case the standing-wave ratio is about 3. It, thus, appears that the standing-wave ratio in the parallel-plate region can be reduced significantly only by reducing the reflection at $y \geq b/2$ of the entire component E_y on the electric field between the parallel plates. The selective reduction of the TM_{0n} modes by attenuating E_z , even if 100% successful, would not significantly reduce the standing-wave ratio when it is greatest, if the TEM wave is not properly terminated. There is no comparable way to attenuate separately the TE_{0l} modes since they have only an E_x component of the electric field. What is required to reduce the standing-wave ratio is more frequency-dependent termination for the parallel-plate section of the

simulator than is provided by the sloping triangular plate with its resistive termination, which is frequency independent only at sufficiently low frequencies. This is important primarily in the intermediate range of frequencies when b is of the order of a wavelength and the standing-wave ratio is higher. More work in optimizing the terminator is planned, and it is expected that a combination of a proper load and selective reduction of TM_{0n} modes will significantly minimize the reflection problem.

VII SIMULATOR/OBJECT INTERACTION

VII.1 Introduction

In designing new bounded wave EMP simulators, or in assessing the measured data obtained from existing simulators, it is important to determine to what extent the presence of the simulator structure affects the response of the test object. The usual objective of a simulation test is to evaluate the response of a system, say an aircraft, in the in-flight or ground-alert modes with no simulator facility present. This is usually not possible due to the need for providing high electromagnetic energy densities in the vicinity of the test object. This requirement generally leads to locating the simulator structure close to the system being tested thereby increasing the degree of simulator/object interaction. For the in-flight mode of testing, in addition to the conductors, dielectrics, wires, etc., that make up the simulator, the nearby ground should also be electromagnetically invisible during the time when the test object is responding. In this sense, the ground effects can also be categorized under simulator/object interaction.

Although bounded wave simulators are constructed with conducting parallel plates (approximated by wire meshes in practice) having a finite width, the analysis of the behavior of objects within the simulator is usually simplified by considering an infinite parallel-plate region containing the object. Thus the simulator/object interaction problem is reduced to that shown in Figure 7.1, where a doubly infinite set of images may be introduced to account for the presence of the parallel plates. The answer to the question of how the response (probably both in time and frequency domains) of the aircraft in Figure 7.1 differs from that of the aircraft in free space then serves to quantify the degree of simulator/object interaction.

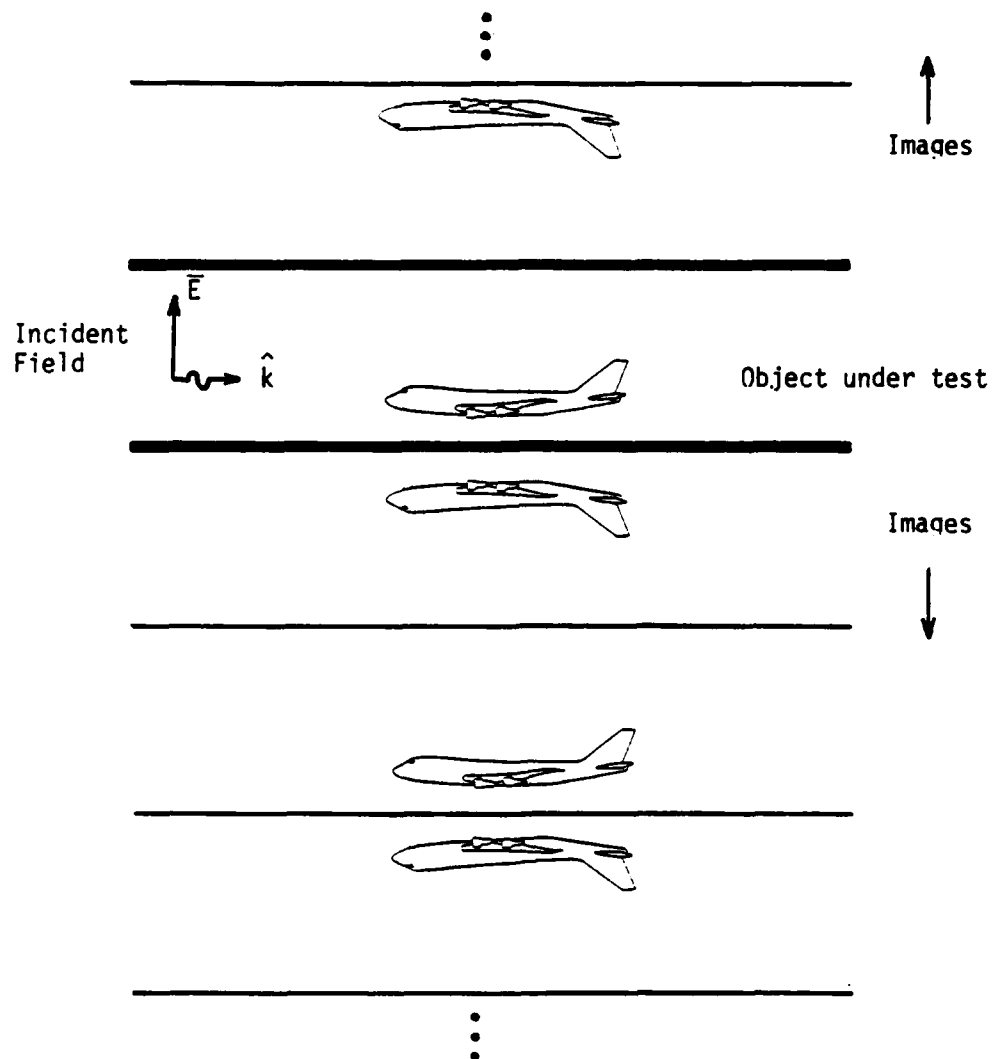


Figure 7.1. Object under test and images in parallel plate EMP simulator

A number of studies have been performed in an attempt to describe simulator/object interaction. Since it is difficult to compute the response of an actual aircraft in free space (not to mention the case of an aircraft in the parallel-plate region), investigators have been forced to consider relatively simple objects, such as cylinders and spheres, for their studies. Numerous data are available for these special cases, but nevertheless, there appear to be a few formalized conclusions that may be drawn from the past work. This is due principally to the fact that there is no single quantity which adequately describes all aspects of object/simulator interaction.

VII.2 SEM Representation

Past studies have dealt with currents at various points on the object and charge densities (or charge enhancement factors) in both the time and frequency domains, as a function of the many geometrical parameters describing the problem. These studies are documented in references [7.1 to 7.9]. In an attempt to obtain a relatively simple set of quantities to describe the interaction, the concepts of the singularity expansion method (SEM) have been applied in reference [7.10] and, more recently, in reference [7.11]. In the SEM representation, the total current at a point ξ on a thin cylinder within the parallel-plate region can be expressed as

$$\tilde{I}(\xi; s) = \sum_{\alpha} \left[\frac{R_{\alpha}(\xi)}{(s - s_{\alpha})} + \frac{\bar{R}_{\alpha}(\xi)}{(s - \bar{s}_{\alpha})} \right] + \tilde{I}_R(\xi, s) \quad (7.1)$$

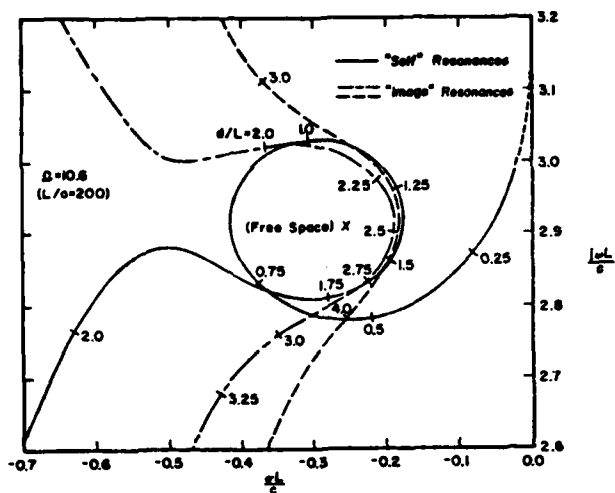
where s represents the complex frequency, s_{α} are the complex natural resonances of the wire, $R_{\alpha}(\xi)$ is the residue or pole strength at the α^{th} resonance, and $\tilde{I}_R(\xi, s)$ is a remainder term which arises from both the incident waveform singularities and the branch cut integrals which arise in the parallel plate region [7.11]. The bar over a quantity

as in \bar{s}_α) denotes the complex conjugate of the quantity. The second term in the summation with complex conjugate quantities is required so that the time domain response $I(\xi;t)$ will be a real function of time.

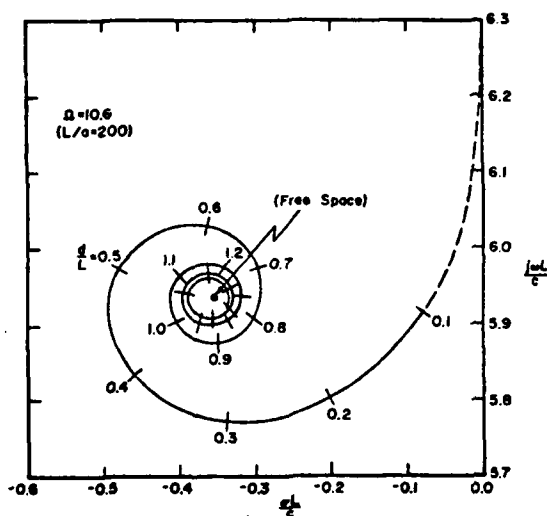
In studies to date, attention is focused on the natural resonances, s_α , and how they vary with changes in the simulator/object geometry. Early studies involved removing one plate of the simulator and examining the trajectories of the resonances in the complex frequency plane. Figure 7.2, taken from reference [7.12], shows the trajectories of the first two resonances of a thin cylinder of length L and radius a , which is parallel to the bottom plate, as a function of height, d , of the cylinder. As is noted, substantial variations of the damping constants are obtained for the first natural frequency. For this particular example, the length to radius ratio was $L/a = 200$.

Similar data for the first resonance have been presented in reference [7.9] for the same thin wire at various inclination angles, β . Note that $\beta = 0^\circ$ implies that the wire is parallel to the ground plane, and $\beta = 90^\circ$ is for the wire perpendicular to the ground. Figure 7.3 shows the percent change of the first resonant frequency relative to the free space value, as a function of the height of the wire (measured from the wire midpoint) above the ground. Figure 7.4 shows the corresponding variation of the damping constant. Although these data are in a slightly different form than the trajectories of Figure 7.2, they contain essentially the same kind of information regarding the simulator/object interaction.

The removal of the top plate of the simulator causes a significant simplification in the numerical treatment of simulator/object interaction studies. It removes, however, an important feature of the problem: that of branch points within the complex frequency solution for the body response.



(a)



(b)

Figure 7.2. Trajectories of the first (a) and second (b) natural resonances of a thin wire of length L and radius $a = L/200$, as a function of the height of the wire, d , over a conducting ground. (The wire is parallel to the ground, and this figure is reproduced from [7.12].)

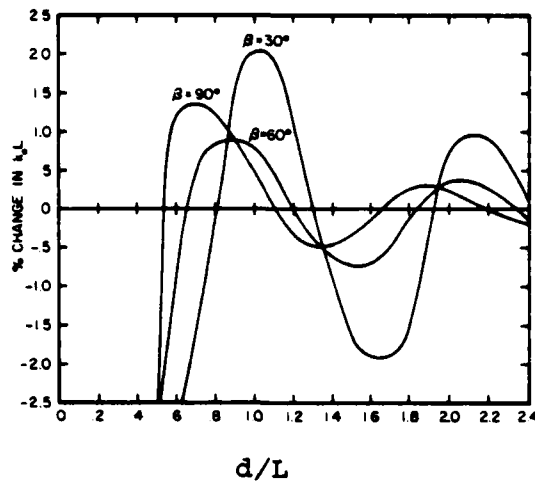


Figure 7.3. Plots of percent changes of first resonant frequency of wire object relative to free-space resonant frequency, shown as function of d/L for various inclination angles

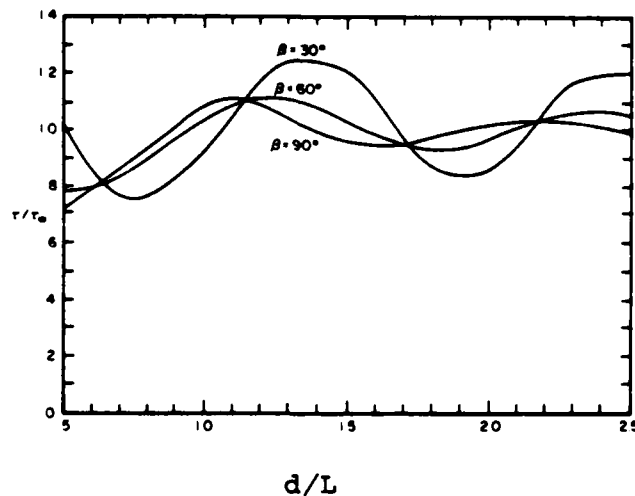


Figure 7.4. Plots of normalized damping constant τ/τ_∞ for fundamental resonance, shown as a function of d/L for various inclination angles. The quantity τ_∞ is the free-space damping constant

In reference [7.5], a study of the thin-wire object within the parallel-plate region was reported. Although other authors had considered similar problems [7.2 and 7.3], this report [7.5] was the first to consider the cylindrical object to be of an arbitrary angle within the simulator. Figure 7.5 shows the input conductance of a center-fed cylindrical antenna as a function of plate separation, d , and for various angles of inclination, θ . The discontinuities in these curves at certain plate separations are due to the presence of the branch points in the s -plane. For the thin wire perpendicular to the plates, ($\theta = 90^\circ$), note that these discontinuities vanish, suggesting that the branch point contributions become small or, perhaps, vanish. Similar discontinuities have been noted for scattering problems within parallel plates.

In an attempt to understand the behavior of thin cylinder objects within a parallel-plate simulator from an SEM view, reference [7.11] presents a study of the locations of the natural resonances for wires of varying aspect ratio (a/L) and for three different heights above the bottom plane. In obtaining these results, an integro-differential equation is derived, but it is only solved approximately so that it is difficult to assess the accuracy of the solution. Moreover, it does not give insight into the degree of importance of the branch point contribution to the solution. It does provide, however, a first step at applying SEM concepts to this interaction problem. The results reported in [7.11] are briefly summarized in the following Tables numbered 4.1, 4.2 and 4.3. In these tables, the pole locations in the complex s -plane for the three cases of $L/d = 0.2, 0.5$ and 0.8 are presented. It is noted that the cylinder is located symmetrically in the parallel plate region with its axis normal to the plates.

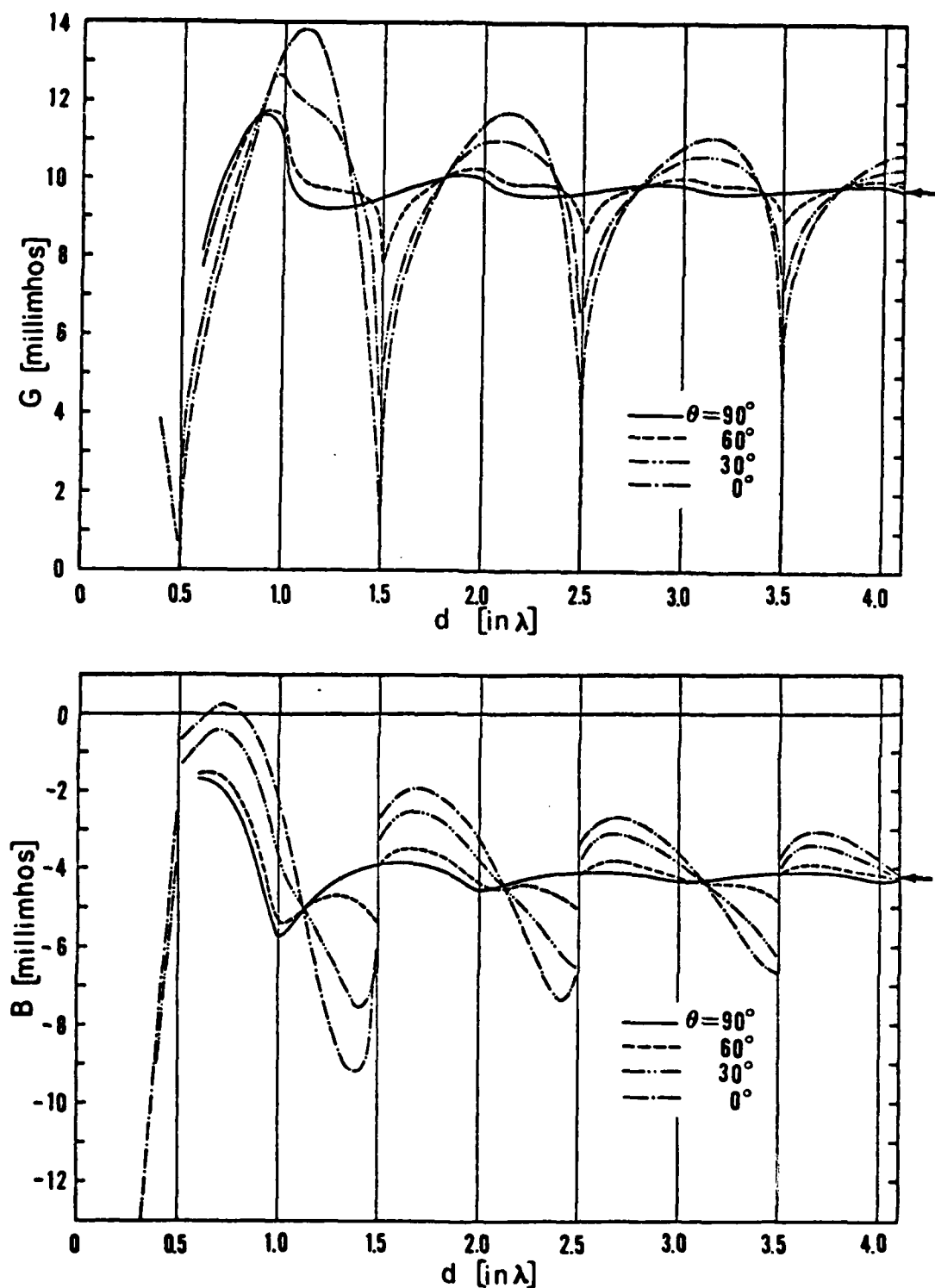


Figure 7.5. Input conductance (top) and susceptance (bottom) of a center driven antenna ($L=\lambda/2$, $\Omega=2 \ln (2L/a) = 10$) located at a distance $h = d/2$ from the bottom plate of a parallel-plate region of separation d . The arrows indicate the free-space values

TABLE 4.1
POLE SINGULARITY PARAMETERS FOR $L/d = 0.2$

m	$\frac{a}{L}$	$\frac{s'L}{m\pi c}$	$\frac{s''L}{m\pi c}$
1	0.003	-0.085	0.935
	0.01	-0.114	0.927
	0.03	-0.162	0.917
	0.1	-0.290	0.918
2	0.003	-0.117	1.91
	0.01	-0.160	1.91
	0.03	-0.238	1.91
	0.1	-0.460	1.98
3	0.003	-0.138	2.90
	0.01	-0.192	2.90
	0.03	-0.293	2.91
	.1	-0.578	3.09
4	0.003	-0.154	3.89
	0.01	-0.217	3.89
	0.03	-0.337	3.92
	0.1	-0.647	4.22
5	0.003	-0.167	4.88
	0.01	-0.238	4.89
	0.03	-0.374	4.94
	0.1	-0.674	5.33
6	0.003	-0.179	5.88
	0.01	-0.257	5.89
	0.03	-0.406	5.95
	0.1	-0.671	6.42

TABLE 4.2

POLE SINGULARITY PARAMETERS FOR $L/d = 0.5003$

m	$\frac{a}{L}$	$\frac{s^1 L}{m \pi c}$	$\frac{s'' L}{m \pi c}$
1	0.003	-0.052	0.952
	0.01	-0.064	0.950
	0.03	-0.081	0.950
	0.1	-0.109	0.963
2	0.003	-0.126	1.94
	0.01	-0.174	1.93
	0.03	-0.266	1.91
	0.1	-0.557	1.99
3	0.003	-0.094	2.90
	0.01	-0.119	2.91
	0.03	-0.155	2.93
	0.1	-0.186	3.03
4	0.003	-0.165	3.93
	0.01	-0.236	3.92
	0.03	-0.379	3.93
	0.1	-0.848	4.27
5	0.003	-0.117	4.88
	0.01	-0.152	4.90
	0.03	-0.199	4.95
	0.1	-0.176	5.10
6	0.003	-0.191	5.92
	0.01	-0.280	5.92
	0.03	-0.458	5.97
	0.1	-0.976	6.61

TABLE 4.3

POLE SINGULARITY PARAMETERS FOR $L/d = 0.8003$

m	$\frac{a}{L}$	$\frac{s'_m L}{\pi c}$	$\frac{s''_m L}{\pi c}$
1	0.003	-0.114	0.956
	0.01	-0.154	0.947
	0.03	-0.226	0.936
	0.1	-0.431	0.952
2	0.003	-0.128	1.97
	0.01	-0.177	1.97
	0.03	-0.266	1.99
	0.1	-0.504	2.15
3	0.003	-0.110	2.97
	0.01	-0.151	2.98
	0.03	-0.220	3.01
	0.1	-0.327	3.21
4	0.003	-0.061	3.95
	0.01	-0.075	3.96
	0.03	-0.090	3.98
	0.1	-0.065	4.04
5	0.003	-0.129	4.88
	0.01	-0.180	4.87
	0.03	-0.270	4.88
	0.1	-0.447	5.02
6	0.003	-0.182	5.86
	0.01	-0.265	5.85
	0.03	-0.435	5.86
	0.1	-1.25	6.22

Comparisons of the pole trajectories of cylinders in the parallel plate region with those of isolated cylinders, as well as comparisons of time domain responses, should be pursued in future efforts.

VII.3 Fields Near the Test Object

Another approach in understanding how an object interacts with the simulator is to investigate the behavior of the electric fields in the vicinity of the test object. These fields generally have four components, 1) fields produced by currents flowing on the test object, 2) fields produced by currents flowing on the parallel plates (i.e., the image currents), 3) the incident field, and 4) reflections of the incident field within the parallel-plate region. The fourth field component is often neglected, since pure TEM excitation is assumed. Concentrating on the first two field components, it is noted that their behavior depends not only on the overall body geometry, but also on the simulator geometry. For the thin wire of length L , analyzed in reference [7.5], an integral relation for the scattered electric field at a point $\bar{\xi}$ is given by

$$j\omega\epsilon \bar{\xi}' \cdot \bar{E}^{inc}(\bar{\xi}) = \int_0^L I(\bar{\xi}') \left[K_{fs}(\bar{\xi}, \bar{\xi}'; \omega) + K_{pp}(\bar{\xi}, \bar{\xi}'; \omega) \right] d\bar{\xi}' \quad (7.2)$$

where $\bar{E}^{inc}(\bar{\xi})$ is the incident TEM field, $I(\bar{\xi}')$ is the induced wire current, K_{fs} is a free-space kernel and K_{pp} is the additional contribution to the kernel which takes into account the presence of the parallel plates. This relation may be used to derive an integral equation for the wire current. A study of the variation of the K_{pp} term relative to K_{fs} will thus permit some insight into the interaction problem.

In order to assess the relative importance of these terms, it is possible to study the magnitude of the ratio K_{pp}/K_{fs} as a function of the height of the scatterer above the bottom plate with all other variables taken to be constant. This is equivalent to investigating the primary and image components of the electric field which are parallel to the wire at a position ξ , due to an infinitesimal current element at a position ξ' . To minimize the complexity of this problem, we consider both ξ and ξ' to be located at the midpoint of the wire, i.e., at $L/2$, and the wire to be inclined with an angle $\theta = 90^\circ$, which provides for maximum interaction with the ground plane. Figure 7.6 shows the geometry of this case. From [7.5], the free-space kernel has the value

$$K_{fs}(L/2, L/2; \omega) = \left(\frac{\partial^2}{\partial \xi^2} + k^2 \right) \frac{e^{-jk[(\xi - \xi')^2 + a^2]^{1/2}}}{4\pi[(\xi - \xi')^2 + a^2]^{1/2}} \Big|_{\xi = \xi' = L/2} \quad (7.3)$$

where a is the radius of the wire and $k = \omega/c$. The portion of the kernel due to the parallel plates is given by

$$K_{pp}(L/2, L/2; \omega) = - \left(\frac{\partial}{\partial \xi'} \frac{\partial}{\partial \xi} + k^2 \cos(2\theta) \right) \sum_{n=-\infty}^{\infty} \frac{e^{-jkR_n^{(1)}}}{4\pi R_n^{(1)}} + \left(\frac{\partial^2}{\partial \xi^2} + k^2 \right) \sum_{\substack{n=-\infty \\ n \neq 0}}^{\infty} \frac{e^{-jkR_n^{(2)}}}{4\pi R_n^{(2)}} \Big|_{\xi = \xi' = L/2} \quad (7.4)$$

where

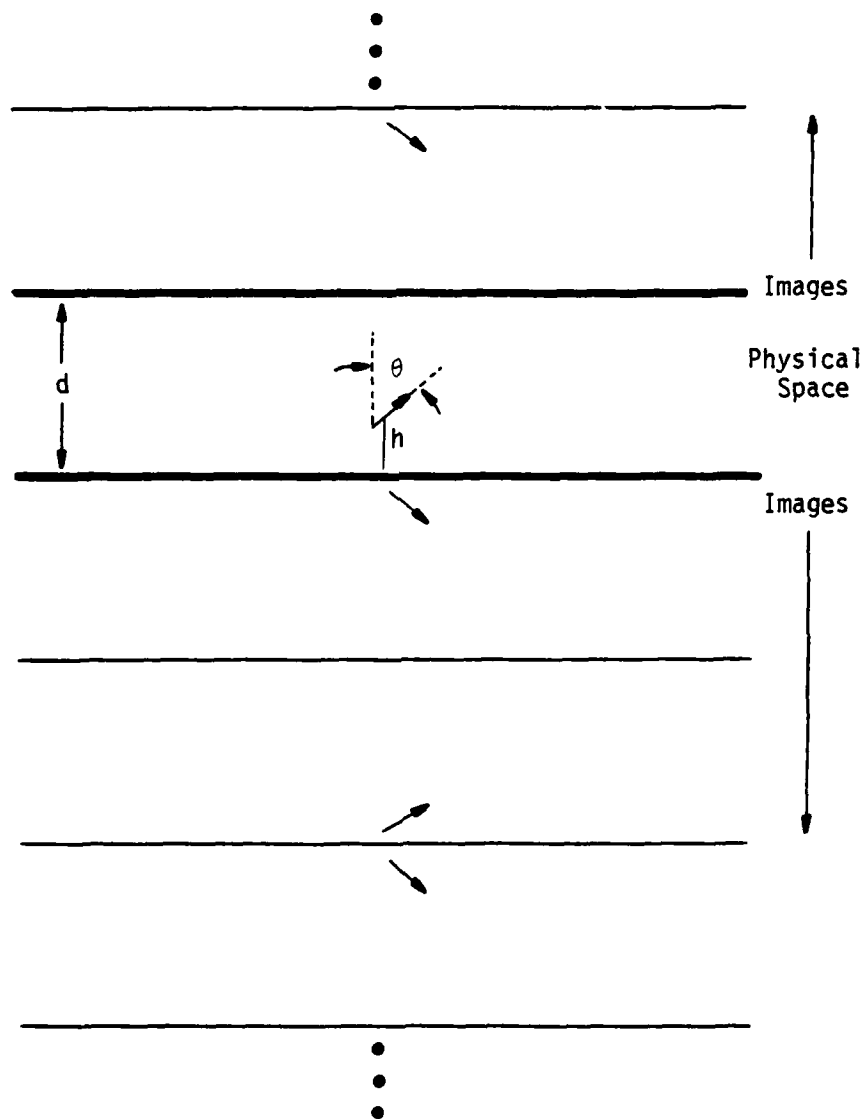


Figure 7.6. Infinitesimal current element within parallel-plate region

$$R_n^{(1)} = [((L-\xi-\xi') \sin\theta - 2(h+nd))^2 + (\xi-\xi')\cos\theta]^{\frac{1}{2}} \quad (7.5)$$

$$R_n^{(2)} = [((\xi-\xi')\sin\theta - 2nd)^2 + ((\xi-\xi')\cos\theta)^2]^{\frac{1}{2}} \quad (7.6)$$

and d is the plate separation and h is the height of the source point above the bottom plate.

A careful examination of the self-kernel in equation (7.3) shows that there is a $(ka)^3$ dependence which tends to mask the effects of the parallel plates. Thus, it is advisable to plot the quantity $(K_{pp}/K_{fs})/(ka)^3$.

Figure 7.7 shows this quantity as a function of kd for various values of source height. The effects of the resonances introduced by the parallel-plate geometry are clearly illustrated at $kd = \pi, 2\pi$, etc.

Unfortunately, this measure of object/simulator interaction depends on a parameter of the object, namely a , the radius of the wire. It would be possible to plot only the term $|K_{pp}|$ which is independent of a , but its value relative to $|K_{fs}|$ is what is important in equation (7.2) in determining the effects of the interaction. Thus, in performing a study of this sort, it is important to have a knowledge of the size of the object, as well as the dimensions of the parallel-plate region.

In summarizing the past work in this area, it is found that there is no one scalar parameter which can be used to describe simulator/object interaction. Given existing analytical and numerical methods, it is possible to analyze a few specific obstacles within a parallel-plate region, but it is difficult to then cast these numerical results into design curves which would be useful to engineers. The SEM

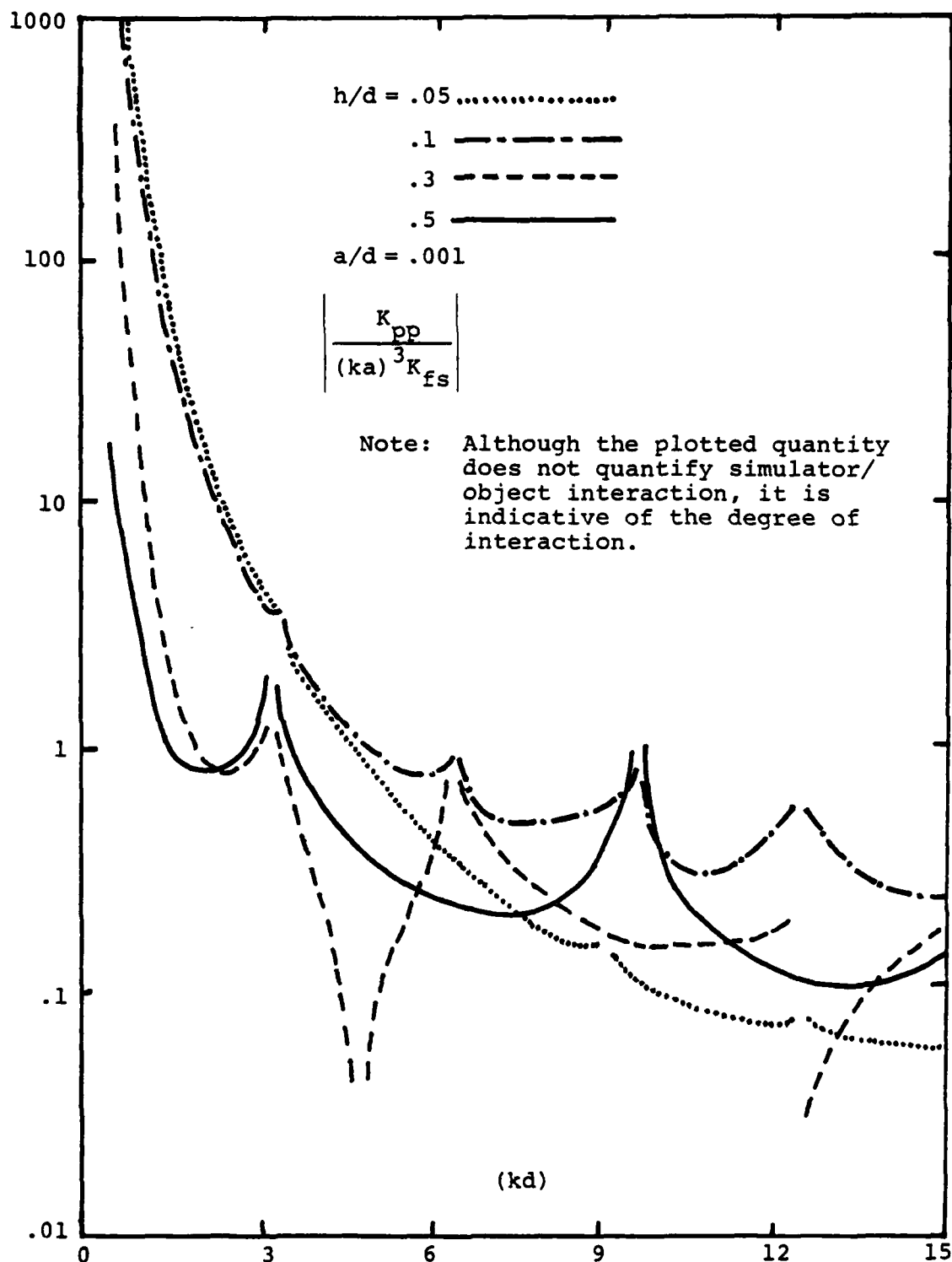


Figure 7.7. Plot of the normalized ratio of kernels for an infinitesimal current element at $\theta = 90^\circ$ (parallel to plates) and at a height h , as a function of plate separation

concepts, which have been used to explore the shift of the natural resonances of an obstacle, should be extended to investigate the effects of the branch points, which give rise to the discontinuities shown in Figure 7.7. Also, it is suggested that studies in the variations of the residues of the natural resonances be made to further understand the interaction problem. Finally, it would be useful to consider more realistic bodies within the simulator, say, a crossed-wire aircraft model.

VIII SIMULATOR AS A WHOLE

Because of the complexities in analyzing or evaluating the performance of the simulator as a whole, emphasis in the past has been rightfully placed on the individual components of the simulator. However, it is imperative that the understanding of various components of the simulator be hybridized wherever necessary, so that one can arrive at some meaningful conclusions, with regard to the simulator performance as a whole. A good example of the need for such confluence of understanding of individual simulator components lies in the junction of the conical and cylindrical (two-parallel plate) transmission lines. We have a detailed knowledge of the spherical TEM wave characteristics in the conical plate region [Section III] and the TE, TM and TEM wave characteristics in the parallel-plate region [Section IV]. But, at the junction of these two transmission lines, the fields can be quite complex due to reflections caused by field mismatches even though the impedance of the principal TEM modes in the two regions may be matched within a few percent.

Based on the considerations similar to the above example, it may be argued that while viewing the simulator as a whole we are confronted with the problem of assuring smooth electromagnetic transitions between various components, and, also between the various stages within a component (e.g., monocone switch and Marx column in the pulser).

Many examples of problem areas in this regard were identified by Baum, Giri and Chen [8.1] who updated a similar list in an earlier memo by Baum [8.2]. In what follows, we shall list and briefly discuss these problems, while pointing out some of their salient features.

VIII.1 Problems List

1. Characterization of the pulser and improvements in its matching with the simulator,
2. Evaluation of the TEM mode coupling coefficient for conical-cylindrical transition in frequency and time domains,
3. Analysis of TEM and higher order modes in non-flat plate geometries, e.g., circular arcs,
4. Accurate calculation of the earth effects on existing simulators,
5. GTD analysis of the simulator as a whole,
6. Determination of the properties of wire grid which make up the simulator plates for various unit cell geometries,
7. Higher order mode calculations in the conical plate region,
8. Appropriate modifications of the wave launcher and receptor for analysis purposes, consistent with problem (3) above,
9. Analysis and evaluation of both sloped and perpendicular distributed terminators for the case of finitely wide plates,
10. Determination of the properties (attenuation, phase shift, etc.) of the periodic array of dielectric rods, metal bolts and rings in the trestle,
11. Determination of simulator distant fields at low and high frequencies.

VIII.2 Brief Discussion of Salient Features of Listed Problems

1. Matching of pulser to the simulator

It is fair to state that the pulse power has not yet received sufficient attention from an electromagnetic point of view [8.3]. Some of the problems here are: a) impedance and field matching of the monocone switch geometry with the Marx and peaker assembly, b) minimizing dispersion times [8.4] at the Marx-simulator plate interface. Work is in progress in this area which looks at the Marx type of pulser as an EM boundary value problem by modeling the central Marx column along with the peakers as coupled transmission lines.

2. TEM coupling coefficients

The spherical TEM wave fields in the conical region, are well known in the spherical coordinate system which is a natural coordinate system for this geometry. From these studies, the rectangular components in a transverse plane at the conical-cylindrical junction can be evaluated. These fields can be thought of as "input" to the parallel plate region. By matching the fields from the conical region to those of the parallel plate region at the junction, the TEM coupling coefficients can be evaluated.

3. Nonflat geometries

For future generation simulators, it is desirable to explore other top plate geometries, e.g., curved (inwards [8.5] and outwards) in terms of the propagating modal (TEM, TE, and TM) distributions, impedances, etc. An important criterion here is the confinement of energy in the working volume, coupled with suitable modifications in the wave launcher and receptor sections.

4. Earth effects

Earth moving and sloping techniques have been used in the simulator facilities to reduce the adverse earth effects. For example, at frequencies above 5 MHz in ATLAS I (TRESTLE), the earth effects are not so significant; but below 5 MHz, more accurate calculation and experimental validation of such effects for various samples of Albuquerque soils are useful.

5. GTD analysis

At sufficiently low frequencies, quasi-static considerations apply and the evaluation of working volume fields are relatively straightforward. At the other end of the frequency spectrum, where critical dimensions of the simulator become several wavelengths, ray-optic techniques become applicable and hence a complete GTD analysis is desirable. The chief goal of such studies would be the prediction of working volume fields.

6. Wire grids

Although the simulator plates are in practice made of wire meshes, analyses and laboratory model studies have always employed solid plates with zero surface impedances. If one neglects ohmic losses, the wire-mesh plates have reactive surface impedance. The effects of this on wave propagation in conical and parallel plate regions need further investigation.

7. Non-TEM modes in conical transmission lines

We have extensive data from recent efforts at Dikewood Industries on the properties of TE and TM modes in

parallel plate regions which are summarized in Section IV. A similar analysis of the conical plate transmission line will significantly enhance our understanding of the simulator performance. The conical transmission line is a radial transmission line and classical methods of determining the non-TEM modal distributions should be explored.

8. Wave launcher/receptor

If nonflat top plate geometries are considered for analysis purposes, it is imperative to modify the wave launcher and receptor sections. Such modifications need to be addressed with the view of ensuring smooth transitions for wave transport, at all junctions.

9. Distributed terminators

Lumped resistive terminators with their inherent intrinsic reactances have been traditionally employed and experimentally evaluated [5.6]. Furthermore, the desirability and implications of perpendicular and sloped distributed terminators [5.4 and 5.5] were considered in Section V on terminators. However, the available calculations are for the case of infinitely wide plates, and the case of the finite width is considered a logical and useful extension of existing results.

10. Trestle effects

References [8.6, 8.7 and 8.8] consider the problem of scattering of a plane wave incident on a two dimensional periodic array of infinitely long dielectric posts. The conclusion there was that the support structure reflects little energy in the low frequency limit, but reflections are non-negligible when lengths of wood arrays become comparable to

wavelength. Additional complexities are introduced by metal on the trestle [8.9]. More work is desirable in this area by considering semi-infinite and finite vertical arrays of posts including horizontal and diagonal cross members. The platform or the trestle top affects the wave propagation and they can be evaluated at least initially, on laboratory model parallel plate simulators.

11. Distant fields

Some crude results are currently available [8.10 and 8.11] in estimating the distant fields from this class of EMP simulators. Reference [8.10] starts with the estimated working volume fields and computes distant fields via considerations of $(1/r)$ fall off, reflection and surface wave losses. Also, at low frequencies [8.11] one can estimate the distant fields by first estimating the equivalent electric and magnetic dipole moments of transmission lines formed by simulator plates. In contrast with high frequency distant fields, it was found that at low frequencies the maximum radiation occurs in a direction opposite to the direction of propagation in the simulator. The available approximate results indicate that more detailed studies for a wide range of frequencies are desirable.

REFERENCES

Most references cited in this report are from the AFWL EMP Notes and Memos series edited by Dr. C.E. Baum. They have been identified simply as "Sensor and Simulation Note XXX" or "ATLAS Memo XX," for convenience. While copies of the "memos" can be obtained from the author(s) or the editor, individual copies of the "notes" can also be obtained from the DDC. The relevant addresses are:

- 1) Defense Documentation Center
Cameron Station
Alexandria, VA 22314
- 2) Dr. Carl E. Baum, Editor
Air Force Weapons Laboratory/ELT
Kirtland Air Force Base
New Mexico 87117

-
- [S.1] C.E. Baum, "Notes Concerning Electromagnetic Design and Performance of ATLAS I and II," ATLAS Memo 17, 2 September 1976.
 - [2.1] C.E. Baum, "Pulse Power Problems with Respect to EMP Simulators," Pulse Power Memo 1, 5 June 1977.
 - [2.2] A.S. Denholm, G. Simcox and H. Milde, "Electromagnetic Pulse System, Vol. I, Van de Graaff Generator Design," AFWL-TR-69-15, Vol. I, August 1969.
 - [2.3] McDonnell-Douglas Corporation, "TRESTLE Program: Pulse Power Subsystem Design Analysis Report, CDRL-A015, Vol. II - Appendix A, TRESTLE Pulser Module Technical Memorandum (TRETm)," MDCG 5797, 16 June 1975.
 - [2.4] G. Simcox, "Pulser for Vertically Polarized Dipole Facility (VPD-II)," Final Report for AFWL Contract F29601-76-C-0048, October 1978.
 - [3.1] N. Marcuvitz, Editor; Waveguide Handbook, Section 2.8b, pp. 98-100, Dover Publications, New York, 1965.

- [3.2] F.C. Yang and K.S.H. Lee, "Impedance of a Two-Conical-Plate Transmission Line," Sensor and Simulation Note 221, November 1976.
- [3.3] F.C. Yang and L. Marin, "Field Distributions on a Two-Conical-Plate and a Curved Cylindrical-Plate Transmission Line," Sensor and Simulation Note 229, September 1977.
- [3.4] C.E. Baum, "Early Time Performance at Large Distances of Periodic Planar Arrays of Planar Bicones with Sources Triggered in a Plane-Wave Sequence," Sensor and Simulation Note 184, August 1973.
- [3.5] W.R. Smythe, Static and Dynamic Electricity, 2nd ed., Section 6.20, McGraw-Hill Book Company, 1950.
- [4.1] N. Marcuvitz, Editor; Waveguide Handbook, Section 2.2, pp. 62-66, Dover Publications, New York, 1965.
- [4.2] C.E. Baum, "Impedance and Field Distributions for Parallel-Plate Transmission Line Simulators," Sensor and Simulation Note 21, 6 June 1966.
- [4.3] T.L. Brown and K.D. Granzow, "A Parameter Study of Two Parallel Plate Transmission Line Simulators of EMP Sensor and Simulation Note 21," Sensor and Simulation Note 52, 19 April 1968.
- [4.4] C.E. Baum, D.V. Giri and R.D. González, "Electromagnetic Field Distribution of the TEM Mode in a Symmetrical Two-Parallel-Plate Transmission Line," Sensor and Simulation Note 219, 1 April 1976.
- [4.5] L. Marin, "Modes on a Finite-Width, Parallel Plate Simulator, I. Narrow Plates," Sensor and Simulation Note 201, September 1974.
- [4.6] T. Itoh and R. Mittra, "Analysis of Modes in a Finite-Width Parallel Plate Waveguide," Sensor and Simulation Note 208, January 1975.
- [4.7] L. Marin, "Modes on a Finite-Width, Parallel-Plate Simulator, II. Wide Plates," Sensor and Simulation Note 223, March 1977.

- [4.8] R. Mittra and S.W. Lee, "Excitation of Modal Fields in Parallel Plate Transmission Lines," Final Report for AFOSR 76-3066, 30 June 1976 to 31 December 1978, February 1979.
- [4.9] J.C. Giles, M.K. Bumgardner, G. Seely and J. Furaus, "Evaluation and Improvement of the CW Performance of the ALECS Facility," AFWL-TR-75-93, Volumes I and II, September 1975.
- [4.10] T.T. Wu, R.W.P. King, D.J. Blejer and S.-K. Wan, "Laboratory Model Parallel-Plate Transmission Line Type of EMP Simulator (Description of the Setup and and Sample Measurements)," Miscellaneous Simulator Memo 16, 31 July 1977.
- [4.11] M. Krook, R.W.P. King, D.J. Blejer, T.K. Sarkar and S.-K. Wan, "The Electric Field in a Model Parallel Plate EMP Simulator of a High CW Frequency," Miscellaneous Simulator Memo 17, 31 July 1978.
- [4.12] D.L. Endsley and D.B. Westenhauer, "Special Report on Field Measurements," ALECS Memo 4, 28 December 1977.
- [5.1] C.E. Baum, "Admittance Sheets for Terminating High-Frequency Transmission Lines," Sensor and Simulation Note 53, April 1968.
- [5.2] R.W. Latham and K.S.H. Lee, "Termination of Two Parallel Semi-infinite Plates by a Matched Admittance Sheet," Sensor and Simulation Note 68, January 1969.
- [5.3] C.E. Baum, "A Sloped Admittance Sheet Plus Coplanar Conducting Flanges as a Matched Termination of a Two-Dimensional Parallel-Plate Transmission Line," Sensor and Simulation Note 95, December 1969.
- [5.4] A.D. Varvatsis and M.I. Sancer, "Performance of an Admittance Sheet Plus Coplanar Flanges as a Matched Termination of a Two-Dimensional Parallel-Plate Transmission Line, I. Perpendicular Case," Sensor and Simulation Note 163, January 1973.
- [5.5] A.D. Varvatsis and M.I. Sancer, "Performance of an Admittance Sheet Plus Coplanar Flanges as a Matched Termination of a Two-Dimensional Parallel-Plate Transmission Line, II. Sloped Admittance Sheet," Sensor and Simulation Note 200, June 1974.

- [5.6] D.V. Giri, C.E. Baum, C.M. Wiggins, W.D. Collier and R.L. Hutchins, "An Experimental Evaluation and Improvement of the ALECS Terminator," ALECS Memo 8, May 1977.
- [5.7] C.E. Baum, D.V. Giri and R.D. González, "Electromagnetic Field Distribution of the TEM Mode in a Symmetrical Two-Parallel-Plate Transmission Line," Sensor and Simulation Note 219, April 1976.
- [5.8] D. Higgins, "Consideration of Properly Terminating the Simulator Transmission Line," ATLAS Memo 7, February 1972.
- [6.1] K.M. SooHoo, "Numerical Analysis of a Transmission-Line EMP Simulator," Sensor and Simulation Note 209, 18 January 1974.
- [6.2] D.G. Dudley and J.P. Quintenz, "Multi-modal Transient Excitation Effects in an Infinite Parallel-Plate Waveguide," Canadian Journal of Physics, Vol. 50, pp. 2826-2835, 1972.
- [6.3] A.M. Rushdi, R.C. Mendez, R. Mittra and S.-W. Lee, "Leaky Modes in Parallel-Plate EMP Simulators," IEEE Trans. Electromagn. Compatib., Vol. EMC-20, pp. 443-453, 1978.
- [6.4] L. Marin, "Modes on a Finite-Width, Parallel-Plate Simulator, I. Narrow Plates," Sensor and Simulation Note 201, September 1974.
- [6.5] L. Marin, "Modes on a Finite-Width, Parallel-Plate Simulator, II. Wide Plates," Sensor and Simulation Note 223, Revised November 1977.
- [6.6] L. Marin and G.C. Lewis, Jr., "Modes on a Finite-Width, Parallel-Plate Simulator, III. Numerical Results for Modes on Wide Plates," Sensor and Simulation Note 227, September 1977.
- [6.7] N. Marcuvitz, Waveguide Handbook, p. 64, McGraw-Hill Book Company, New York, 1951.

- [6.8] T.T. Wu, R.W.P. King, D.J. Blejer and S.-K. Wan, "Laboratory Model Parallel-Plate Transmission Line Type of EMP Simulator (Description of the Setup and Sample Measurements)," Miscellaneous Simulator Memo 16, 31 July 1977.
- [6.9] M. Krook, R.W.P. King, D.J. Blejer, T.K. Sarkar and S.-K. Wan, "The Electric Field in a Model Parallel-Plate EMP Simulator at a High CW Frequency," Miscellaneous Simulator Memo 17, 31 July 1978.
- [6.10] R.W. Burton, R.W.P. King, D.J. Blejer, "Surface Currents and Charges on an Electrically Thick and Long Conducting Tube in E- and H- Polarized, Normally Incident, Plane-Wave Fields," Radio Science, Vol. 13, pp. 75-91, January-February 1978, and Section V of Interaction Note 336, October 1977.
- [7.1] R.W. Latham, "Interaction Between a Cylindrical Test Body and a Parallel Plate Simulator," Sensor and Simulation Note 55, May 1968.
- [7.2] C.D. Taylor, "On the Pulse Excitation of a Cylinder in a Parallel Plate Waveguide," Sensor and Simulation Note 99, March 1970.
- [7.3] R.W. Latham and K.S.H. Lee, "Electromagnetic Interaction Between a Cylindrical Post and a Two-Parallel-Plate Simulator, I," Sensor and Simulation Note 111, July 1970.
- [7.4] K.S.H. Lee, "Electromagnetic Interaction Between a Cylindrical Post and a Two-Parallel-Plate Simulator, II (A Circular Hole in the Top Plate)," Sensor and Simulation Note 121, November 1970.
- [7.5] F.M. Tesche, "On the Behavior of Thin-Wire Scatterers and Antennas Arbitrarily Located Within a Parallel Plate Region, I (The Formulation)," Sensor and Simulation Note 135, August 1971.
- [7.6] L. Marin, "A Cylindrical Post Above a Perfectly Conducting Plate, II (Dynamic Case)," Sensor and Simulation Note 136, August 1971.
- [7.7] K.S.H. Lee, "A Vertical Post Inside a Two-Parallel-Plate Simulator," Sensor and Simulation Note 139, October 1971.

- [7.8] A.D. Varvatsis and M.I. Sancer, "Electromagnetic Interaction Between a Perfectly Conducting Sphere and a Two-Parallel-Plate Simulator, I (Top Plate Removed)," Sensor and Simulation Note 140, October 1971.
- [7.9] F.M. Tesche, "Numerical Determination of the Step Wave Response of a Thin-Wire Scattering Element Arbitrarily Located Above a Perfectly Conducting Ground Plane," Sensor and Simulation Note 141, February 1972.
- [7.10] L. Marin, "Application of the Singularity Expansion Method to Scattering from Imperfectly Conducting Bodies Within a Parallel Plate Region," Interaction Note 116, June 1972.
- [7.11] J. Lam, "Interaction Between a Parallel-Plate EMP Simulator and a Cylindrical Test Object," Report by Dikewood Industries, October 1978.
- [7.12] K.R. Umashankar, T.H. Shumpert and D.R. Wilton, "Scattering by a Thin Wire Parallel to a Ground Plane Using the Singularity Expansion Method," IEEE Trans. on Antennas and Propagation, Vol. AP-23, No. 2, pp. 178-184, March 1975.
- [8.1] C.E. Baum, D.V. Giri and K.C. Chen, "An Overview of EM Considerations of ATLAS in the Context of Current and Future Efforts," ATLAS Memo 22, 5 January 1977.
- [8.2] C.E. Baum, "Electromagnetic Considerations for Pulser Design," ATLAS Memo 10, 6 April 1974.
- [8.3] C.E. Baum, "Pulse Power Problems with Respect to EMP Simulators," Pulse Power Memo 1, 5 June 1977.
- [8.4] C.E. Baum, "The Conical Transmission Line as a Wave Launcher and Terminator for a Cylindrical Transmission Line," Sensor and Simulation Note 31, January 1967.
- [8.5] T.K. Liu, "Impedances and Field Distributions of Curved Parallel-Plate Transmission-Line Simulators," Sensor and Simulation Note 170, February 1973.
- [8.6] R.W. Latham, "Reflection From an Array of Dielectric Posts," Sensor and Simulation Note 180, June 1973.

- [8.7] R. Blackburn and K.C. Chen, "Reflections from Singly and Doubly Periodic Array of Dielectric Posts," ATLAS Memo 12, May 1974.
- [8.8] W.D. Prather, J. Little, R. Blackburn and K.C. Chen, "The Reflection of Electromagnetic Waves from a Wooden Test Stand," ATLAS Memo 16, November 1974.
- [8.9] W.D. Prather, "The Reflection of Electromagnetic Waves from an Array of Electrically Small Metal Bolts and Rings," ATLAS Memo 15, September 1974.
- [8.10] K.C. Chen, B.K. Singaraju and C.E. Baum, "Preliminary Estimates for Distant Fields," ATLAS Memo 13, 13 September 1974.
- [8.11] C.E. Baum and D.V. Giri, "Low Frequency Distant Fields for ATLAS I and II and Comparison with ALECS and ARES," ATLAS Memo 19, 29 October 1974.

